Technische Universität München

The development of a sensor model for Large Ring Lasers and their application in seismic studies

Alexander Velikoseltsev

Vollständiger Abdruck der von der Fakultät für Bauingenieur– und Vermessungswesen der Technischen Universität München zur Erlangung des akademischen Grades eines
Doktor-Ingenieurs
genehmigten Dissertation.

Vorsitzender: Univ.-Prof. Dr.-Ing. habil. Th. Wunderlich
Prüfer der Dissertation:
1. apl. Prof. Dr.rer.nat., Dr.-Ing. habil. U. Schreiber
2. Univ.-Prof. Dr.-Ing. R. Rummel
3. Prof. D. Sc. Y. Filatov,
   Saint Petersburg State Electrotechnical
   University

Die Dissertation wurde am 6. April 2005 bei der Technischen Universität München eingereicht und durch Fakultät für Bauingenieur– und Vermessungswesen am 6. Juni 2005 angenommen.

Abstract

The general ring laser operation model is adopted for the large gyroscopes C-II and G. An extended set of auxiliary sensors information is used for the long time period data modeling and ring laser behavior analysis with respect to the ideal case. Both instrumental errors and orientational effects are estimated and compensated where possible. The instrumental stability improved approximately for one order of magnitude for timeseries with duration of up to 70 days. This makes small periodic signals of geophysical interest accessible in the presence of instrumental drift.

Basic considerations for the application of ring laser in seismology are presented. The design principles of the GEOsensor, a rotational measurement system for seismology, are demonstrated along with a comparison of rotational seismograms taken from different ring lasers as a proof of concept. The various Sagnac frequency extraction methods are analyzed and compared. As a result the key technology for obtaining rotational seismograms developed. The appropriate data acquisition approach has been chosen with respect to the requirements in seismology and is described.

The procedures of the GEOsensor ring laser component installation, beam path alignment and experimental setup are described. The comparison of the GEOsensor data with rotational signal from G and linear signal from standard seismometer are provided. The value of the GEOsensor as a complex stand-alone seismological station is discussed.

Zusammenfassung

Für die Korrektur der Rohmessungen der großen Ringlaser C-II und G wird das allgemeine Ringlasermodell verwendet. Über die Messung zusätzlicher Systemparameter konnten verschiedene Freiheitsgrade des Ringlasermodells weiter eingegrenzt werden. Damit ist in der Modellausgleichung eine Verringerung der Sensordrift von ca. 1 Größenordnung für Zeitreihen von bis zu 70 Tagen Länge erzielt worden. Somit werden auch noch kleine Signale von geophysikalischem Interesse in Anwesenheit von instrumenteller Drift zugänglich. Grundlegende Betrachtungen für die Anwendung von Ringlasern in der Seismologie werden dargestellt. Daraus leitet sich ein Sensorkonzept für einen Rotationssensor in der Seismologie ab, welches hier beschrieben wird.

Acknowledgements

I would like to thank my supervisor Prof. Dr. Ulrich Schreiber for his guidance and tremendous support throughout my time in Wettzell. I would also like to thank Geoff Stedman, Robert Hurst, Thomas Klügel, Y.V. Filatov, D.P. Loukianov, M.N. Burnashev, H. Igel, A. Cochard and A. Flaws for their support, participation in my work and useful discussions.

I'm very grateful to all the members of Fundamental station Wettzell staff for providing excellent working environment and good talks. In particular I would like to thank station manager Dr. Wolfgang Schlüter and workshop chief Josef Müller. My gratitudes also go to Prof. Dr. Markus Rothacher and Christiane Horz from Forschungseinrichtung Satellitengeodäsie TUM for their great help and patience.

On a personal note I would like to thank Marianne and Johan Fischer for their incredible hospitality and friendliness during my long stay in Fischerhof.

Finally I would like to acknowledge the support of Technische Universität München, Deutsche Forschungsgemeinschaft and Bundesministerium für Bildung und Forschung.

Contents

List of Figures

List of Tables

1. Introduction

1.1 The large ring lasers

Ring lasers detect rotation and since early 60's they gained one of the leading positions in the area of inertial navigation and motion control due to their large dynamic range, high precision, small size and the fact that they do not require any moving mechanical parts [3]. The principle of ring laser gyro (RLG) operation is based on the Sagnac effect when two oppositely propagating beams in the rotating cyclic cavity oscillate on slightly different optical frequencies where the frequency difference is proportional to the velocity of rotation. This beat frequency is proportional to the product of the geometric area (A) enclosed by the laser beams and the rotation rate (Ω) imposed on the cavity and inversely proportional to the wavelength (λ) of the laser and the perimeter (L) [4].

$$\Delta f = \frac{4A}{\lambda L} \vec{n} \cdot \vec{\Omega} \tag{1}$$

However the resolution and stability of conventional sensors are not good enough for the accurate measurement of fluctuations of Earth rotation for applications in geodesy and geophysics. Large ring lasers have the potential to be used for that purpose. The extension of the perimeter along with a highly symmetrical design of the cavity, a high mechanical stability and a high Q-factor provide the required sensitivity [33]. At the same time "lock-in" as the major error source is considerably reduced. The number of successfully built large gyroscopes demonstrates how the gradual increase of perimeter and design requirements approached the desired range of precision. The first HeNe ring laser device dubbed C-I was constructed in Christchurch (New Zealand). It enclosed an area of 0.755 m^2 and was one of the first ring lasers that unlocked at the earth rate. The next generation ring laser C-II followed the same principle but was far superior in the mechanical construction and mirror design. C-II showed that by using an optimised design a high resolution as well as high stability of less than 1 part in 10^7 can be achieved over a time span of weeks and months. It was a reasonable expectation for the next development step of an even further upscaled ring laser G (Grossring) with an area of 16 m^2 that much higher degree of stability can be obtained by the corresponding reduction in backscatter [24]. The G ring was commissioned in 2001 and up to now it is the most stable and sensitive instrument within the ring laser project.

1.2 The RLG precision limit and resolution

In absence of any external rotation fluctuations and nonreciprocal effects the accuracy of a ring laser is limited by quantum noise. The analysis of phase fluctuations in counter-rotating beams defines the random walk coefficient ($\delta\Omega$), which describes the minimally achievable fluctuations of the phase difference of the two beams. This is the fundamental limit of the sensitivity to rotation [39].

$$\delta\Omega = \frac{C}{2\pi K L} \sqrt{\frac{\hbar \omega \mu T}{2P_0}} \frac{1}{\sqrt{t}} \tag{2}$$

P_0 is the beam output power observed at the mirror with known transmission T; μ is the total cavity loss; C the velocity of light; K the ring laser scaling factor, t the observation time and ω the optical laser frequency. Table 1 presents the corresponding random walk coefficients for all our currently operating rings.

Table 1: Characterization of the currently existing large ring lasers

Device	Perimeter, m	Area, m^2	τ, s	P_0, W	Q	μ, ppm	Random walk, $rad/s/\sqrt{t}$
C-II	4	1	1.5×10^{-4}	20×10^{-9}	4.5×10^{11}	89	7.2×10^{-10}
G	16	16	1×10^{-3}	3×10^{-9}	3×10^{12}	53	9×10^{-11}
G0	14	12	3×10^{-4}	3×10^{-9}	9×10^{11}	155	2×10^{-10}
UG1	77	370	2×10^{-3}	5×10^{-9}	6×10^{12}	128	4.7×10^{-12}
Geosensor	6.4	2.56	1.2×10^{-3}	22×10^{-9}	3.5×10^{12}	17	4.5×10^{-11}

In this table τ is the measured ring-down time, or photons' lifetime in the resonator. The mirror transmission value measured by manufacturer is 1.87 ppm. However for the modeling the value of mirror transmission has been taken as 13 ppm for all rings (see subsection 2.2.3 for details). For example in the G ring the spontaneous emission causes a measurement error of 9×10^{-11} radians per second, while the rotation rate of the earth contributes as much as 7.3×10^{-5} radians per second. This example demonstrates the high potential for the application of ring lasers in the field of geodesy and geophysics.

1.3 Application of large ring lasers in geodesy

Very-Long-Baseline-Interferometry (VLBI) routinely establishes the determination of length of day (LOD) to better than one part in 10^9, which corresponds to an uncertainty of less than 0.1 ms per day. Measurements are made by a set of globally distributed radio telescopes and with respect to a reference frame of quasar positions. The result is an accurate estimation of the global earth rotation and earth orientation. Ring lasers measure the earth rotation locally and within much smaller time intervals. They measure rotation absolute with respect to the local Fermi system. Therefore also local contributions to earth rotation are contained in the measurements. The effects of earth tides, strain, crust deformation, seismic events, polar motion are contained in the ring laser measurements due to their contribution to earth rotation or due to variations in the orientation of the respective ring laser.

1.4 Ring laser data modeling

In order to understand the performance of ring lasers it is possible to divide the contribution to the Sagnac frequency into three categories, which have been investigated in independent projects [19,21]:

- sensor error model
- orientation model
- rotation model

Diagram 1 illustrates the respective contributions to the ring laser output. The **sensor error model**, which is the subject of this work, estimates and corrects the errors from non-reciprocities[1] inside the ring laser cavity. These instrumental errors can be represented by:

- scaling factor correction
- null-shift errors due to any cavity non-reciprocity
- back-scatter due to nonlinear coupling of the two laser beams

Using auxiliary sensor data and the mono-beam optical power measurements along with the Sagnac frequency as the primary output of the ring laser, the model determines and corrects the instrumental errors of a ring laser.

The **orientation model** analyses the variations of the beam path relative to the local g-vector as a function of time. Local, regional or global geodetic aberrations cause changes of the orientation angle of the ring laser relative to the rotational axis of the earth and modifies the value of the measured Earth rate via the inner product in the ring laser equation (1). The **rotation model** finally identifies variations of the earth rotation rate, polar motion and energy exchange between atmosphere, hydrosphere and lithosphere and is the prime quantity of interest for our ring laser project.

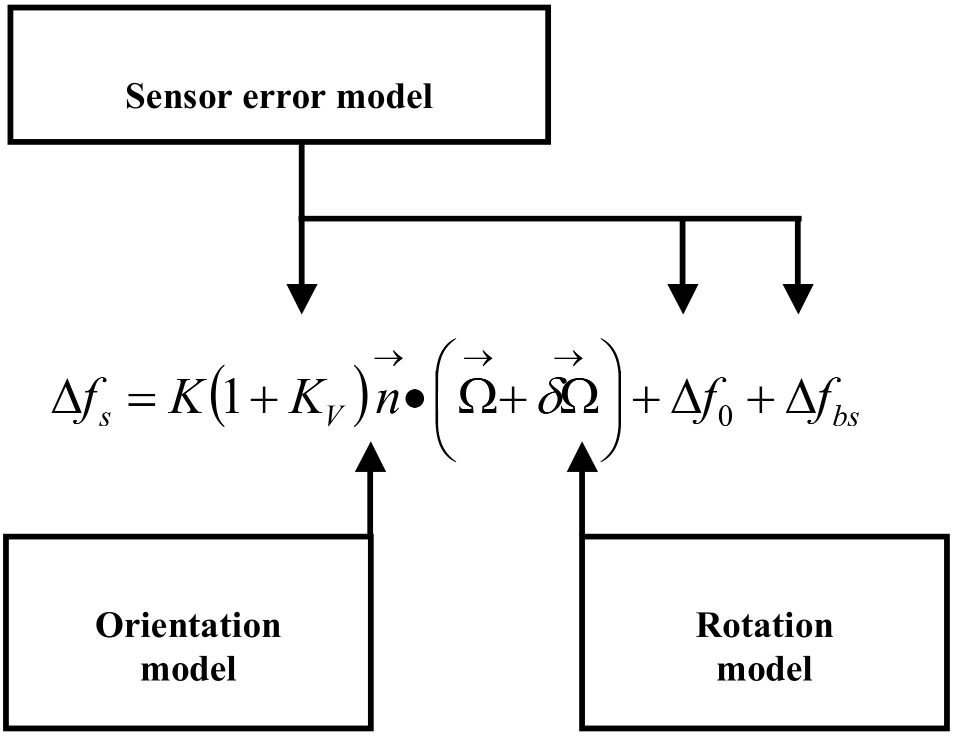

$$\Delta f_s = K\left(1+K_V\right)\vec{n}\bullet\left(\vec{\Omega}+\delta\vec{\Omega}\right)+\Delta f_0+\Delta f_{bs}$$

Diagram 1: The block diagram of the various contributions to the Sagnac frequency as measured by a large ring laser.

---

[1] Non-reciprocity here means inequality of the counter-rotating beam parameters caused by various reasons

2. Ring Laser Model

2.1 The RLG operation theory

The theoretical model of the RLG uses the semi-classical Lamb formalism that was developed for linear lasers and then adopted to ring lasers [4]. This approach results in a set of coupled differential equations, which describe the amplitudes and frequencies of the two counter-rotating beams.

$$\begin{aligned}(L/c)\dot{I}_1/I_1 &= \alpha_1 - \beta_1 I_1 - \theta_{12} I_2 - 2\rho_2 \cos(\psi + \varepsilon_2) \\ (L/c)\dot{I}_2/I_2 &= \alpha_2 - \beta_2 I_2 - \theta_{21} I_1 - 2\rho_1 \cos(\psi - \varepsilon_1) \\ \omega_1 + \dot{\varphi}_1 &= \Omega_1 + \sigma_1 + \tau_{12} I_2 - (c/L)\rho_2 \sin(\psi + \varepsilon_2) \\ \omega_2 + \dot{\varphi}_2 &= \Omega_2 + \sigma_2 + \tau_{21} I_1 - (c/L)\rho_1 \sin(\psi - \varepsilon_1)\end{aligned} \tag{3}$$

Ω_1 and Ω_2 are the resonator eigen-frequencies for the modes of the counter-propagating waves and ψ is the instantaneous phase difference between two beams. The dimensionless intensity of each beam is

$$I_i = \frac{|\mu_{ab}|^2}{2\eta^2 \gamma_a \gamma_b} E_i^2 \tag{4}$$

where μ_{ab} is the electric dipole matrix element between the laser states and γ_a and γ_b are the decay rates of the upper and lower laser energy levels. The coefficients α_i, β_i, θ_{ij} and τ_{ij} are the Lamb coefficients defined in terms of the plasma dispersion function. It is a complex function, which consists of a real part proportional to the dispersion of the active medium and an imaginary part proportional to the population inversion.

$$Z(\xi) = 2i\int_0^\infty \exp\left(-x^2 - 2\eta x - 2i\xi x\right)dx \tag{5}$$

$\xi = (\omega - \omega_0)/kU$ is a measure of the deviation of the laser oscillation frequency from the cavity center frequency and $\eta = \gamma_{ab}/kU$ is the relative value of the homogeneous broadening γ_{ab} (radiation decay rate plus collision induced rate) to the Doppler broadening kU. For the case of the Doppler limit ($\eta << 1$), which is typical for gas-lasers, the expressions for the real and imaginary parts of the dispersion function can be written as:

$$\begin{aligned} Z_I(\xi) &\approx \sqrt{\pi}\exp\left(-\xi^2\right) - 2\eta \\ Z_R(\xi) &\approx -2\xi \exp\left(-\xi^2\right)\end{aligned} \tag{6}$$

Thus the Lamb coefficients in amplitude equations are:

$$\alpha_i = G\frac{Z_I(\xi_i)}{Z_I(0)} - \mu_i \tag{7}$$

This term represents the threshold condition for each beam, where G is the gain in the line center and μ_i are losses for each beam.

$$\beta_i = G\frac{Z_I(\xi_i)}{Z_I(0)} \tag{8}$$

$$\theta_{ij} = G\frac{Z_I(\xi_j)}{Z_I(0)}L(\xi),\ L(\xi) = \left[1 + (\xi/\eta)^2\right]^{-1} \tag{9}$$

The terms β_i correspond to the gain saturation for each beam on itself due to hole burning and the θ_{ij} terms give the gain saturation for each beam due to the experienced hole burning by the other beam. In the frequency equations the terms σ_i represent the oscillation frequency pulling from the cavity eigen-frequency. The terms τ_{ij} are showing the mode pushing due to the hole burning in the dispersion curve.

$$\sigma_i = [c/2L]\cdot G\,\frac{Z_R(\xi_i)}{Z_I(0)} \tag{10}$$

$$\tau_{ij} = [c/2L]\cdot(\xi/\eta)G\,\frac{Z_I(\xi_i)}{Z_I(0)}L(\xi) \tag{11}$$

$$\rho_1 = r\sqrt{\frac{I_1}{I_2}},\ \rho_2 = r\sqrt{\frac{I_2}{I_1}},\ r = \frac{r_S\lambda}{4d} \tag{12}$$

The terms ρ_i are the respective backscatter amplitudes, where r is the fractional amplitude scattering coefficient (r_S is a mirror scattering and d is the beam diameter). Finally the beat frequency equation obtained from Eqs. 3 becomes

$$\begin{aligned}
\Delta f &= \frac{4A}{\lambda L}\vec{n}\cdot\vec{\Omega} && \text{- Sagnac frequency}\\
&+(\sigma_2-\sigma_1) && \text{- Scale factor}\\
&+\tau_{21}I_1-\tau_{12}I_2 && \ \text{corrections}\\
&+\frac{c}{2L}\left(\rho_2\sin(\psi+\varepsilon_2)+\rho_1\sin(\psi-\varepsilon_1)\right) && \text{- Backscatter}
\end{aligned} \tag{13}$$

Here the first term shows rotation induced frequency splitting, the second term is the differential frequency pulling which is responsible for a scale factor reduction. The terms in τ are the mode "pushing" correction to the optical frequency due to the hole burning. The last term is correcting for the experienced backscatter with backscattering phase angles ε_1 and ε_2 [3].

2.2 The RLG error model formulation

Taking the equation for the beat frequency it is customary to adopt the average frequency detuning $\xi = (\xi_1+\xi_2)/2$ and the difference $\xi_2-\xi_1 = K\Omega/kU \ll 1$ [38]. This allows the Taylor expansion of the Lamb coefficients about this parameter. For example:

$$\sigma_2 \cong \sigma + \frac{\partial\sigma}{\partial\xi}\frac{\Delta f}{2kU} \tag{14}$$

$$\sigma_1 \cong \sigma - \frac{\partial\sigma}{\partial\xi}\frac{\Delta f}{2kU} \tag{15}$$

Thus

$$\Delta\sigma = (\sigma_2-\sigma_1) = \frac{\partial\sigma}{\partial\xi}\frac{\Delta f}{kU} \tag{16}$$

The τ_{ij} are treated in a similar way and since the intensity values are close to each other they become

$$I_1 = I + \frac{\Delta I}{2},\ I_2 = I - \frac{\Delta I}{2} \tag{17}$$

Substituting all obtained parameters in the equation (13) we arrive at the following expression for the Sagnac frequency.

$$\Delta f = K\Omega + \Delta\sigma + \Delta\tau I + \tau\Delta I + \frac{c}{2L}\left(\rho_2\sin(\psi+\varepsilon_2)+\rho_1\sin(\psi-\varepsilon_1)\right) \tag{18}$$

where $K = 4A/\lambda L$ is the ring laser scale factor. The term $\Delta\sigma$ represents the difference in pulling and can be incorporated into the scale factor. It is responsible for a scale factor reduction from the empty cavity value. The mode pushing correction of the scale factor $\Delta\tau I$ is an order of magnitude smaller than the mode pulling correction and can be ignored for simplicity [4]. The generalized form of the RLG output signal therefore can be reduced to:

$$\Delta f = K(1+K_A)\Omega + \Delta f_0 + \Delta f_{bs} \tag{19}$$

These three major parts of the generalized RLG equation are now discussed in more detail.

2.2.1 Scale factor correction

In a first order approximation the expression for the Sagnac frequency is [4]:

$$\Delta f = K_R(1+K_A)\cdot\Omega = \frac{4A}{\lambda L}\left(1+\left(\frac{c}{2L}\right)\cdot\left(\frac{G}{kU}\right)\frac{Z'_r(\xi)}{Z_i(0)}\right)\cdot\Omega \tag{20}$$

K_R is a “resonator” part of scale factor and in a simplest case, when there are no non-reciprocal elements inside the cavity, it is a constant. Otherwise this coefficient must be calculated from:

$$K_R = \frac{4A}{\lambda}\left[L+\sum_i l_i(n_i-1)\right]^{-1} \tag{21}$$

where l_i is the length of the i-th part of the resonator which has refraction coefficient n_i. There are no dielectric elements in the constructed cavity but the stability of the A/L ratio is a very important part of the overall experimental stability. Instead of (21) the “resonator” part of scale factor can be simplified to:

$$K_R = \frac{4A}{\lambda L}\left[1+\delta\left(\frac{A}{L}\right)\right] \tag{22}$$

K_A characterizes the contribution of active medium to the scale factor because of fluctuations of gain, gas temperature, pressure, losses and frequency detuning.

$$K_A = \left(\frac{c}{2L}\right)\cdot\left(\frac{G}{kU}\right)\frac{Z'_r(\xi)}{Z_i(0)} \tag{23}$$

Typical scale factor corrections due to these contributions in the conventional gyros were found to be about $1\cdot 10^{-3}$ [4]. In practice most of the existing variations of the scale factor are the product of fluctuations of the active medium parameters. This is because of the higher stability of the parameters in K_R relative to those in K_A. Both the frequency detuning and the gain variations will contribute to the scale factor correction.

2.2.2 Null shift

The differential loss null shift represented by the term $\tau\Delta I$ in equation (18) is also important for the ring laser operation. This differential loss term appears due to unequal propagation conditions for the two counter-rotating beams. The major source of the amplitude non-reciprocity is an elliptical polarization of the counter-propagating beams, which in the presence of an external magnetic field creates a Faraday effect in the plasma [40]. Applied to our large rings we find no evidence of magnetooptical effects in the data. There is no strong magnetic field present in the laboratory and the deviation of the beam from S-polarization is very small if present at all. Another possible reason for non-reciprocity is coming from intra cavity gas flow (Langmuir effect). This effect is a prominent error source in DC excited lasers and is expected to be virtually non-existing in our lasers because of the applied RF-excitation scheme and the small size of the plasma. However, environmental factors like fluctuation of temperature, pressure and humidity in laboratory, as well as outgassing, reduce the Q-factor of a resonator, change its effective optical length and create different Q-factors for each counter-propagating beam. Therefore we are suffering from amplitude non-reciprocities. Since the measurements of beam power of each beam are available, the intensity difference can be taken directly from these data and the expression for the null shift error then is:

$$\Delta f_0 = [c/2L] \cdot \left(G \ \frac{\xi}{\eta} L(\xi) Z_i(\xi) \Big/ Z_i(0) \right) \cdot \Delta I \tag{24}$$

This null shift is an odd function of the frequency detuning and is zero at the maximum gain frequency. It is believed to be the major error in large perimeter RLG such as G. Consequently the stability of RF-excitation power becomes very important.

2.2.3 The backscatter

Lock-in phenomena in ring lasers have been thoroughly studied because of their critical importance for the optical gyro performance. The major problem for conventional gyros is the large lock-in threshold, which is a function of the net backscatter phase and so of the mirror separation [22]. The removal of this effect requires precautions like perimeter stabilization, dithering or the application of a rate bias. Taken from equation (18) the expression for scattering is:

$$\Delta f_{bs} = \frac{c}{2L} \left(\rho_2 \sin(\psi + \varepsilon_2) + \rho_1 \sin(\psi - \varepsilon_1) \right) \tag{25}$$

When assuming symmetry between the two directions with respect to the backscattering coefficients the expression (25) simplifies to ($\rho_1 = \rho_2 = \rho$, $\varepsilon_1 = \varepsilon_2 = \varepsilon$):

$$\Delta f_{bs} = \frac{c}{2L} \rho \cdot \sin(\psi) \cos(\varepsilon) \tag{26}$$

In a generalized way one can put the lock-in equation for the beat frequency into the form:

$$\Delta f = K\Omega - \Delta f_{bs} \tag{27}$$

where $K\Omega$ is the theoretical beat frequency. From equation (27) it can be seen that the beat frequency is always modulated at the lock-in rate in the presence of scattering. This appears as a weak modulation of the laser beam intensity at the frequency of the Sagnac rate. The amplitude of this “monobeam-modulation” is proportional to the amount of scattering. The phase difference between the two counter propagating modulated beams is measured continuously in C-II and its value corresponds to the sum of the respective net backscatter phases. Therefore it is possible to include this parameter into the model.

The lock-in threshold (27) is not the issue for the large rings because it is so much smaller than the signal of interest. A detailed investigation of the backscatter induced frequency pulling can be found [32]. However the importance of backscatter becomes progressively smaller for the very large ring lasers, because of the application of low-loss mirrors (scatter-loss approx. 2 ppm) and the very high mechanical stability of the instruments. While the backscatter definitely causes substantial contributions for C-II, where the modulation of the monobeam intensities with Sagnac frequency reaches value of more than 10%, there is very little evidence for backscatter in G. The following observations have been made. According to the recent measurements the ringdown time for C-II is 65 μs, which corresponds to a quality factor of

$$Q = 2\pi \cdot f_0 \cdot \tau = \frac{2\pi \cdot f_0 \cdot L}{\mu c} = 1.9 \cdot 10^{11} \tag{28}$$

and thus to a total cavity loss μ of 205 ppm. For a square ring laser cavity we have $\mu = \left(1 - R^4\right) \approx 4(1 - R) = 4(T + S)$, where T is the mirror transmission and S the mirror scattering. The same measurement for G gives a ringdown time of 1 ms. This corresponds to a total loss of 53 ppm. Since there is little evidences of monobeam modulation in G, we have to assume that most of the loss we observe is due to transmission rather than scatter. This results in a value of about 13 ppm transmission per mirror as an upper bound. Using this limit as a common figure for all the rings, we obtain an average scatter for 38 ppm per mirror for C-II. Therefore the backscatter correction is important in the model for C-II and may be negligible for G.

2.2.4 Polarization variations in ring lasers

The calculation presented above ignores the substantial discrepancy between the measured transmission (1.87 ppm) and the one obtained for the ring laser using ringdown time. The explanation is the following – the mirrors have polarization dependent transmission loss and since the measurement of the mirrors transmission has been done with S-polarized light, one can assume that the light inside the cavity is P- or elliptically polarized. Other sources of increased transmission loss are the mirror coating defects, through which the light escapes from the cavity. However this does not change the value of transmission accepted for the model since it's an actual value for G and for C-II the situation is similar.

During the GEOsensor test operation in Wettzell the measured ringdown time was about 1.2 ms. At the Pinion Flat observatory the same parameter is 100 μs. We assumed that one of the possible causes for increased cavity losses can be a ring nonplanarity, since the leveling exercise showed the deviation of one of the corner mirrors from the plane at the level of 6 mm. In a planar ring laser cavity the light is linearly polarized in the s direction. In case of a nonplanar resonator geometry the eigenmodes of the active cavity become circularly polarized, with the degree of nonplanarity defined by the fold angle β (Figure 1).

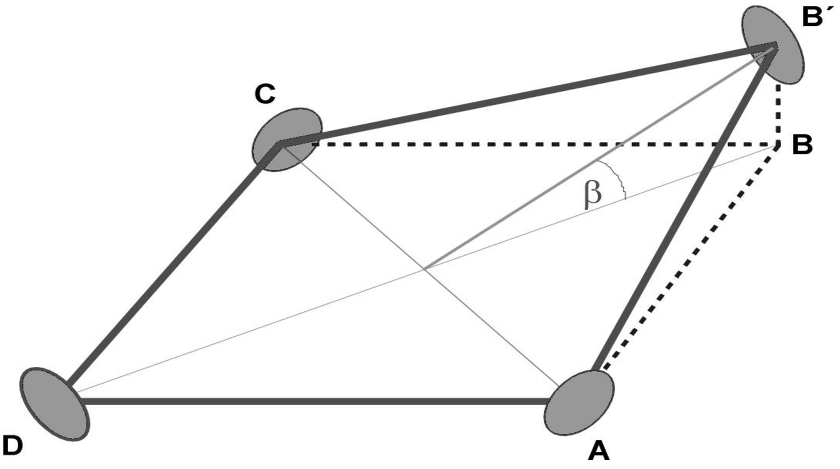

Figure 1: The geometrical path for a beam propagating in the near-planar ring laser cavity. The fold angle β depends on the mirror B elevation B-B´.

It has been shown [5] that the resonator eigenmode polarization is very sensitive to small deviations from planarity. Since all our ring lasers possess more or less nonplanar geometry, and this is especially probable in case of the GEOsensor ring laser due to its specific design, this effect can be responsible for the observed differences between the apparent transmission losses and the manufacturer specified values of those. The mirror imperfection is characterized by the anisotropy parameter for amplitude δ and birefringence χ. Following the formalism developed in [36] we can write the polarization component ratio as

$$\frac{E_p}{E_s} = \frac{\gamma \pm \sqrt{\gamma^2 - \beta^2}}{\beta} \tag{29}$$

where $\gamma = (\delta - i\chi)/\sqrt{2}$; $\delta = \sqrt{1-T_s} - \sqrt{1-T_p}$; T_p and T_s are the mirror transmission for p and s directions respectively. The ± sign in the equation 29 must be chosen with respect to the sign of the real part of $\sqrt{\gamma^2 - \beta^2}$ such that if this part is positive, the negative sign is selected. Using the obtained parameters for our present mirrors like T_s=0.2 ppm and T_p=58 ppm, we obtain the $\delta = 29 \cdot 10^{-6}$. The birefringence anisotropy value is chosen to be χ=$4 \cdot 10^{-3}$ rad, following the discussion of [5]. The fold angle β=$5{,}3 \cdot 10^{-3}$ rad calculated for 6 mm planarity deviation of one of GEOsensor mirrors. Therefore we have a situation where the birefringence dominates ($\chi >> \delta$) and the light inside the cavity becomes elliptically polarized with s and p as major axes.

We calculated the corresponding polarization component ratio for the ring lasers C-II, GEOsensor, G and UG-2 assuming identical mirror qualities and varying corner mirror planarity deviation from 0.1 mm up to 10 mm. The results are presented in Figure 2.

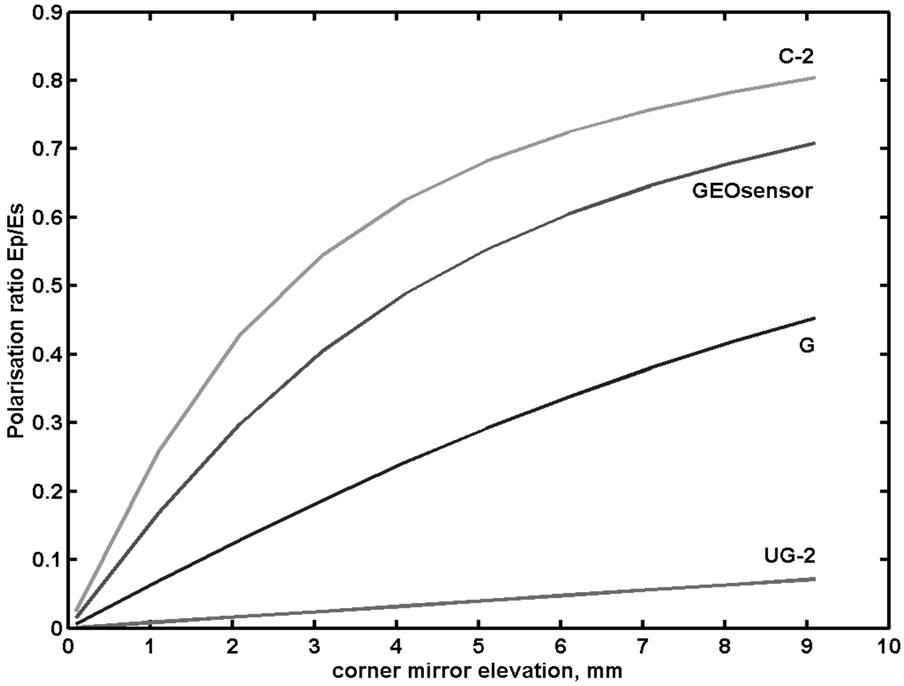

Figure 2: Polarization ratio dependency from the corner mirror elevation.

One can see that the size of the ring laser contour plays a major role in the nonplanarity induced polarization change: the bigger the ring the smaller becomes the fold angle for the same absolute inclination magnitude. The important conclusion is that the misalignment of the mirrors must be kept at the level less or equal to 1 mm for light being mostly linearly polarized. The polarization ellipticity produces a higher loss in the cavity, thus reducing the quality factor Q and therefore, the ultimate resolution of the ring laser. However for the current GEOsensor operation this is not very critical, since the expected signal magnitudes are still much higher than the reduced random walk parameter, caused by the reduction in the cavity Q. The value of the nonplanarity contribution to the cavity losses is still not fully confirmed experimentally since, for example in G ring, the observable amount of light coming out in p direction is barely observable (using a rather coarse direct observation method with low quality polarizer), while the measured loss per mirror is 13 ppm instead of expected 0.2 ppm. But still, even assuming presence of elliptical polarization in G cavity, one should expect a very small amount of p component (less than 5% of s component) because the designed mirror planarity deviation is better than 1 mm for this ring laser. At the moment the information whether the outcoming light in GEOsensor has the same profile as in G, or the p-plane light is clearly visible. Hence we can only guess that the nonplanarity induced polarization affects the ringdown time at Pinion Flat. Such discrepancy between the measured and design values of losses can be the result of the combination of the small nonplanarity, coating defects and scattering, but the polarization cannot yet be identified as a major source for increased losses.

2.3 Model modification

The model developed for this thesis is based on the formalism mentioned above and has been adapted to the special construction and operating features of our rings. This includes also the availability of auxiliary sensor information. The corresponding model is discussed below.

2.3.1 Homogeneous and inhomogeneous broadening

In general there are two types of line-broadening mechanisms, which are important in gas lasers [28]. The homogeneous broadening is represented by a Lorentzian function that describes the form of the spontaneous emission line. The expression for the homogeneous linewidth is

$$\gamma = \gamma_{ab} + (\partial\gamma_i / \partial P)P \qquad (30)$$

where $i = a,b$; γ_i is the radiative decay rate, P the gas pressure; $2\gamma_{ab} = \gamma_a + \gamma_b$ is the sum of the upper-state and the lower-state energy decay rates. For a ratio of Helium and Neon of 5:1 we have a homogeneous linewidth of $\gamma = [(8.5 \pm 2) + (59.5 \pm 2)P]MHz$ [2]. The second source provides the expression which contains the linewidth changes due to the variation of the partial pressures of both Helium and Neon ($\gamma = [(10 \pm 4) + (59 \pm 3)P_{He} + (29 \pm 6)P_{Ne}]MHz$) for a total gas pressure of 0.14-2.7 Torr and a Helium/Neon ratio of 0:1-49:1[41]. However the difference between these independently experimentally obtained approximations is not too large compared to our conditions and the first expression can be taken as a basic one. At the operational gas pressure of 7 mbar the value of homogeneous linewidth for our ring lasers is about 150 MHz. Note that the homogeneous broadening parameter γ is usually taken as FWHM of the full homogeneous linewidth.

The inhomogeneous broadening occurs when individual spectral packets are spread out about some central frequency. For a gas laser the typical cause for inhomogeneous broadening is the Doppler effect [13]. Milloni [17] provides the formula for the calculation of the Doppler width (FWHM)

$$\delta\nu_D = 2.15 \cdot 10^{12} \cdot \left(\frac{1}{\lambda} \cdot \sqrt{\frac{T}{M_x}}\right) \tag{31}$$

where the wavelength $\lambda = c/\nu$ is expressed in angstroms, the molecular weight of the absorbing species M_x in grams and the gas temperature T in Kelvin. A typical value for the Doppler width of the 633 nm line of Helium/Neon lasers is 1500 MHz. The second parameter, which is always included in the RLG equations, is the Doppler parameter kU, defined over the 1/e point of the curve.

$$kU = \frac{\delta\nu_D}{2\sqrt{\ln 2}} \tag{32}$$

Generally in the active medium of a gas laser both homogeneous and inhomogeneous broadening are present. The resulting line shape of the spectral line can be found by the convolution of the two contours [39], which are represented in Figure 3.

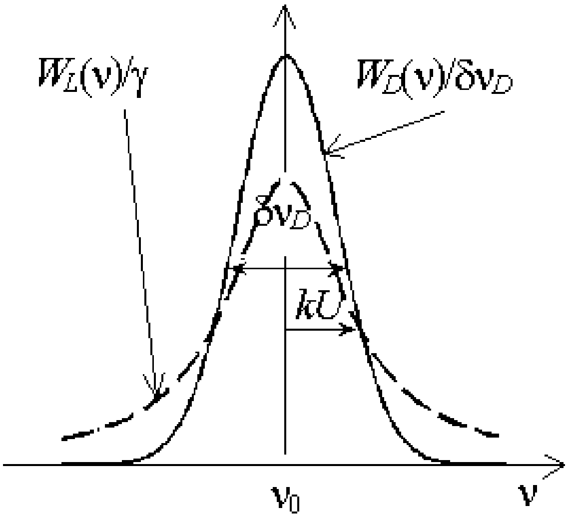

Figure 3: Doppler (Gaussian) contour WD and Lorentzian contour WL

The obtained curve is intermediate between a Lorentzian and a Gaussian and is known as the Voight profile. This Voight profile, or plasma dispersion function, depends on the ratio of the homogeneous and the inhomogeneous linewidths, which lies between 0.1 and 0.3 for our ring lasers. Since most of our ring lasers are operating on higher gas pressures (4-8 Torr), where both kinds of broadening are present, it is reasonable to adopt the Voight profile for our purpose.

2.3.2 Plasma dispersion function

The Voight profile or plasma dispersion function is a complex function, which consists of a real part proportional to the dispersion of the active medium and an imaginary part proportional to the population inversion.

$$Z(\zeta) = Z_r(\xi) + iZ_i(\xi) = 2i \int_{-\infty}^{i\zeta} \exp\left(-\left(x^2 + \zeta^2\right)\right) dx \tag{33}$$

where $\zeta = \xi + i\eta = (\omega - \omega_0)/kU + i\gamma/kU$; ξ is a measure of the deviation of the laser oscillation frequency from the center frequency and η is the relative value of the homogeneous broadening compared to the Doppler broadening. For the case of the Doppler limit ($\eta << 1$), which is typical for a gas-lasers and a frequency range of resonator detuning of $\xi < 1$ the expressions for the real and imaginary parts of the dispersion function can be written as:

$$\begin{gathered} Z_i(\xi) \approx \sqrt{\pi}\exp(-\xi^2) - 2\eta \\ Z_r(\xi) \approx -2\xi\exp(-\xi^2) \end{gathered} \tag{34}$$

These functions are shown in Figure 4 and represent the dependence of the gain ($Z_i(\xi)$) and active medium dispersion ($Z_r(\xi)$) from the resonator detuning ξ in the presence of both homogeneous and inhomogeneous broadening.

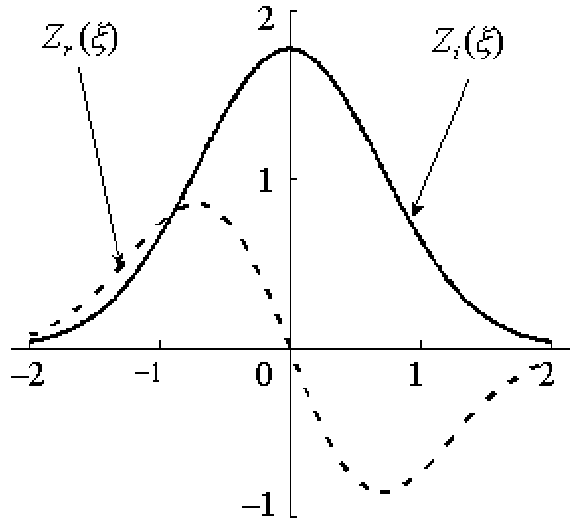

Figure 4: Real and imaginary parts of the Voight profile

Despite a slightly larger than normal relative broadening parameter $\eta = 0.15 - 0.3$ this expansion can still be applied to our ring lasers. Therefore all the Lamb coefficients can be written in terms of an oscillation frequency detuning. All our rings are filled with a 50:50 mixture of the isotopes Ne^{20} and Ne^{22} in order to avoid the mode competition problem. The isotope center transition separation is about 875 MHz. It provides a nearly symmetric (depends on isotopes ratio) gain curve with the maximum in the middle between the two transitions. For low gain operation and a high gas pressure, which are the typical working conditions for our rings, the Lamb dip usually is not observed [4]. The presence of the second Ne isotope changes all the Lamb coefficients and they become a function of the isotope ratio and must be modified as shown below:

$$\tau = [c/2L](G/Z_i(0))\left[\kappa_1 \frac{\xi_1}{\eta} L(\xi_1) Z_i(\xi_1) + \kappa_2 \frac{\xi_2}{\eta} L(\xi_2) Z_i(\xi_2)\right] \tag{35}$$

κ_1 and κ_2 are the partial amounts of each Neon isotope component; ξ_1 and ξ_2 are the frequency detuning measured with respect to the corresponding isotope center.

2.3.3 The optical frequency stability

The characteristics of the RLG output signal (scale factor correction, differential zero shift etc.) strongly depend on the active medium gain and dispersion. In turn these parameters are functions of the optical frequency detuning. Thus the stability of the optical frequency is the next important issue for the large ring laser operation. The fluctuations of the ambient temperature and the atmospheric pressure act on the cavity dimension, changing its effective optical length, which in turn affects the Q-factor of a resonator in the presence of backscatter and also creates a different Q-factor for the counter-propagating radiation. This is changing the tuning of the optical cavity. The main goal of all our instrumentation is to avoid any non-reciprocal elements inside the cavities in order to maintain a Q-factor as large and stable as possible. The absence of an active control system and passive stabilization of all the environmental parameters are done for the same purpose. Therefore there is no piezoelectric control of the ring laser perimeter included. In order to achieve a high mechanical stability for the perimeter, a monolithic block of Zerodur was used as the material for the ring body. According to the manufacturer (Schott Glaswerke) the linear thermal expansion coefficient of Zerodur is $\alpha=5\cdot10^{-9}$ K^{-1} and the elastic bulk modulus is $5.8\cdot10^{10}$ Pa. However even with stable Zerodur blocks the mirrors itself are suffering from membrane effect (induced by pressure variations) and bimetal-strip effect (temperature dependent). This effect may be larger than the thermal expansion or compression. The atmospheric pressure variations were found to be critical with respect to the stability of the C-II scale factor and backscatter induced frequency variations [24]. The integration of a pressure-stabilizing vessel (stability = ± 0.05 hPa) virtually eliminated any atmospheric pressure induced variations in perimeter and mirror separation. However small temperature variations were found to be the remaining major sources for perimeter fluctuations and the observed drift in the optical frequency. So the assumption has been made that the frequency pushing took a leading part in affecting the C-II performance [37]. Nevertheless this does not mean that the modeling of backscatter can be neglected from the C-II model. Both the differential null shift and backscatter phenomena are important in the description of our ring lasers. Any change of the cavity length results in a shift of the corresponding oscillation frequency, which is an integer multiple of the free spectral range.

$$\frac{\delta f_{FSR}}{f_{FSR}} = \frac{\delta L}{L} \tag{36}$$

The frequency detuning of a resonator relates to the perimeter fluctuations as

$$\xi(\nu) \approx \nu_0 \frac{\delta L}{L} \tag{37}$$

Perimeter variations strongly depend on the mechanical stability and the design features of the ring. In the model the optical frequency drift is described as in equation (38):

$$\nu = \Delta\nu + k\nu_T \cdot \delta T + k\nu_P \cdot \delta P \tag{38}$$

where $\Delta\nu$ is initial frequency offset from the center frequency, $k\nu_T$ the coefficient of the frequency dependence from temperature changes and $k\nu_P$ the coefficient of the frequency dependence from atmospheric pressure changes. δT and δP the respective temperature and pressure changes. This expression must be extended where additional sources of optical path length variations are identified. For C-II we have the temperature variations as the major contributor for perimeter changes, since the instrument is isolated with a pressure-stabilizing vessel and the level of residual pressure variations is too small. For G there is no clear evidence for a temperature or pressure fluctuation induced drift. Instead we observe some changes that correspond to a drift in the RF-power excitation system and are believed to influence the refractive index of the plasma and therefore cause a small change in the effective length of the cavity. However this effect is not yet unambiguously identified and therefore not yet added to equation (18).

2.3.4 Output power and gain

The single longitudinal mode operation regime, which is a prerequisite for a stable Sagnac-signal detection can be achieved by a reduction of the laser gain to near threshold operation. In theory this requirement is difficult to maintain with increasing size of the cavity, since the free spectral range (FSR) f=c/L is reduced at the same time. However by overpressuring the cavity, thus increasing homogeneous linewidth, one can achieve spontaneous single-frequency operation [30]. Recent investigations [7] demonstrated that stable monomode operation under condition of high gas pressure (6 – 8 mbar) can be established within very short time and adjacent cavity modes are suppressed within a frequency range of up to 200 MHz around center line. For example stable operation could be obtained for more than 2 weeks on a ring with a perimeter of about 77 m. The indication of the monomode regime is the absence of a beat note at the FSR frequency on the laser beam of one sense of rotation.

Under these conditions it becomes difficult to obtain the gain value for the modeling. However one can still implement the old approach to get an initial estimation, and then apply a scale factor to the gain variable. Below we will follow the old formalism for calculating the theoretical gain value by using threshold condition.

According to that criterion, the positive gain bandwidth, i.e. optical frequency range where the laser beam generation is possible, cannot exceed the range of twice the FSR. It means that under the assumption that the optical frequency is located right in the line center the laser threshold is not further away than one FSR in each direction. This threshold condition has been obtained from the first order perturbation theory [4] and can be written as:

$$\frac{G\left[\kappa_1 Z_i(\xi_1)+\kappa_2 Z_i(\xi_2)\right]}{Z_i(0)}=\mu \tag{39}$$

Assuming that the detuning is equal to one FSR and substituting the known value of cavity loss, we obtain the magnitude of the unsaturated gain. This method is not very precise, since the exact threshold frequency is unknown. On the other side the value is accurate enough to produce an upper bound for the gain. The indirect confirmation of this result can be taken from the expression for the output beam power

$$P_{out}=2I_s A_b T\left(\chi\frac{\left[\kappa_1 Z_i(\xi_1)+\kappa_2 Z_i(\xi_2)\right]}{Z_i(0)}-1\right) \tag{40}$$

where χ - gain/loss ratio; T - mirror transmission; A_b - beam area; κ_1 and κ_2 are the partial amounts of each Neon isotope component; ξ_1 and ξ_2 are the frequency detuning measured with respect to the corresponding isotope center; I_s - saturation intensity. The latter is a function of the total gas pressure [29] and can be approximated by

$$I_s=\left(15325+49127\cdot P+9968\cdot P^2\right)\frac{W}{m^2}, \tag{41}$$

where P is the total gas pressure in Torr. The intensities used in the RLG equations are dimensionless. In order to obtain this, we have to scale the output beam power properly. The expression for the dimensionless intensity is

$$I_i=\frac{\left|\mu_{ab}\right|^2}{2\eta^2\gamma_a\gamma_b}E_i^2. \tag{42}$$

μ_{ab} is the electric dipole matrix element between the laser states and γ_a,γ_b are the decay rates of two states and η is the reduced Planck constant. The ratio between the intensity and the electric field inside the cavity has the form [17]

$$I = \frac{1}{2}\varepsilon_0 c E^2 . \tag{43}$$

The ratio between the intensity inside the cavity and the output power is

$$I = \frac{P_{out}}{T \cdot A_b} . \tag{44}$$

Thus the square of the electric field amplitude inside the cavity can be written as

$$E^2 = \frac{2}{\varepsilon_0 c T A_b} P_{out} . \tag{45}$$

The final expression for the dimensionless intensity then becomes:

$$I = \frac{|\mu_{ab}|^2}{\hbar^2 \gamma_a \gamma_b} \frac{1}{\varepsilon_0 c T A_b} P_{out} . \tag{46}$$

The electric dipole matrix element is:

$$\mu_{ab} = 0.95 \cdot e \cdot a_0 . \tag{47}$$

where $e = 1.6022 \cdot 10^{-19} C$ is the elementary charge and $a_0 = 0.053 nm$ the Bohr radius. The decay rates for the $3s$ and $2p$ states are $\gamma_{3s} = 8.35 \cdot 10^6 + 1.0 \cdot 10^6 \cdot P[Hz]$ and $\gamma_{2p} = 9.75 \cdot 10^6 + 40.0 \cdot 10^6 \cdot P[Hz]$ respectively [2], with P the total gas pressure in Torr. The mirror transmission was obtained as $T = 13 ppm$. The beam area was measured to be $A_B = 2 \cdot 10^{-6} m^2$, c is the speed of light ($c = 2.9979 \cdot 10^8 ms^{-1}$) and $\varepsilon_0 = 8.8544 \cdot 10^{-12} C^2 N^{-1} m^{-2}$ the dielectric number. The reduced Planck constant finally is $\hbar = 1.0545 \cdot 10^{-34} Js$. For the operational gas pressure of 7 mbar the value of scale coefficient for the beam power is then 2.8×10^7.

2.3.5 The use of the model

The model is developed with the purpose of describing the Sagnac frequency departure from theory, caused by various instrumental properties under particular conditions. In general the three major types of RLG errors were investigated. The ability of the model to produce appropriate estimates of error parameters and RLG output signal is discussed below.

The modeling approach is straightforward. The ring data and auxiliary environmental information is recorded simultaneously as a function of time. The measured parameters are:

- Epoch of the measurement
- Sagnac frequency
- Output power independently from both beams
- Phase difference of backscatter modulation between both beams
- Temperature of the ring laser body
- Ambient atmospheric pressure at the ring laser body
- North/South and East/West monument tilt

Other important quantities such as the total gas pressure, partial gas pressures, ringdown time are providing the basis for the pre-computation of constant parameters such as the unsaturated gain and the homogeneous and inhomogeneous broadening. The parameters for the broadening are expected to remain constant since the gas pressure does not change, despite of some observed outgassing, which affects the gain but does not affect the pressure numbers. The gain value may change but it can be monitored indirectly by measuring the driving power or by using the mean output power of the two beams. The quantities of interest are the scale factor correction, null shift and nonlinearities of the Sagnac frequency induced by fluctuations of optical frequency, gain variations, unequal beam losses and backscatter respectively. The model is adjusted to the measured Sagnac frequency by varying the model parameters along with the additional information from the auxiliary data, until a least squares minimum is obtained. The model however is not valid for any boundary situation such as the operation in the multimode regime or for frequency locking. It relies on steady-state operation. This is supposed to be the normal regime for ring laser applications. The advantage of this approach is that we can exclude the differential equations for the intensities from the analysis and use the directly measured output power instead. So the model is sensitive to externally induced perturbations. As expected, this method is extremely sensitive to the quality of the input data. The removal of any instrumental drift from the auxiliary sensors as well as an increased performance of the optical detectors are highly desirable and the limiting factors for our model. This is especially important when photomultiplier tubes are used. Despite their high sensitivity these sensors have many disadvantages like temperature sensitivity and variations in quantum efficiency. Photodiodes offer far better overall usage characteristics – good sensitivity, linearity, low noise level, good stability and ease of use. Looking at the range of light levels in our rings – from hundreds of picowatts up to tens of nanowatts – the photodiodes are the best choice.

Parameters inferred from the environmental data are the coefficients of the optical frequency drift. Since no path length control is provided in the rings the changes of ambient parameters directly act on the optical path and consequently the tuning of oscillation frequency. Also when backscatter is considered the fractional scatter amplitude and phase are important. For the drift of the optical frequency equation (38) is applied. Equation (19) is solved for the parameters $\Delta\nu, k\nu_T$ and $k\nu_P$. In addition the backscatter fractional amplitude r and phase ε are taken as free and the model solves for them.

$$\Delta f_{bs} = r\frac{c}{2L}\sqrt{\frac{I_2}{I_1}}\cdot\cos(\varepsilon) \tag{48}$$

where the initial value for fractional scattering amplitude is taken as

$$r = \frac{r_S\lambda}{4d} \tag{49}$$

The gain variations δG are represented through the scaling of the RF power level, which is represented by normalized beam power P_{RF} as

$$G(P_{RF}) = G\cdot\delta G\cdot P_{RF} \tag{50}$$

Hence in all the terms of the Sagnac equation, which include the gain, the static value G is substituted with one from expression (50).

The general model dataflow is illustrated by Diagram 2. Here Ω is the theoretical Earth rotation rate at the site of the ring laser location (New Zealand – C-II; Germany - G). LSR is the least square residual method used as a criterion for minimizing the difference between the real Sagnac frequency and the error model. The difference in the number of output parameters will be explained in the following chapters.

The model has been written in MATLAB® using the standard toolboxes. The fitting routine is based on the Nelder-Mead simplex search method. This is a direct search method that does not use numerical or analytic gradients. If `n` is the length of `x`, a simplex in `n`-dimensional space is characterized by the `n+1` distinct vectors that are its vertices. In the two dimensional space, a simplex is a triangle; in three-dimensional space it is a pyramid. At each step of the search, a new point in or near the current simplex is generated. The function value at the new point is compared with the function values at the vertices of the simplex and the worst one is rejected. This step is repeated until the diameter of the simplex is less than the specified tolerance [18]. The function implemented was the least square residual between the measured Sagnac values and model. In order to decrease the influence of the instrumental noise on the fitting all the data used in the model were filtered. This is particularly important for temperature data that must be smoothed and shifted in the time domain. It is a reasonable assumption that the ZERODUR ring body acts as a low-pass filter on the timescale of minutes.

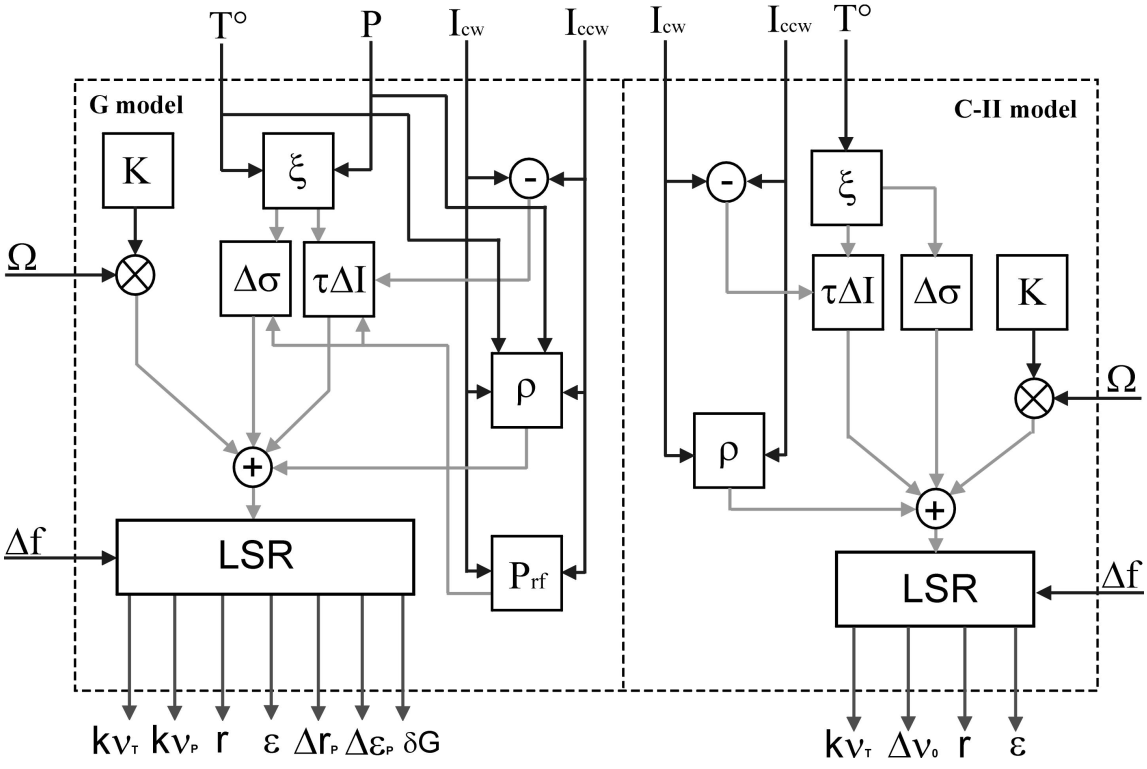

Diagram 2: The block diagram of the ring laser error model.

3. Applying the RLG error model to C-II and G

3.1 The results for C-II

The previously discussed ring laser model was applied to two long data sets obtained from C-II. The first sequence was recorded in March 2001. A plot of the Sagnac frequency versus time is shown in the Figure 5. The x-axis is scaled in days since the beginning of the measurement, while the y-axis shows the Sagnac frequency. The observed drift has contributions from both, null shift and backscatter induced frequency deviations. Scale factor variations are small as expected. Table 2 shows the obtained model parameters and the fitting error (according to the least squares criteria) for the whole data set.

Table 2: Null-shift and backscatter contributions for the C-II time-series started on March 13, 2001

$\Delta\nu_0$ [kHz]	$k\nu_T$ [kHz/K]	r	ε [rad]	Δlsr [Hz^2]
706	-877	$-4.26\cdot10^{-8}$	3.14	0.0075

A good agreement between the measurement and the model was obtained in general. However towards the end of the dataset one can see a progressively increasing deviation between measurements and model. This effect becomes even more apparent when one looks at the residuals between the measurements and the theoretical calculations (Figure 6).

Most of this drift is presumably caused by a temperature related drift in the quantum efficiency of the photomultiplier and degrades the reliability of the beam power measurements. As the result of this drift in the auxiliary instrumentation the obtained backscatter fractional amplitude is two orders of magnitude larger than the expected value of $r\approx9\cdot10^{-10}$ and of an unrealistic negative sign. To understand this result, one must look at the two basic elements of the model. Figure 7 shows the contribution of null-shift to the ring laser output, while Figure 8 displays the backscatter part. As one can see from Figure 8 the values of the backscatter corrections are constantly decreasing at a high rate. This is reflecting a detector drift rather than the true variation in the backscatter. A major difficulty for the fitting process is the fact that there is no direct measurement of the optical frequency in the resonator available.

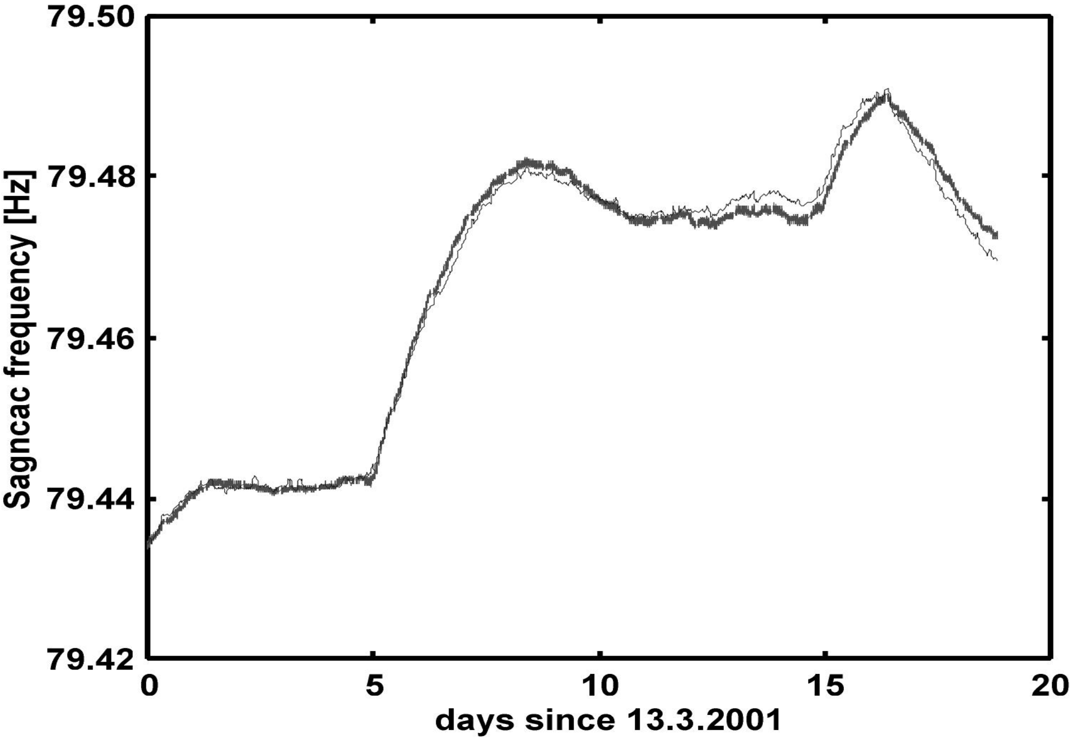

Figure 5: Raw dataset of C-II Sagnac frequency measurements obtained in March 2001 (black line) and the adjusted ring laser model (grey line)

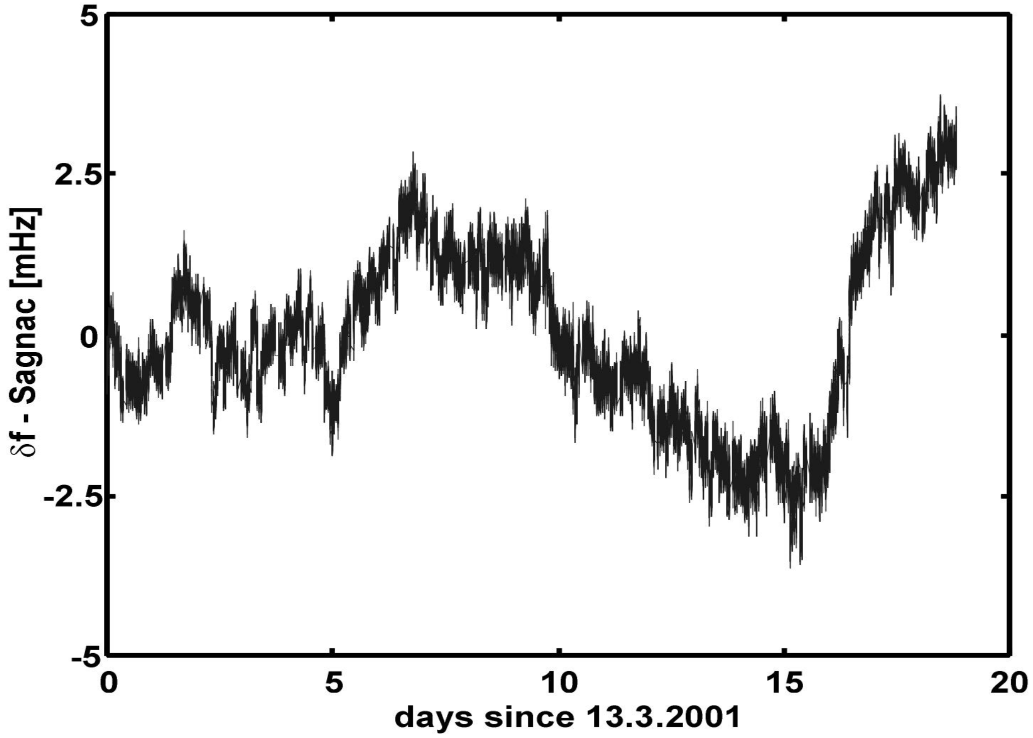

Figure 6: Residual plot of the measured Sagnac frequency and the model

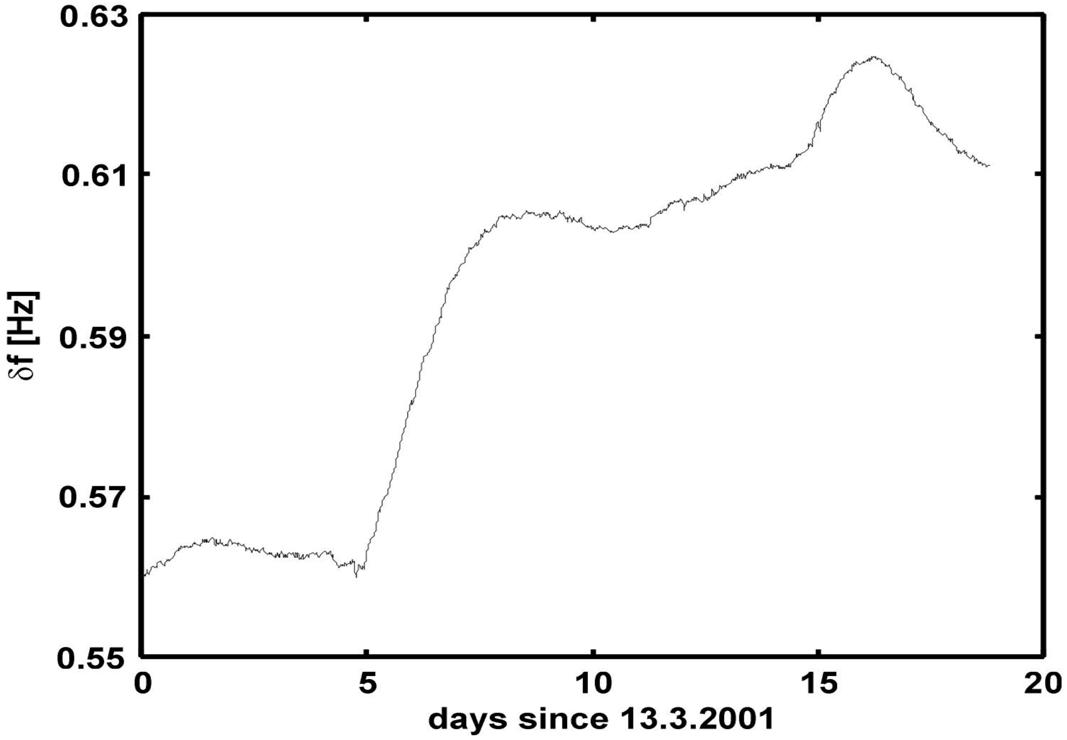

Figure 7: The null shift error contribution of the sensor model for the dataset started at 13.3.2001

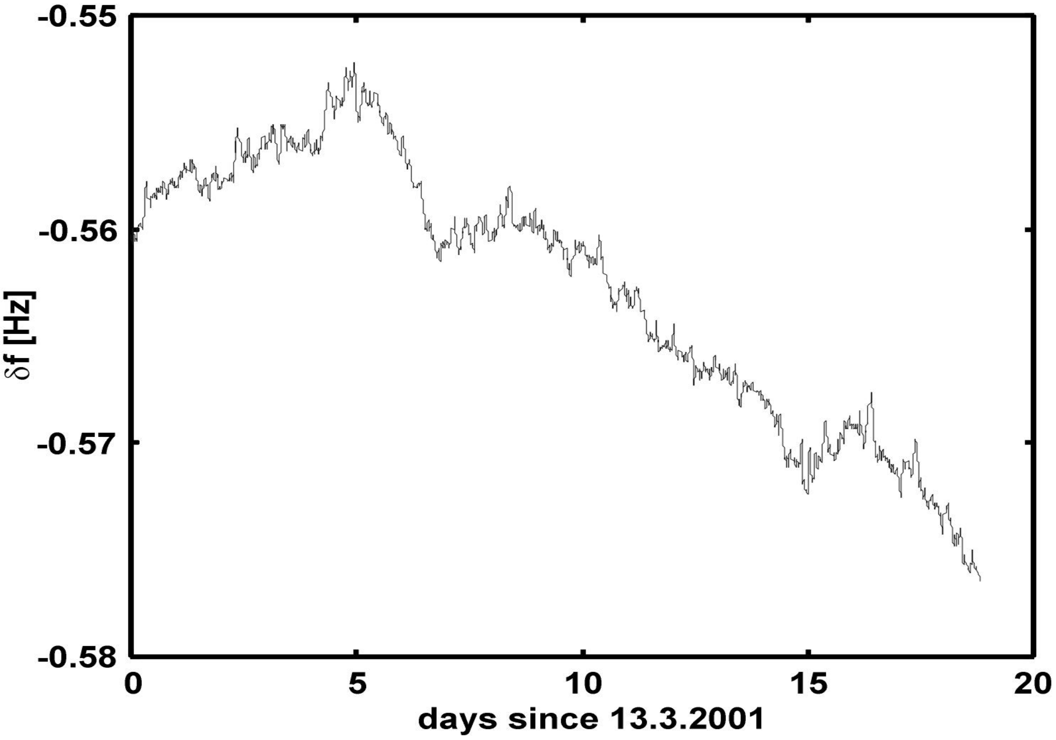

Figure 8: Backscatter induced offset of the sensor model for the dataset started at 13.3.2001

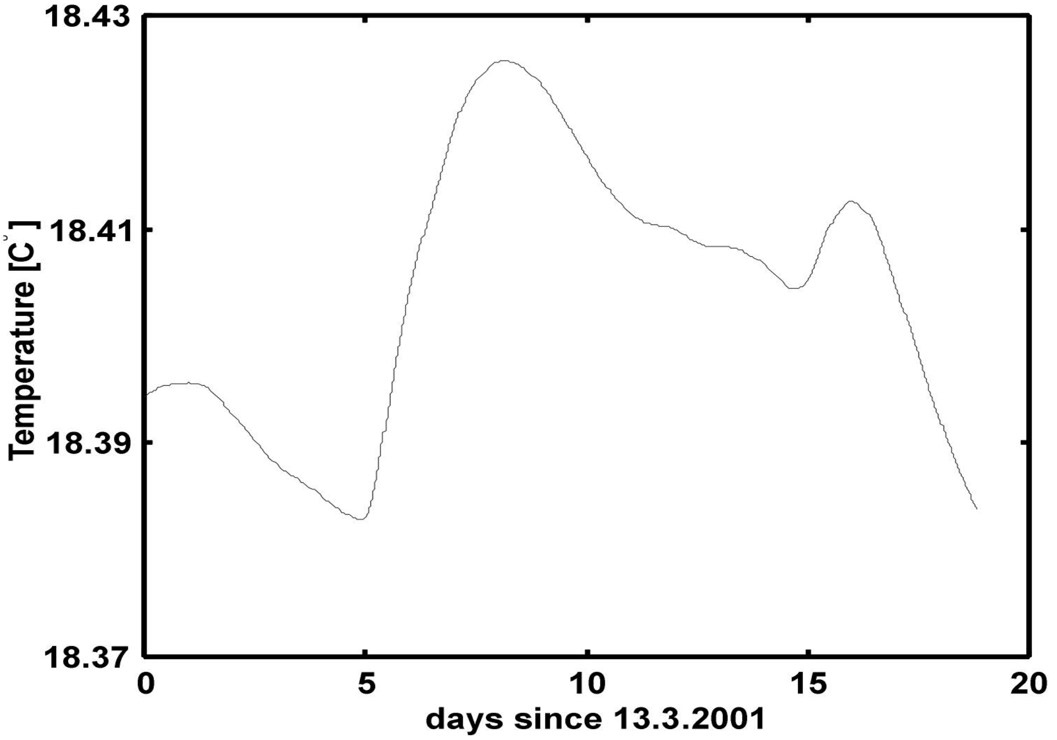

Figure 9: Temperature of the ring laser body over the measurement series started at 13.3.2001

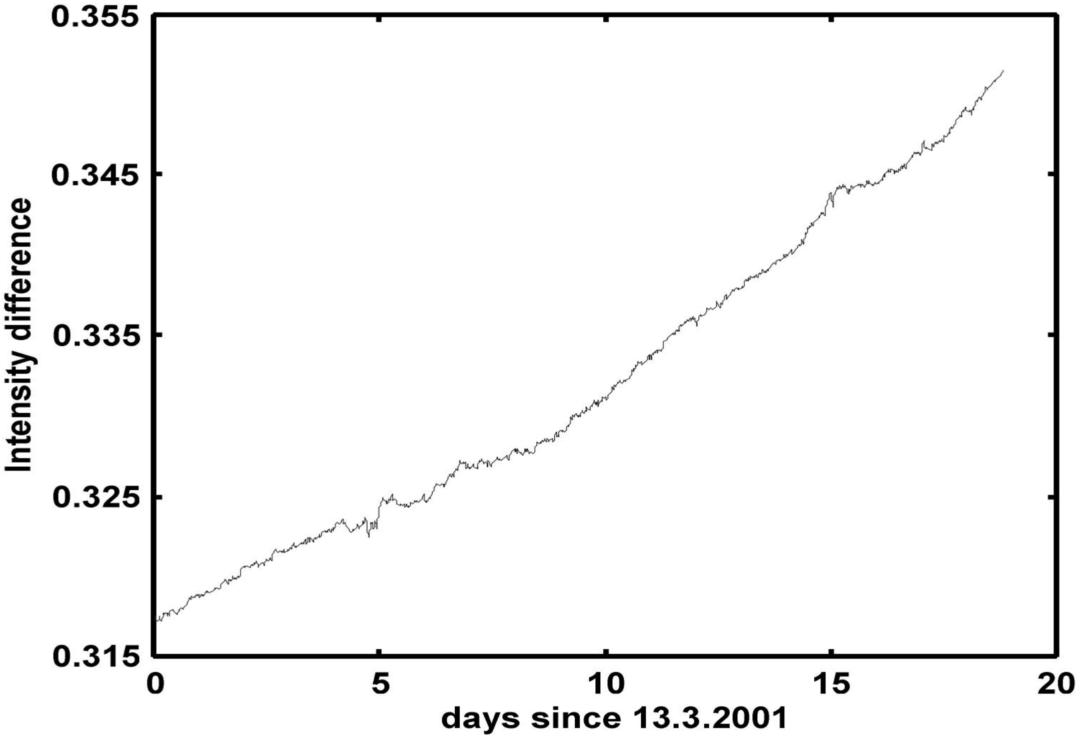

Figure 10: Intensity difference of the two counterrotating beams for the dataset started at 13.3.2001

Since this information is essential for the model to obtain the proper correction for the null-shift, the optical frequency as a function of time is inferred from time dependent temperature variations and an initial frequency estimate. The temperature measurements are made at one particular position on the monolithic ring laser body (Figure 9). Under conditions where there are only small temperature gradients one can assume a reasonable agreement. Another difficulty is coming from the drift of the optical power measurement as mentioned above. Figure 10 shows the time series of the intensity drift effects. One is believed to be coming from the drift in the optical frequency, while the other drift is caused by variations in quantum efficiency of the differences in the counterrotating beam powers. This even means that there are two applied photomultipliers. This latter effect is not extractable from the measurement quantity in Figure 10. The backscatter term however is not affected by these shortcomings. Therefore the fitting procedure has a tendency to adjust the scaling of the backscatter term in order to compensate for the shortcoming of the null-shift term for those measurement series, which are suffering from inadequate auxiliary sensor inputs.

Also the outgassing – the process of gas leakage into the cavity, which decreases the amount of active atoms on the higher energy levels, is responsible for the intensity drift. It creates the scale factor correction, which is smaller than null shift and backscattering contributions in C-II and the model is not able to estimate it adequately.

The absence of information about the changes in gain as well as the exact position of the optical frequency under the gain curve requires a few assumptions in order to obtain their real values. Assuming an isotropic thermal expansion of the Zerodur block, one can write for the optical frequency

$$\xi(\nu) \approx \nu_0 \frac{\delta L}{L} = \nu_0 \frac{4L(\alpha \cdot \delta T)/4}{L} = \nu_0 \cdot \alpha \cdot \delta T \tag{51}$$

According to the manufacturer the thermal expansion coefficient α for class 0 Zerodur is within the range of $1\text{–}20\times10^{-9}$/K. The largest temperature change in this dataset was -0.045 K, which corresponds to $\Delta\xi(\nu)_T$=21–426 KHz. This is a large range and the corresponding coefficient of the frequency dependence from temperature then becomes $k\nu_T$ = -(466KHz–9.4MHz)/K. From Zerodur samples of the tempered ring laser block the manufacturer Schott Glass works measured the expansion coefficient to be 5×10^{-9}/K, which corresponds to $k\nu_T = -2.37$MHz/K. The result of the numerical adjustment procedure is nearly three times less. There are a few possible causes for that, but the most likely one is that of formula (51). It does not necessarily describes the real perimeter variations, since the mirrors and mirror holders may have slightly different thermal characteristics. The so far largest contribution to these variations is the "membrane" effect, observed in both C-II and G ring lasers. It is a deformation of the mirror surface, i.e. a change in the beam position, due to the variations of external ambient pressure or temperature. Another difficulty is coming from the fact that we have only one value for the temperature of the ring laser body available, which is not necessarily representative for the entire block. One possible solution would be to obtain the optical path by constantly measuring the free spectral range [23]. Unfortunately this method is unavailable in a strict single mode operation. Therefore the best solution is the direct determination of the optical frequency [25]. In this model we only looked at a linear mechanism for optical frequency drifts. For a better understanding of this process a better experimental base is required and under preparation.

The second dataset with much longer duration was taken between September and November 2001. The resulting parameters after applying the fitting procedure are summarized in the table 3. Figure 11 shows the raw data along with the model, while the modeled residuals are displayed in Figure 12.

Table 3: The obtained fitting parameters for the measurement started in September 2001.

$\Delta\nu_0$ [kHz]	$k\nu_T$ [kHz/K]	r	ε [rad]	Δlsr [Hz^2]
19	-53	$9.64\cdot10^{-10}$	2.9	0.043

The same model as discussed for the previous case provides a good agreement with the shape of the observed data curve. The backscatter fractional amplitude is of the expected order of magnitude. The backscatter part mostly plays the role of an offset for the Sagnac frequency from the ideal magnitude, since the operational point is far away from the lock-in zone at a position where no strong non-linearity may be expected. As one can see a good agreement between the model and the observations can be obtained. However in comparison to the results of the previous dataset the coefficients for the offset value of the optical frequency and the temperature dependence of the cavity length are substantially different. This difference is the result of both hardware weakness (i.e. PMT drift) and model flexibility. There are too many degrees of freedom in the model, some of which are not determined very well. An example for this is the indirect determination of the optical frequency by using the temperature record in the dataset. Therefore it would be highly desirable for this particular model to obtain the optical frequency and the laser gain directly. This would immediately provide the proper scales and shape for the plasma dispersion function and so remove some uncertainties.

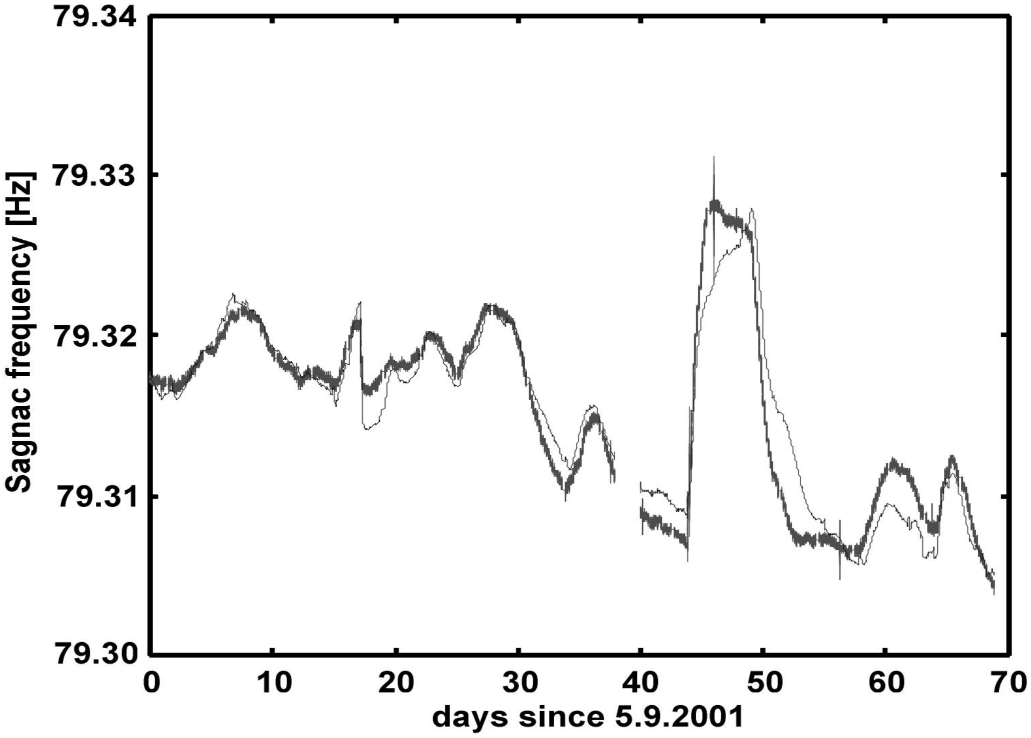

Figure 11: Dataset of Sagnac frequency measurements obtained in the period of September-November 2001 (black) and the fitted sensor model (grey)

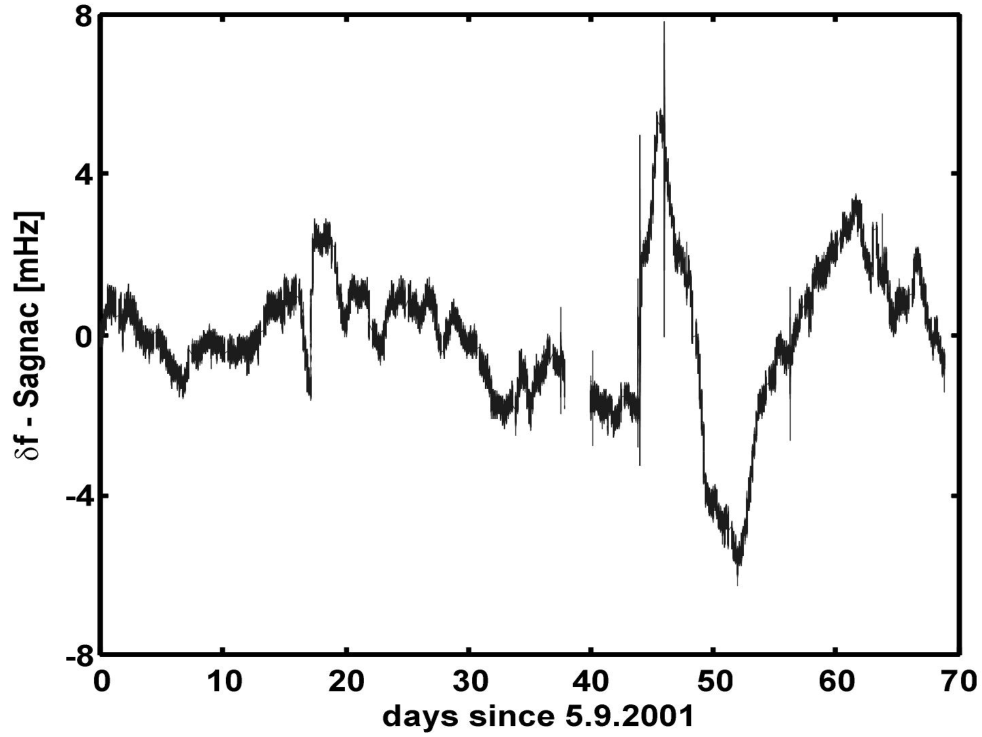

Figure 12: Residual plot of the measured Sagnac frequency and the model

In order to reduce the detector drift for the beam-power measurement the PMT was replaced by a photodiode with an integrated transimpedance amplifier. Figure 13 and table 4 are summarizing the result.

Table 4: The obtained fitting parameters for the measurement started in July 2002.

$\Delta\nu_0$ [kHz]	$k\nu_T$ [MHz/K]	r	ε [rad]	Δlsr [Hz^2]
840	-6.973	$4.16\cdot10^{-9}$	1.44	0.055

One can see that the effects of detector drift with time have been reduced, while the difficulties of computing the correct cavity frequencies from temperature changes still remain. In all cases the model, which is using the temperature measurements, is changing the calculated perturbed Sagnac frequency before the actually measured Sagnac frequency does so. The actually observed temperature lags behind the effective instrumental change.

Figure 14 shows the recent timeseries from C-II using a newly measured ringdown time of 65 μs. The fitting parameters are summarized in table 5. The backscattering contribution increased substantially and the overall fit quality is the worst ever. This indicates the enlarged scattering losses and degradation of the cavity quality factor, which is confirmed by the measurement of ringdown time.

Table 5: The obtained fitting parameters for the measurement started in Oktober 2003

$\Delta\nu_0$ [kHz]	$k\nu_T$ [MHz/K]	r	ε [rad]	Δlsr [Hz^2]
763	-1.432	$1.592\cdot10^{-7}$	3.14	0.55

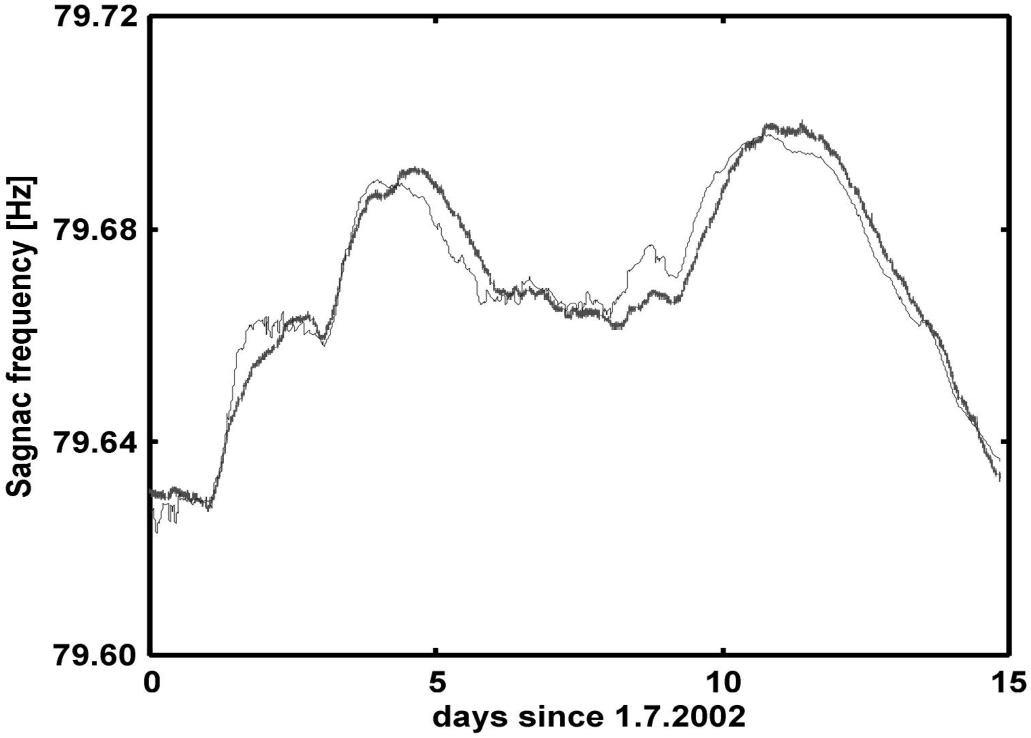

Figure 13: Dataset of Sagnac frequency measurements obtained in the July 2002 (black) and the fitted sensor model (grey)

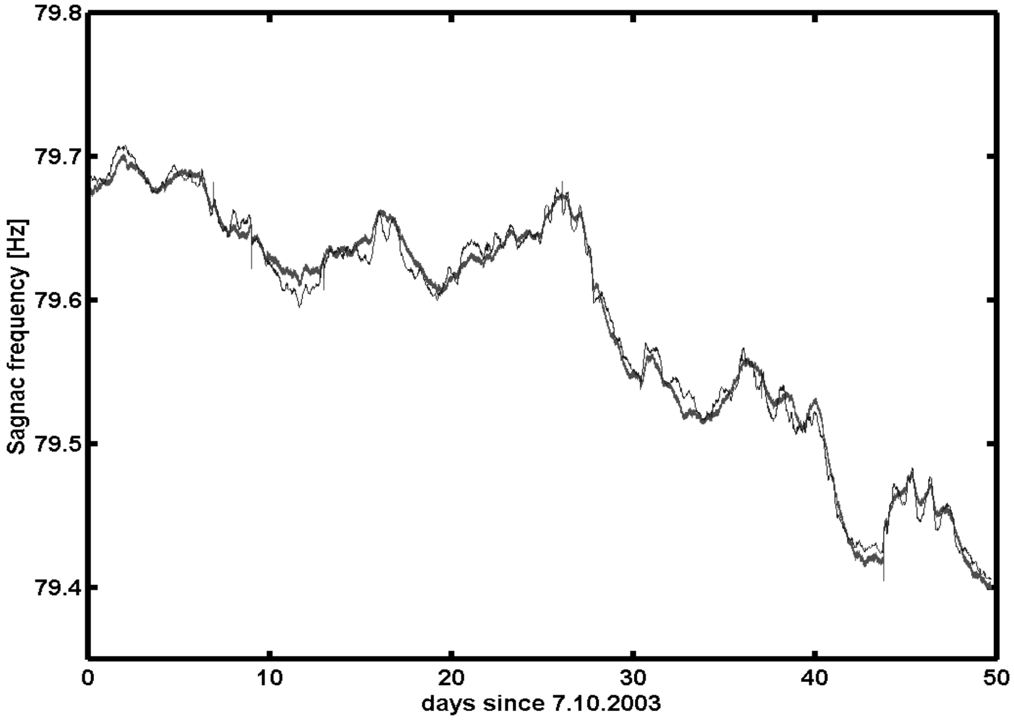

Figure 14: Dataset of Sagnac frequency measurements obtained in the Oktober-November 2003 (black) and the fitted sensor model (grey)

As one can see the distribution of the C-II model parameters is varying substantially from run to run. The initial offset frequency is not very important here since it is only symbolized from which side of the center line the optical frequency is located at the beginning of the run. The same holds for the backscatter phase, which is taken constant throughout the whole time series. As for the frequency temperature dependence and backscatter amplitude they are changing from 50KHz/K to 7MHz/K and from 10^{-9} to 10^{-7} respectively. Such large fluctuations may be caused by flexibility of the fitting procedure, which adjusts the model parameters to obtain the best fit. One needs a fixed reference parameter to provide the good fit and reliable magnitudes at the same time. Such a reference would be direct optical frequency measurement, which is a core parameter for most of the model parts.

3.2 The results for G

The ring laser G is 16 times larger in area than C-II and therefore much more sensitive to rotation. This larger scaling factor along with the horizontal orientation with respect to the local horizontal system results in a Sagnac frequency of 348.636 Hz at the Wettzell underground laboratory. For most of the time G does not show any severe dependence to variations in environmental parameters such as atmospheric pressure and the ring laser temperature. There is either no or very little amplitude modulation of the Sagnac frequency present on the lasing modes of the two counterpropagating beams. Since the mirrors nominally have the same specifications as those of our other rings, we believe that the upscaling of the rings provides an effective mechanism for the reduction of the backscatter contribution.

This avoids complications coming from the nonlinear character [39] of backscatter as an error source and leaves the scale factor correction and null shift as the remaining dominant error sources. The corresponding expression for the Sagnac frequency reduces to:

$$\Delta f = K(1 + K_A)\Omega + \Delta f_0 \tag{52}$$

where K_A characterizes the influence of the active medium on the scale factor correction and Δf_0 represents the null shift due to amplitude non-reciprocities in the resonator. The latter is the dominant error source in the G ring. We consider this as an outstanding success for the instrumental design. The source for this observed amplitude non-reciprocity is not yet well understood. One should note that the design of the G ring carefully avoids the presence of any asymmetry for the two counter-rotating beams and does not have any intra-cavity elements which would prefer one sense of rotation over the other. Since the beam intensities for both beams are recorded along with the Sagnac frequency itself, one can see that the ratio of the two intensities is changing with the RF-excitation power level. The trend of the variation of the beam intensity ratio is strongly correlated with the trend of the Sagnac frequency drift. This effect is demonstrated in Figure 15.

As one can see from the diagrams the Sagnac frequency is not only changed due to the gain adjustment (increase/decrease of the gain can be traced by observing the absolute value of the beam power) but in the presence of nonreciprocity also by magnification of null shift effect. The stable Sagnac frequency is observed when the power ratio is equal to 1 and the gain is constant. Therefore both the scale factor correction due to the active medium instability and the null shift due to the non-reciprocity are both important because of their dependence from the gain settings.

According to the model, the observed drift is not due to scale factor variations or changes in the orientation of the ring, because scale factor variations are only very small and the measured changes in orientation are far from reaching the required magnitude. Additionally, even in the presence of the area/perimeter variations the scale factor of the ring laser is independent of the wavelength and the ring laser dimensions as long as the same longitudinal index of the laser mode is maintained [27].

Table 6 summarizes the model results of the three available measurement sequences. Apart from the size the properties of the G ring in comparison to C-II are very similar. We have set the laser gas pressure in G (0.2 mB Ne; 5.8 mB He) on a lower level than C-II (0.2 mb Ne; 7 mB He) since it was found to be a good operation range in terms of stability of the monomode regime.

In general we observe a much higher consistency of the adjusted model parameters between independent measurement sequences in G than those obtained for C-II. The overall stability of G is much better than one would expect from the effect of the upscaling of the ring area only. The absence of atmospheric pressure influences for most of the time is important to note, while this in particular is the most critical error source in C-II. Furthermore it is currently difficult to identify any temperature influence on the Sagnac frequency unambiguously because of the nearly linear trend with time. On the other side we could see a very strong influence of the RF-excitation power on the effectively measured Sagnac frequency.

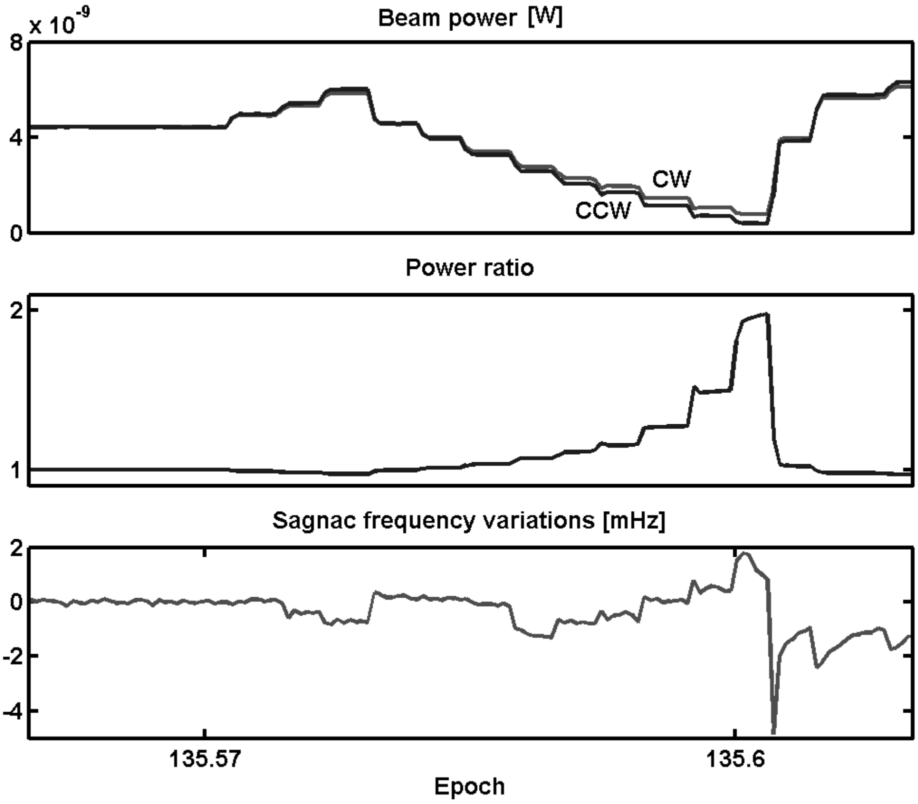

Figure 15: Variations of the counterrotating beam power ratio and, therefore, Sagnac frequency, by adjustment of the RF power level

Table 6: Summary of model parameters obtained from 3 different runs of G.

Run	$\Delta\nu_0$, MHz	$k\nu_T$, MHz/K	δG	Δf_0, mHz	Δlsr [Hz^2]
16.11.01 - 8.12.01	5.505	-1.332	-0.5	-0.017	1.3×10^{-5}
5.3.02 - 4.4.02	0.051	-0.150	10	-0.006	1.3×10^{-5}
18.4.02- 30.4.02	-0.016	0.161	22.6	-0.002	4.6×10^{-6}

The measured Sagnac frequencies of the three discussed measurement sequences are shown along with the respective model calculations as well as the corresponding residual plots in Figure 16 – 21.

The very prominent trend of the Sagnac frequency in Figure 16 corresponds to the drift in the power feedback loop circuit. The following upgrade of that control loop improved the stability of the Sagnac frequency substantially. The model is able to describe this frequency trend adequately though with some residual discrepancy. One can see that in the residual plot in Figure 17, there are some discrepancies especially in the first half of the graph. The possible cause for this may be the instrumental settling process that is usually observed right after the instrument started operating in the monomode regime. The small increase of the residuals between days 5 and 7 may correspond to detector shortcomings as well as to the real signal, such as external rotation. The same kind of discrepancy can be seen in Figure 19 but the strangest feature is coming from another effect. This effect is the change of the ring laser body orientation relative to the local vertical. The ring laser plane orientation change caused by a small monument movement leads to the reduction of the input rotational signal thus to a change in the resulting Sagnac frequency. For example, the change of the G-ring orientation by 1 μradian produces a Sagnac frequency change of about 300 μHz. We have a record of the tilt so this can clearly be quantified.

Figure 21 in particular demonstrates a good agreement between the real Sagnac frequency and the model. The frequency trend there is strongly correlated with the intensity difference variation, which contributed to the null shift.
The fact that the losses due to backscattering in the G ring are nearly negligible leads to the conclusion that the corresponding mirror losses mostly come from their transmission dependency (see section 2.2.4). The obtained value of 13 ppm per mirror being placed in (40) yields the correct order of magnitude. However since the overpressuring makes monomode operation possible even within 200 MHz bandwidth the threshold condition can only be applied as preliminary estimation while the real gain value can be different.

Most of the Sagnac frequency drift in the timeseries of Figure 16-21 is due to null shift, which depends on the intensity ratio and the variations of active medium parameters. The gradual improvement of the feedback loop design reduced the drift of the power for both beams but the accurate control system is still under construction. The offsets obtained by the model include the real misalignment of the beam path plane and frequency corrections that may appear because of incorrect scale or different initial conditions. That is why the additional measurements of the optical frequency or gain are so necessary, as well as a gain (i.e. RF power level) control.

In recent times an unusual susceptibility of the G ring to the pressure variations was observed. These variations were known as a critical factor for the C-II stability and the implication of the pressure-stabilizing tank has been the consequence of this sensitivity. So far no significant atmospheric pressure-correlated fluctuations were noticed and no backscatter phase measurements were available, therefore the pressure was excluded from the modeling. Nevertheless a recent timeseries from G demonstrates a strong correlation with the atmospheric pressure changes. In order to estimate the influence of those changes on the Sagnac frequency the model was extended with the backscatter correction. The difference between this model part for C-II and G is that in the case of C-II the fractional backscatter amplitude and phase are assumed to be constant while in the case of G, since there is no pressure stabilization used, we add the modulation of these parameters by the atmospheric pressure variations. The model results are summarized in the table 7.

Table 7: Summary of model parameters obtained from the recent run from G.

$\Delta\nu_0$ [kHz]	$k\nu_T$ [MHz/K]	r	ε [rad]	Δlsr [Hz^2]
-60	0.674	$5.13\cdot10^{-11}$	-0.0002	0.0000007
$k\nu_P$ [Hz/Pa]	Δf_0, mHz	Δr_P [1/Pa]	$\Delta\varepsilon_P$ [rad/Pa]	
40	-0.005	0.0018	-0.0002	

Here the $\Delta\nu_P$ is the optical frequency pressure dependence coefficient, Δr_P is the fractional scattering amplitude pressure dependence coefficient and $\Delta\varepsilon_P$ scatter phase pressure dependence coefficient respectively. The fractional backscatter amplitude is of the expected level of magnitude ($r \approx 3.9 \cdot 10^{-11}$). The good quality of the fit may also come from the short duration of the dataset. The Sagnac frequency along with the model and the residual frequency are shown in Figures 22 and 23. Most of the nonlinear drift of the Sagnac frequency strongly correlates with the ambient pressure. That is an illustration of the critical importance of controlling the backscatter for the stable operation of RLG. The backscatter amplitude and phase are strictly dependent on the mirror separation, which in turn is determined by the variations of the atmospheric pressure and ambient temperature due to compression or expansion of the ring laser cavity. The obtained value of the fractional backscatter amplitude corresponds to the fractional mirror scattering of about 0.3–0.6 ppm which is in agreement with the measured ringdown time and the estimated value of the mirror transmission. The cause of this sensitivity corresponds to the appearance of the second mode while the ring was running on a slightly higher than usual power level. The indication of the second longitudinal mode presence were the observable sidebands of about 0.3 Hz away from the main Sagnac line (amplitude modulation). The fluctuations of the Sagnac frequency produced by the change of the mode structure are much larger than the error sources discussed so far [39]. The resulting locked Sagnac frequency becomes dependent on the mode separation, which is a function of the optical path length. Thus the atmospheric pressure, which affects the cavity perimeter, became strongly correlated with the output signal. Currently the ring is operating in pure monomode regime and no evidence of the pressure influence on the Sagnac frequency is therefore observed.

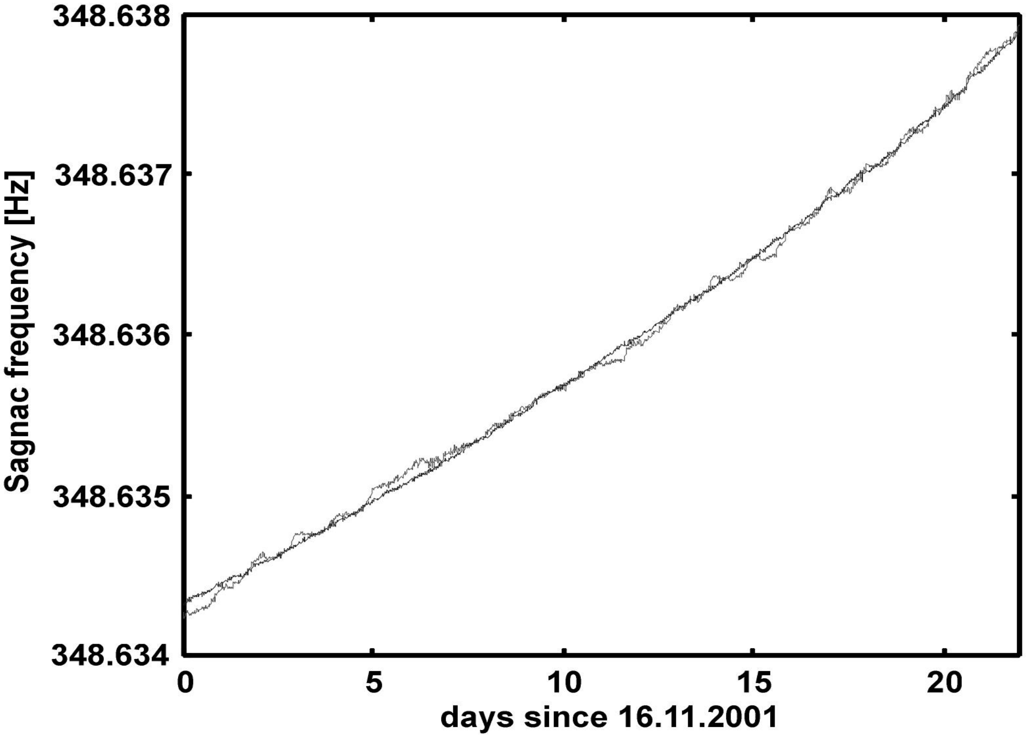

Figure 16: Dataset of Sagnac frequency measurements obtained in November 2001 (grey) and the fitted sensor model (black)

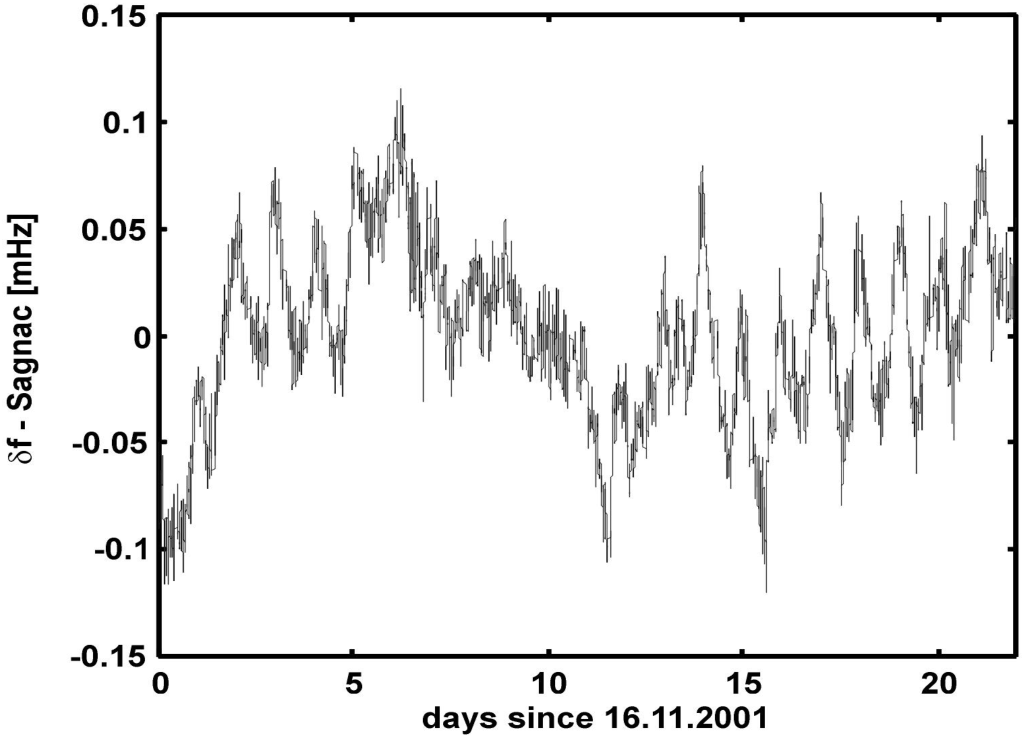

Figure 17: Residual plot of the measured Sagnac frequency and the model

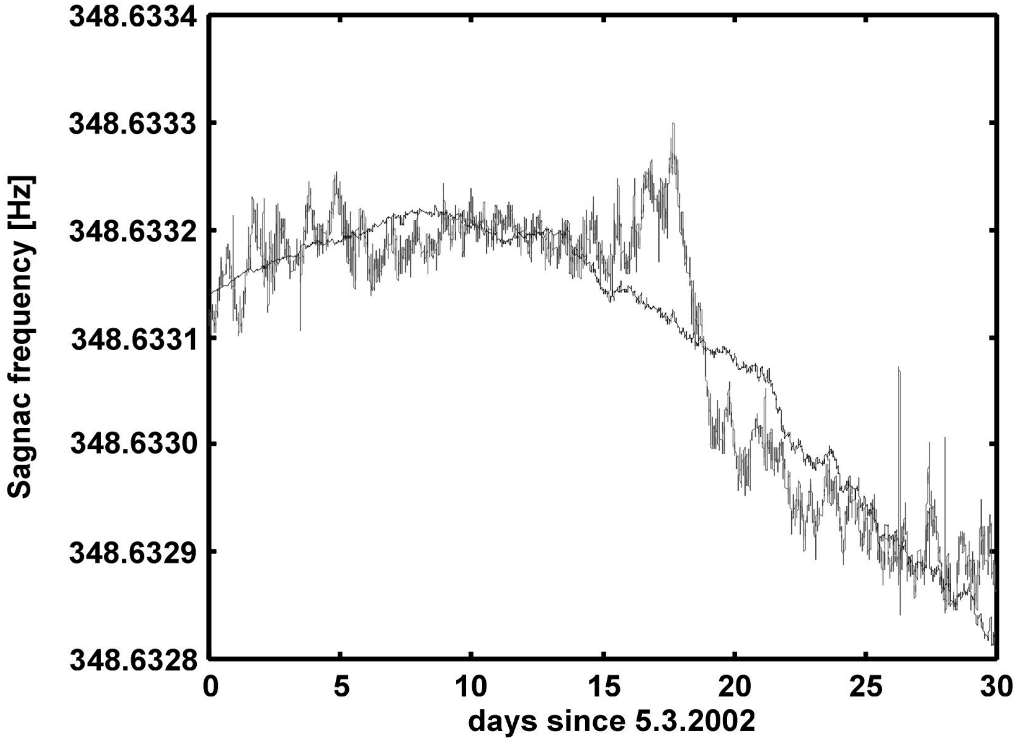

Figure 18: Dataset of Sagnac frequency measurements obtained in the period of March-April 2002 (grey) and the fitted sensor model (black)

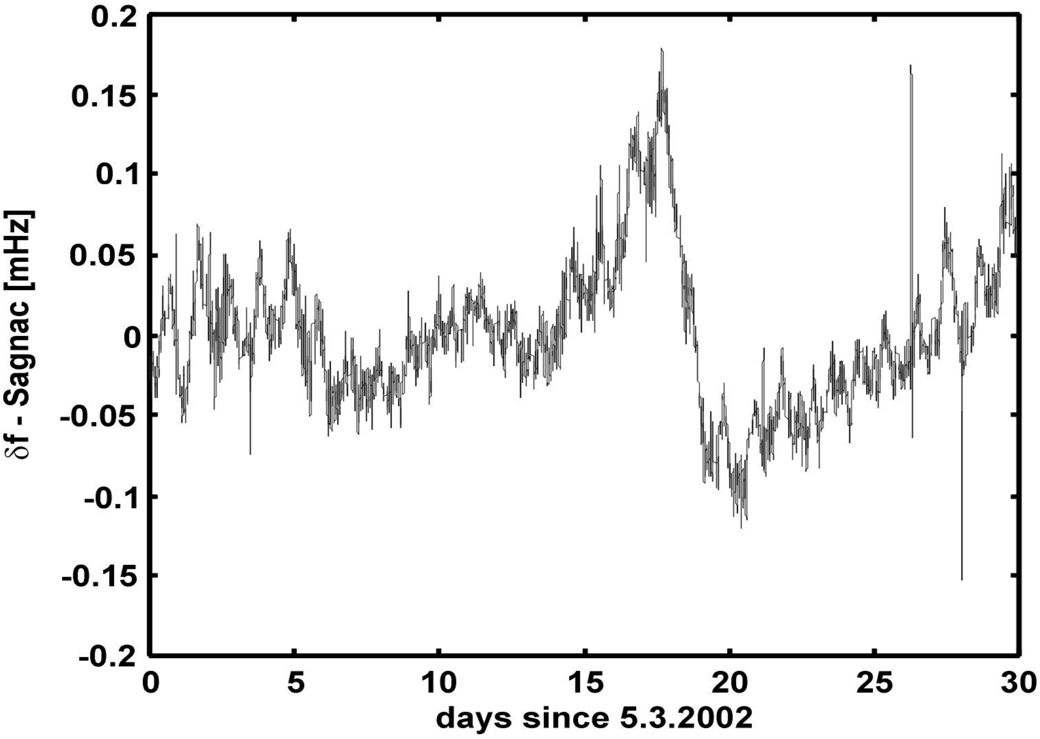

Figure 19: Residual plot of the measured Sagnac frequency and the model

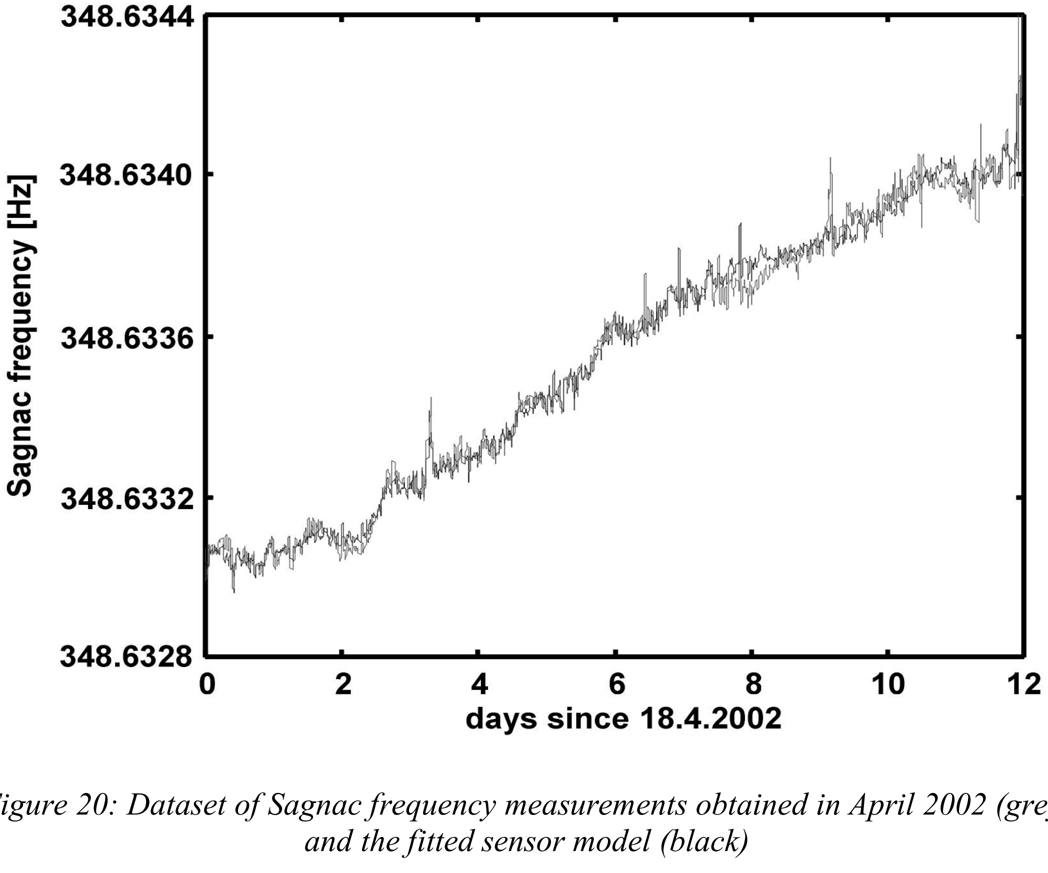

Figure 20: Dataset of Sagnac frequency measurements obtained in April 2002 (grey) and the fitted sensor model (black)

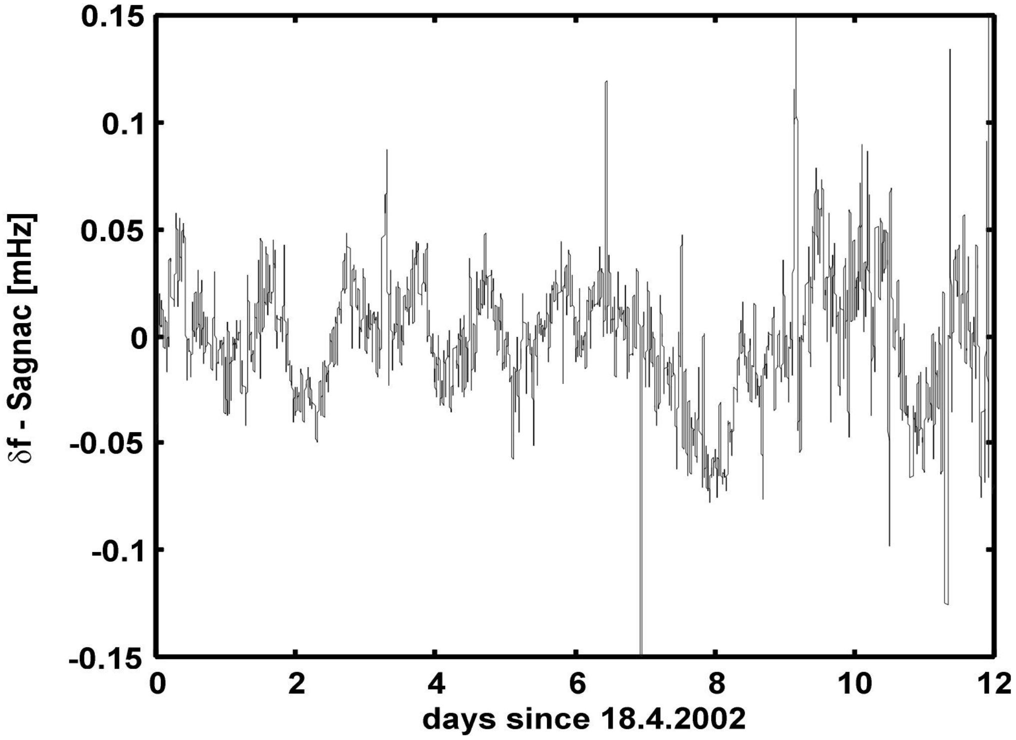

Figure 21: Residual plot of the measured Sagnac frequency and the model

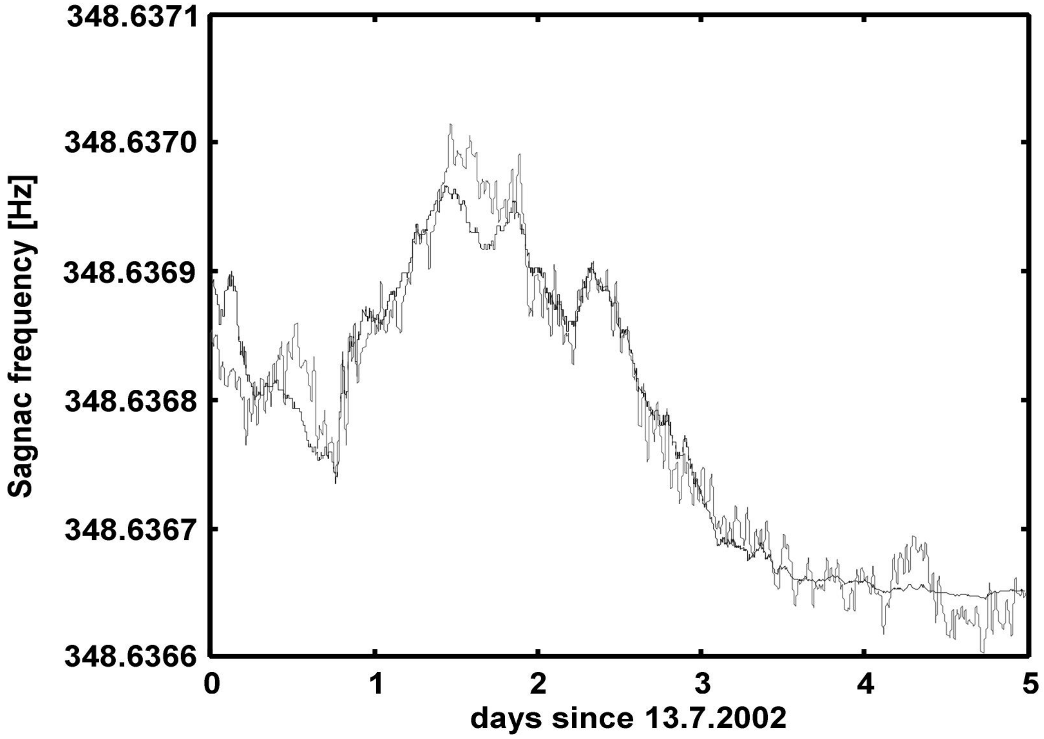

Figure 22: Dataset of Sagnac frequency measurements obtained in July 2002 (grey) and the fitted sensor model (black)

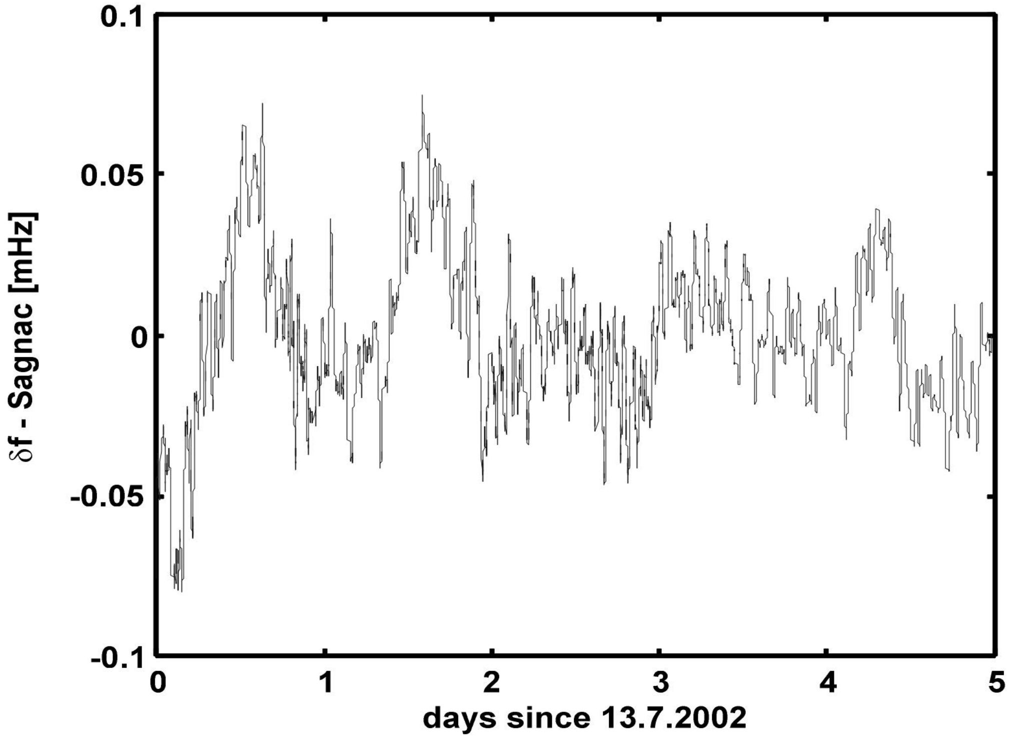

Figure 23: Residual plot of the measured Sagnac frequency and the model

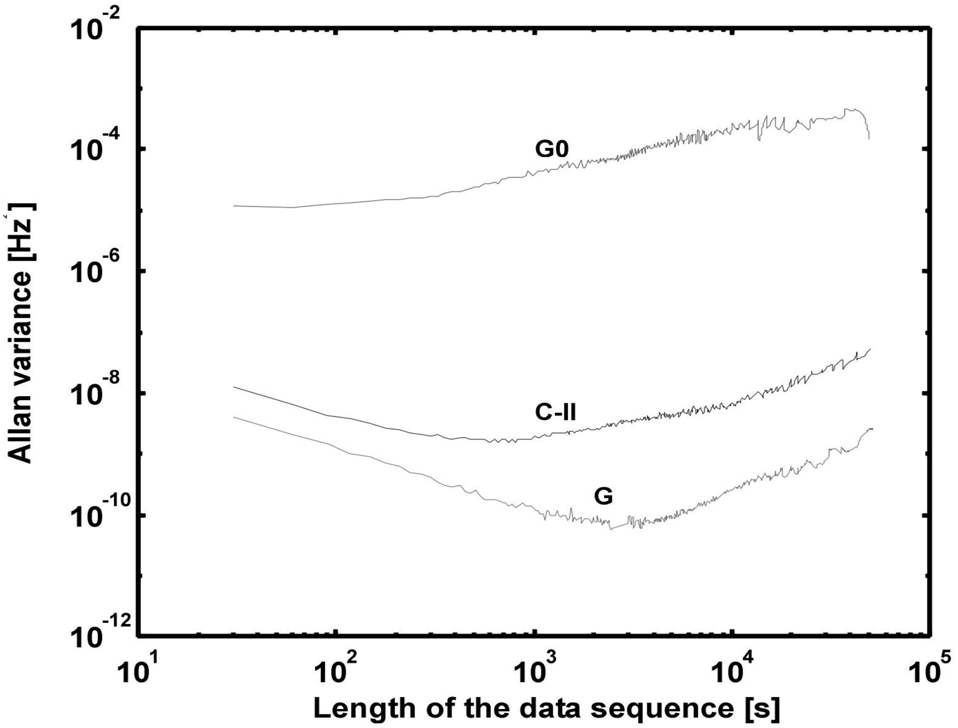

Figure 24: Relative Allan variance of the Sagnac frequency for C-II, G0 and G

In general one can see that the concept of increasing the ring laser perimeter is working well. The overall stability of the instruments increased along with the size (G0 does not fulfill this rule because of the simplicity of the construction). Figure 24 illustrates the quality of three of our currently operating rings.

The laser G0 was built by mounting the four corner structures independently on a vertical concrete wall in the Cashmere Cavern. The cavity is formed by stainless tubes and the mirrors used are of standard quality. It is considerably affected by the earth strains associated with tides and barometric pressure changes. Although similar in size to G, it has considerably poorer Sagnac frequency stability, mostly attributable to dimensional instability and a much higher level of backscattering [27].

As a result one can see that the G0 stability is not so good, but this is mostly due to the mirror cleanliness and the specific installation. Up to now the G is the most precise and stable operating large perimeter ring laser gyro.
The critical parameter of C-II, backscatter, is not of much concern in the case of G. The power feedback loop circuit is adjusted to maintain the stable monomode operation regime. The records of G data as well as those of C-II demonstrate that the photodiodes are particularly well suited for the purposes of the precise measurements. Further improvement of the data quality and increasing of the amount of available information on the operation parameters will help to built up a more precise and complete model for large RLG error correction.

4. Ring Laser orientation

When all instrumental errors of the ring laser are removed the remaining departure of the Sagnac frequency from a constant value corresponds to “natural” effects such as orientation changes of the ring laser relative to the rotational axis and fluctuations in the angular velocity of the earth. The former includes tidal effects as well as variations of the orientation of the rotational axis. In particular periodic signals of well-known origin are of interest since they can be used as a benchmark for the ring laser performance. Earth tides and ocean loading (for the location of Christchurch only) are such periodic signals, which involve variations of the orientation of the ring laser plane. Since ring lasers measure rotation absolute with respect to the local Fermi system, also diurnal polar motion becomes visible. We have used these known signals to evaluate the resolution of our ring lasers.

4.1 Diurnal polar motion

The diurnal polar motion is a nearly circular motion of the rotation axis of the Earth (i.e. rotation pole) with a time-varying amplitude and a period, which is equal to the sidereal day. The diurnal motion of the rotation pole is superimposed on longer period motions consisting mainly of the 14 months Chandler wobble and the annual and semiannual polar motion. The detailed study of the subject has been carried out by McClure [14], who developed the theory of diurnal polar motion for the case of a deformable Earth and computed amplitudes considering the rotation axis, angular momentum axis and figure axis. Correction for the liquid-core effects has shown that there is no significant difference between the results for rotation pole motion in both cases.

Since a ring laser measures the projection of the Earth rotation rate on the normal vector of the ring laser plane, small variations in the position of the rotation axis result in a measurable signal. This effect is equivalent to the diurnal latitude variations of the ring laser location. Using the results obtained by McClure, Brzezinski [14,6] and adopting an Earth-body fixed coordinate frame, the polar position with regard to each diurnal component can be calculated by multiplying a particular amplitude of rotation axis motion by –sin(arg.) and cos(arg.) respectively. Each argument is represented as a linear combination of the Greenwich mean sidereal hour angle ϕ_M and fundamental arguments of nutation theory F with corresponding integer coefficients c.

$$\Delta\varphi = \sum_i - A_i \sin(\phi_M + \sum_j c_{ij} F_j)\,,\ \Delta\varepsilon = \sum_i A_i \cos(\phi_M + \sum_j c_{ij} F_i) \tag{53}$$

where $\Delta\varphi$ are longitude diurnal variations and $\Delta\varepsilon$ are obliquity diurnal variations. The fundamental arguments are:

Mean anomaly of the Moon

$F_1 \equiv l = 134.^\circ 96340251 + 1717915923.''2178t + 31.''8792t^2 + 0.''051635t^3$,

Mean anomaly of the Sun

$F_2 \equiv l' = 357.^\circ 52910918 + 129596581.''0481t - 0.''5532t^2 + 0.''000136t^3$,

Difference between the mean longitude of the Moon and the mean longitude of the ascending node of the lunar orbit

$F_3 \equiv F = 93.^\circ 27209062 + 1739527262.''8478t - 12.''7512t^2 - 0.''001037t^3$,

Mean elongation of the Moon from the Sun

$F_4 \equiv D = 297.^\circ 85019547 + 1602961601.''2090t - 6.''3706t^2 + 0.''006593t^3$,

Mean longitude of the ascending node of the Moon

$F_5 \equiv \Omega = 125.^\circ 04455501 - 6962890.''2665t + 7.''4722t^2 + 0.''007702t^3$,

where t is measured in Julian Centuries of 36525 days of 86400 seconds since J2000. The Greenwich mean sidereal hour angle ϕ_M relates to the Greenwich Mean Sidereal Time (GMST) as follows:

$$\phi_M = GMST \frac{2\pi}{86400} + \pi + 2\pi d_u\,, \tag{54}$$

$$GMST = 24110^s.54841 + 8640184^s.812866T_u + 0^s.093104T_u^2 - 6^s.2 \times 10^{-6} T_u^3\,, \tag{55}$$

where $T_u = d_u / 36525$, d_u is the number of days elapsed since 2000 January 1, 12h UT1. Inserting the position of the ring laser in Wettzell as φ the corresponding longitude must be added to the Greenwich mean sidereal angle as follows:

$$\phi_L = GMST \frac{2\pi}{86400} + \pi + 2\pi d_u + \varphi\,. \tag{56}$$

The tables given in McClure provide up to 160 values of diurnal polar motion amplitudes and coefficients. However only the largest values contribute to the polar motion. When we apply only 6 coefficients for example, all the others together are contributing less than 1×10^{-3} seconds of arc of amplitude of pole variations. This is clearly beyond our instrument resolution, so we're using only those 6 largest coefficients in our calculations. Figure 25 shows the computed diurnal part of the latitude variations for Wettzell for a period in January 2002.

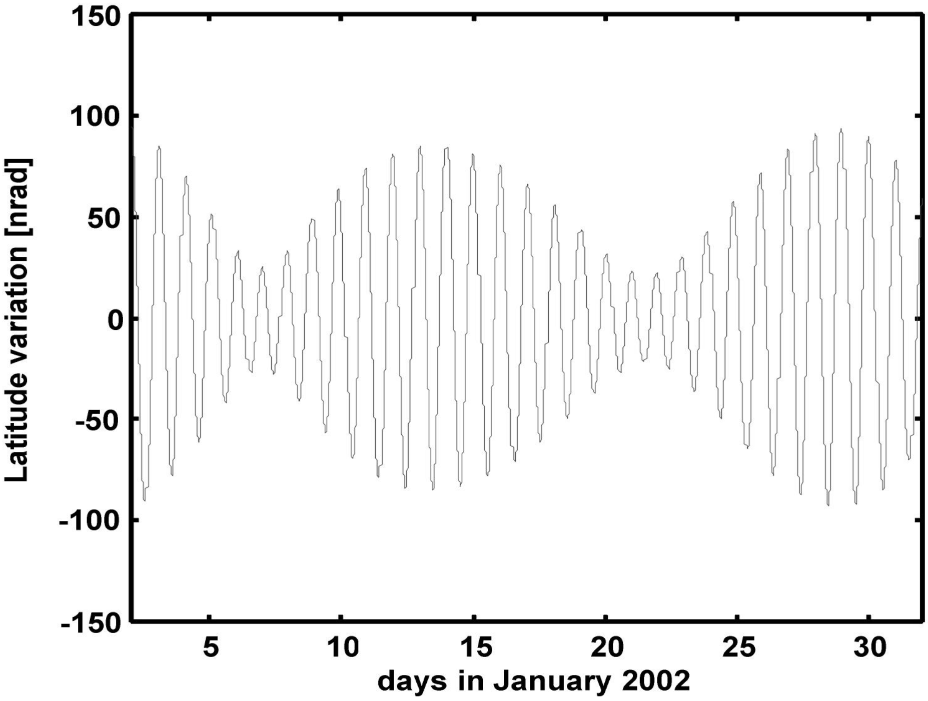

Figure 25: An example for one month of calculated polar motion data. The maximum amplitude is 94.5 nrad

The 18 largest coefficients from Brzezinski were used in the computation. The resulting "latitude oscillation" has two main components with a periodicity of sidereal length of day and about 14 days. The maximum amplitude corresponds to 0.02 seconds of arc. It is important to note that this polar motion model has been developed for nutation corrections in VLBI and our ring laser as an inertial rotation sensor is the only experimental proof so far, which can confirm this theory quantitatively by direct measurements. Similar consistent results were found for the independently operating UG1 ring laser in Christchurch.

4.2 Solid earth tides and ocean loading

Solid earth tides are also modifying the value of the observed Sagnac frequency (δf) of large ring lasers because they are changing the orientation of the ring laser plane with respect to the earth rotation vector (1).

$$\delta f = \frac{4A\Omega}{\lambda P}\cos(90^\circ - \phi + \delta\varphi(t)) \qquad (57)$$

$\delta\varphi(t)$, measured with respect to the local g, represents small periodic variations of the orientation of a ring laser in the range of up to 300 nrad when both earth tides and ocean loading are acting on the location of the ring. ϕ corresponds to the latitude of the location of the respective instrument. Since both ring lasers C-II and G are equipped with tiltmeters, measurements of $\delta\varphi(t)$ are available and may be used to correct the raw measurements of large ring lasers. In a long timeseries of ring laser measurements one can identify two different types of orientation variations. The first component is periodic and is caused by the gravitational attraction of the orbiting moon. The second component is arbitrary and corresponds to a drift in the monument orientation. This reflects a response of the ring laser monument to slow environmental changes such as seasonal temperature adjustment, groundwater table variations, aging of the monumentation and so on.

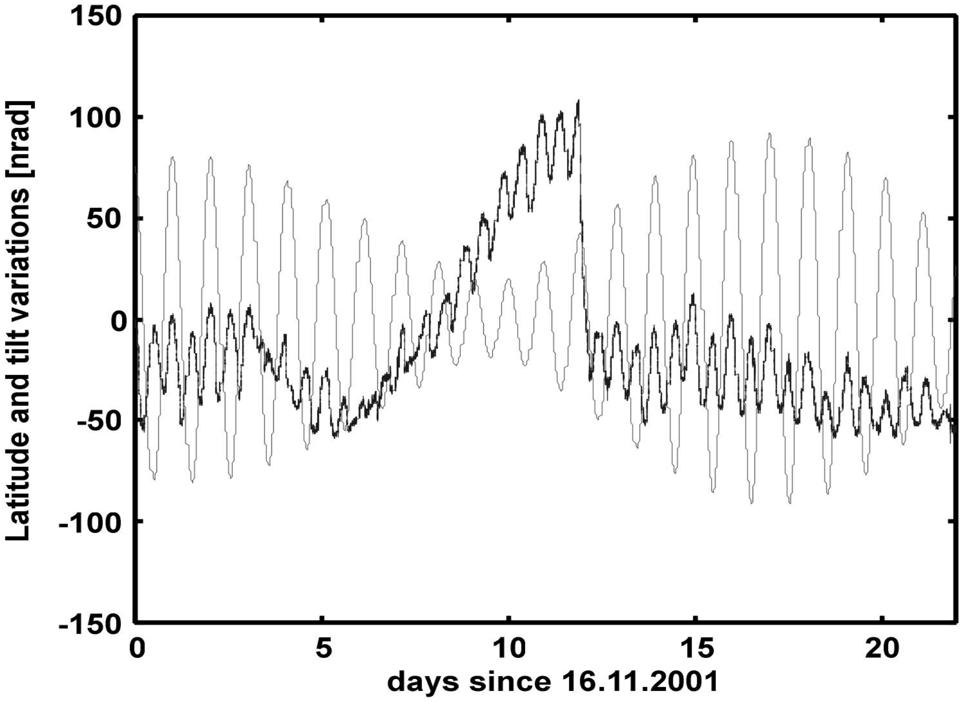

Figure 26: The contribution of diurnal polar motion (grey) and instrumental tilt (black) relative to local g for the timeseries started at 16.11.2001

The first component is periodic and can be obtained from model calculations readily [6]. Therefore it serves for benchmarking purposes. At the same time the arbitrary component is much more difficult to extract from the ring laser output data and requires a continuous high resolution monitoring of the ring laser site. Figure 26 represents the contribution to orientation changes in $\delta\varphi(t)$ for both geophysical signals as discussed above.

The red curve is the computed "global" orientation change (diurnal polar motion), usually considered as latitude variation of the observation position. It has maximal amplitude of about 90 nrad or 60 cm in linear scale. The blue curve represents the tiltmeter data, i.e. the "local" orientation change. In addition to the 12 hours period tidal components one can see the pure pillar orientation variations, especially remarkable is this abrupt inclination of the ring laser basement at 28.11.2001 (day 12 on the graph), which presumably was caused by changes of the ground water level [19].

4.3 Geophysical signals in ring laser data

For the first timeseries of G ring laser data (see chapter 3.2) we have calculated the required corrections for orientation variations during the ring laser measurements. Figure 27 shows the superposition of the Sagnac frequency residuals after the application of the sensor model as discussed in chapter 3 and the signal contributions from geophysical sources, mentioned in chapter 4.2.

One can clearly see the correspondence in phase and mostly also in amplitude between the measured quantity and the theory. Keeping in mind that the Sagnac frequency itself is around 348.636 Hz, the residual peak-to-peak error for the worst part in the entire dataset is smaller than 0.5 ppm of the total measurement value.

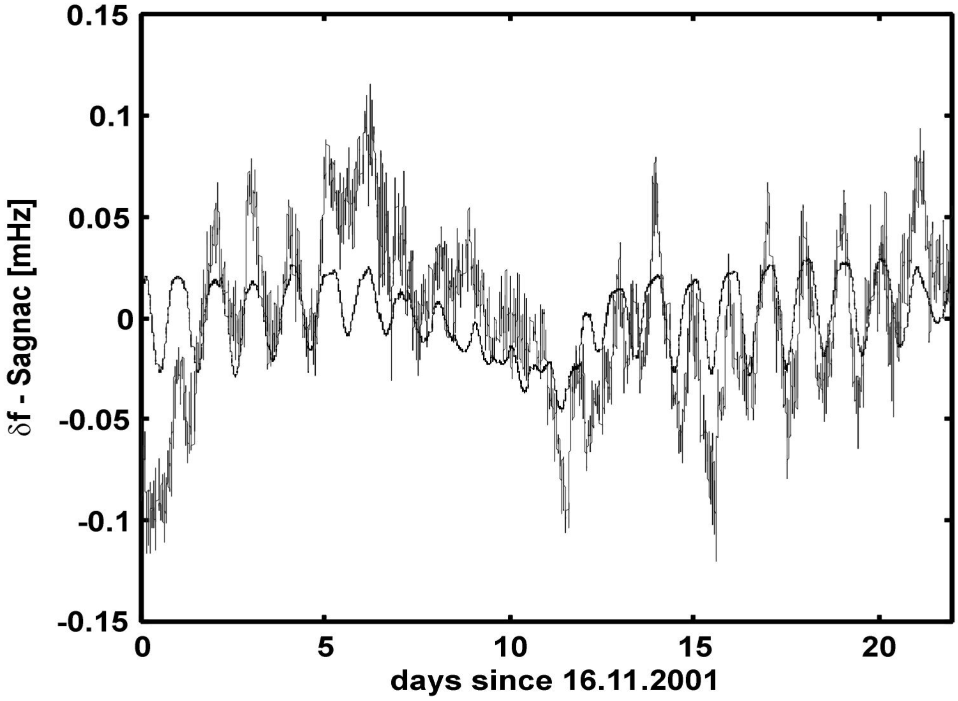

Figure 27: The superposition the sensor-model corrected Sagnac frequency (grey) and the calculated signal from geophysical sources (black)

There are several possible reasons for this model defects.

- The real signals such as external rotation or micro-seismicity can produce the short-term discrepancies and increased noise level of the original signal. Those effects are hard to compensate or identify since there are no other reference devices except for the ring laser itself. Bandpass filtering may be applied to reduce the noise.

- The stability of all environmental and instrumental parameters is extremely important for the ring laser data quality. Those parameters should not only be stabilized by hardware means as good as possible, but must also monitored properly without detector artifacts. As the ambient conditions for G RLG are close to equilibrium at the time of writing this thesis, any detector-related error has become critical for the model. Some of the discrepancies between model and real data might be due to these effects, thus limiting the model abilities.

4.4 The results discussion for G and C-II

The comparison of the postprocessed timeseries for two large ring laser gyroscopes must take into account the superior stability and sensitivity of G over C-II. However the environmental conditions created for the G are much better in terms of temperature stability. While C-II has been encapsulated into the pressure stabilizing vessel the temperature variations in the Christchurch laboratory proved to be very critical for the operation. Based on the modeling there are two major error sources competing to be critical.

On the one hand there is quite a substantial trend in the modeled timeseries associated with the temperature induced optical frequency shift. This is still a task for a further investigation for which the optical frequency measurement experiment is under preparation. The on-the-fly measurements of the optical frequency departure from the center line could be incorporated into the model for the Sagnac frequency drift correction. While the stabilizing of the optical frequency via hardware (i.e. pathlength control) is impossible and undesirable for the large ring lasers, the information about its drift might help to remove the corresponding errors during postprocessing. While the backscattering is practically absent, or at least undetectable in the G ring laser, the optical frequency shift is believed to be one of the major threats for the operational stability.

On the other hand, and this is especially noticeable in case of G ring, the active medium parameter fluctuations are also very important. The “ultimate” stability has to be achieved for the ring laser operational conditions. It also includes the stable RF power supply since the variations of the driving power affect the refractive index of the plasma and change the gain settings. Non-reciprocity inside the cavity produces a null shift, which is also susceptible to the active medium parameters. The balance of the counterrotating wave intensities should be kept constant which is currently realized via a feedback control loop.

A specific error source in ring lasers is a susceptibility to an external magnetic field based on Faraday or Zeeman effect. This effect can be observed when polarization of the counterpropagating waves in the ring laser contour deviates from linear. However as long as the G ring is operating, no correlation of the Sagnac frequency with the magnetic field fluctuations was observed. The experiments for the polarization estimation showed that its departure from planar is undetectable.

Two ring laser accuracy degrading factors that cannot be easily avoided are the outgassing inside the cavity and the instability of the mirror optical axes and their surface erosion. These will eventually lead to backscattering effects and lower the Q factor. The observation of the ring operation shows that these effects are indeed important, however without such a dramatic decrease of the Sagnac frequency stability.

While the long-term stability and operation is important for fundamental studies of the low period Earth rotation variations and polar motion another application of large ring lasers was developed over the last few years. The seismically induced rotation rate fluctuations were recorded quite frequently by the different gyroscopes. This shows the great potential of the large ring laser as an instrument for investigation in the field of geodesy. The following chapters are dedicated to the latter activity in the ring laser research project with respect to the seismology.

5. Ring Laser Gyroscopes for seismic studies

5.1 Introduction

The ring laser is sensitive to absolute rotation, i.e. within its resolution it can detect any variations of rotation rate around the sensitive axis. Since large ring lasers possess such a superior measurement resolution, that they are able to register daily motion of the instantaneous rotation pole, it is reasonably to expect from these instruments the detection of other effects. One of those effects is a variation of rotation rate caused by earthquakes. From the early stages of the Large RLG project the noticeable disturbances of the beat frequency caused by teleseismic events (distant earthquakes) have been regularly observed [15,20]. As an example Figure 28 demonstrates simultaneous record of seismically induced linear velocities (conventional seismogram) and rotation rate from an earthquake in Algeria (21.05.2003, M=6.8). The distance between the quake epicenter and detector is about 1550 km.

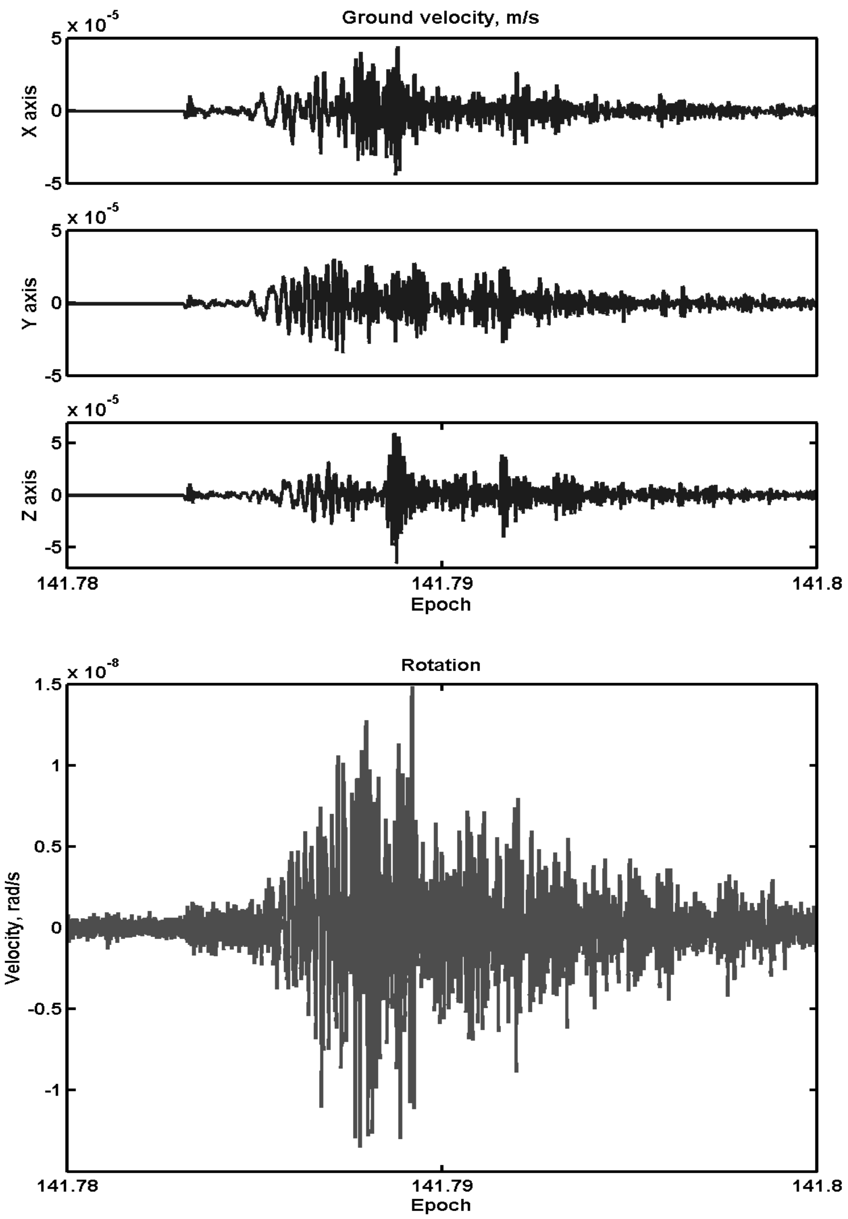

Figure 28: The ground velocities and rotation rate due to Northern Algeria Earthquake, 21.05.03, M=6.8 recorded by G ring and STS-2 seismometer in Wettzell

Over the last two years a number of quakes, varying from teleseismic to local class of events, were recorded by the ring laser G located in Wettzell, Germany. Figure 29 illustrates the paths of the seismic wave propagation from the quakes epicenters to the location of the G ring laser gyroscope and standard STS-2 broadband seismometer.

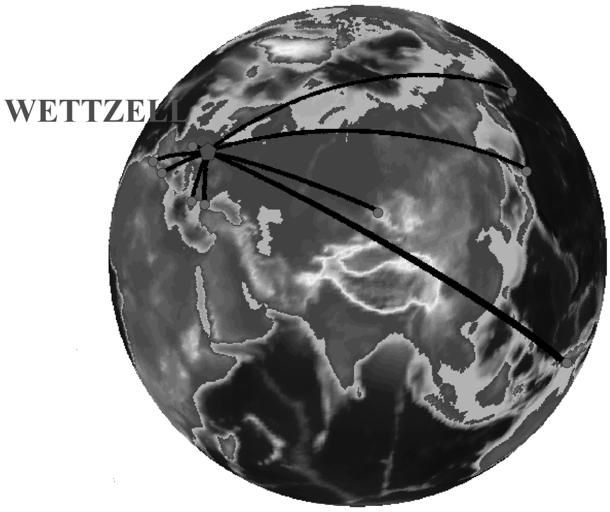

Figure 29: Map of earthquakes recorded by ring laser G in Wettzell during years 2003-2004

These observations provided the evidence that ring laser gyroscopes are suitable instruments for the measurement of seismic rotations. The recording of rotational seismograms is expected to be useful for various aspects of geophysical research such as estimation of permanent displacement from seismic recordings, further constraining earthquake source processes etc. [8]. There are 6 degrees of freedom for a movement in space, 3 degrees of rotation and 3 degrees of translation. Until today only translations have been recorded.

Since the G ring laser is a stationary deployed device, one needs an instrument with similar accuracy but at the same time smaller in size/weight and preferably modular for easier transportation and installation. Based on these conditions, the demonstrator system named GEOsensor has been developed. Its goal is to demonstrate the ring laser technology abilities for measurements of the local and teleseismic events in seismically active regions. In the following chapters the design conception, realization and test results from GEOsensor will be discussed.

5.2 Theory of seismic rotation

The general cause of earthquakes is tectonic activity associated with plate boundaries and faults. A fault is a large fracture line, across which the rocks are moved. The initial movement that causes seismic vibrations occurs when stresses in the Earth reach a level greater than strength of the rock and two sides of a fault abruptly slide past each other. The concentric shock waves then move out from the source (focus) of the quake. These waves produce the ground motion both linear and rotational. There are many different seismic waves, but mainly considered are four types:

- Compressional or P wave (for primary)
- Transverse or S wave (for secondary or shear wave)
- Love wave
- Rayleigh wave

The first two types, P and S are called body waves because they propagate through the body of the Earth. The latter two are called surface waves since they travel along Earth's surface. They all have different amplitudes and travel times and produce rotational motion of the ground except for P-wave which moves the matter in a contraction-expansion way. Nevertheless the P-wave can cause rotation when it reflects from the Earth surface and generates S-wave (known as P-S conversion). The shear and Rayleigh waves cause rotation in the vertical plane while Love waves generate rotation in the horizontal plane.

The conventional seismometers determine three components of linear displacement. In addition the three components of rotation would be necessary to obtain the full body motion description. The seismically induced rotation rate (vorticity) can be written as

$$\Omega_S = \begin{pmatrix} \omega_x \\ \omega_y \\ \omega_z \end{pmatrix} = \frac{1}{2}\nabla \times V = \frac{1}{2}\begin{pmatrix} \partial_y V_z - \partial_z V_y \\ \partial_z V_x - \partial_x V_z \\ \partial_x V_y - \partial_y V_x \end{pmatrix} \tag{57}$$

where V_i, $i=x,y,z$ are the components of the velocity field V, the time derivative of the deformation field U [20]. The corresponding Sagnac frequency also includes such terms as strain and tilt that arise from the changes in perimeter, area and orientation of the ring during the seismic event. However the strain is much smaller than the actual seismic rotation and is difficult to detect while the tilt input is usually no more than a few percent of the magnitude of the rotational signal and can be detected independently and corrected for.

For the teleseismic waves, particularly Love and shear waves, there should be a similarity in phase for the vertical component of the rotation rate and translational acceleration [8]. Considering the transversely y-polarized plane signal A traveling in direction x with constant phase velocity V_P we can write the displacement equation as:

$$U_y(x,t) = A(t - x/V_P) \tag{58}$$

and the corresponding y-acceleration then is:

$$dU_y(x,t)/dt^2 = A''(t - x/V_P) \tag{59}$$

The rotation rate can be expressed as follows:

$$\frac{1}{2}\partial_x V_y = \frac{1}{2}\left(\partial_x U_y'(x,t)\right) = \frac{1}{2}\partial_x\left(A'(t - x/V_P)\right) = -\frac{1}{2V_P}A''(t - x/V_P) \tag{60}$$

Therefore the acceleration and rotation rate show similar phase as demonstrated in expressions 58-60. The conversion factor is proportional to the wave phase velocity. The magnitude of the Love wave seismic velocity can be varying within the range of 3000 up to 6000 m/s. For the teleseismic event there are no substantial changes of the value of the incoming Love wave expected as well as no variations in the direction. Assuming the wave propagation direction being an orthodrome, the directional angle of the incident wave can be calculated by using the following expression

$$\tan(BA) = \left(\sin(\lambda_1 - \lambda_2)\cos(\varphi_2)\right) / \left(\cos(\varphi_1)\sin(\varphi_2) - \sin(\varphi_1)\cos(\varphi_2)\cos(\lambda_1 - \lambda_2)\right) \tag{61}$$

where BA – the back azimuth or directional angle from the point of the receiver to the wave source; (φ_1,λ_1) and (φ_2,λ_2) – coordinates of the receiver and the quake location respectively. The seismograms are measured in North-South, East-West and vertical direction. Since we need to extract the translational components of the seismogram, we have to write down the projections measured by the seismometers on their NS and EW axes.

$$\begin{cases} NS = D\cos(K) - T\sin(K) \\ EW = D\sin(K) + T\cos(K) \end{cases} \tag{62}$$

where D – directional wave component, T – transverse component and K – azimuthal direction of the wave propagation at the point of receiver. The final expression for the translational component is

$$T = EW\cos(K) - NS\sin(K) \tag{63}$$

Figure 30 shows the diagram illustrating expression (63). Blue "North" and "East" axes are the corresponding sensitivity axes of the seismometer along which the NS (north-south) and EW (east-west) components of the ground velocities are measured.

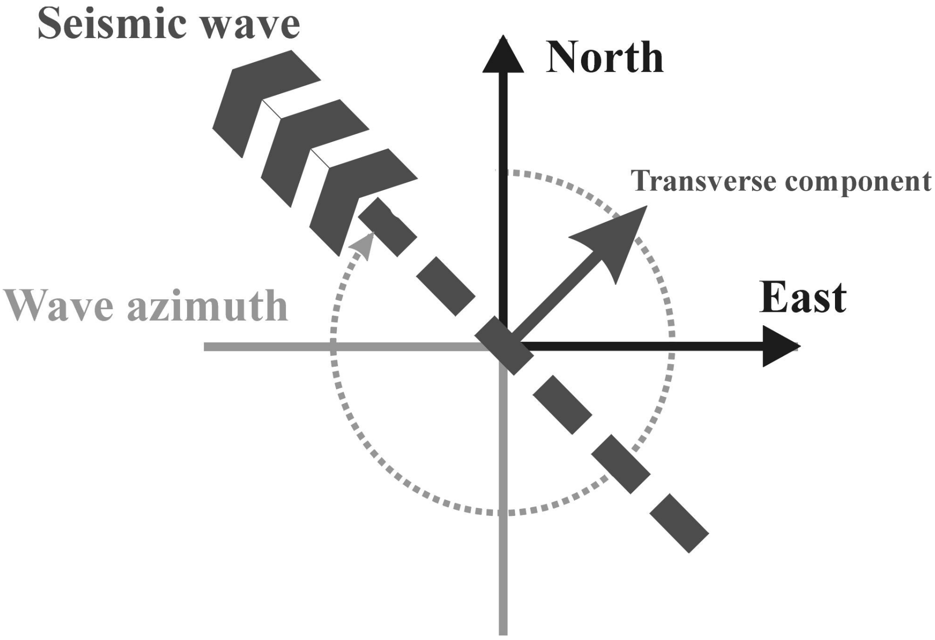

Figure 30: Determination of transverse component of seismic wave

After the ground velocities are differentiated with respect to time in order to obtain accelerations and wave azimuth according to (61), the transverse acceleration can be calculated. The seismically induced rotation rate can then be obtained by dividing the transverse acceleration by twice the horizontal phase velocity. Both signals should be equal in phase and amplitude.

5.3 Requirements for earthquake detection by the Large Ring Laser

In standard seismology the earthquake induced rotation has been neglected because the corresponding magnitudes were thought to be small [1] and no instruments with required resolution existed.

The superior resolution of large ring lasers along with their insusceptibility to acceleration makes the application of these instruments very attractive for seismological studies. The expected range of angular velocities to be measured is estimated as $10^{-14}\,rad/s \le \Omega_S \le 1\,rad/s$ and the signal frequency range for the seismic waves is $0.003Hz \le f_S \le 10Hz$ [27]. The different orientation of the ring lasers can provide the detection of rotation from shear, Love and Rayleigh seismic waves.

The resolution of the ring laser gyroscope is proportional to the area enclosed by the beam path. Therefore the increase of the size of a ring leads to a sensitivity improvement. For example, the 4 by 4 meters square ring laser G installed in fundamental station Wettzell, Germany has a resolution of $\delta f = 9 \cdot 10^{-11} rad/s$. It is a very high sensitivity that is good enough for the detection of both teleseismic waves and small near field events. In case of the seismic application of a ring laser the long-term stability of an instrument is not so important as for the Earth rotation variation measurements. More critical is the short-term precision and mechanical rigidness of the laser beam path for stable monomode operation. The instrument should be capable of accurate seismic rotation detection while keeping its design parameters constant. At the same time the whole system should be transportable, cost effective and provide a relatively easy installation.

5.3.1 Mechanical design

Another important issue is whether all the ring lasers have the same response on quake induced rotational rate or not. C-II and G ring are monolithic and semimonolithic respectively, while UG is a vacuum tube system tied to the ground. This type of large ring laser uses either a concrete base plate or a rock formation as a geometrical reference. For the transportable measurement system like GEOsensor the latter approach is more favorable. It has to be shown that this approach does not compromise the measurements.

To answer this question the direct comparison of two earthquake induced rotation rate records has been made. The raw Sagnac data were taken from C-II and UG ring lasers during Fiji earthquake in august 2002. These data have been carefully processed for accurate Sagnac frequency estimation. The raw photodetector output signal is divided into bins, each being 0.05 seconds long, which is equivalent to the 20 Hz acquisition rate (see section 6.3 for details). Then the signal is interpolated within each section in order to obtain accurate zero crossing positions and the Sagnac frequency is determined using the number of zero crossings per time window. The determined frequency is converted into a rotation rate using the basic Sagnac equation. Finally the resulting rotational seismograms from two different ring lasers are superimposed and this

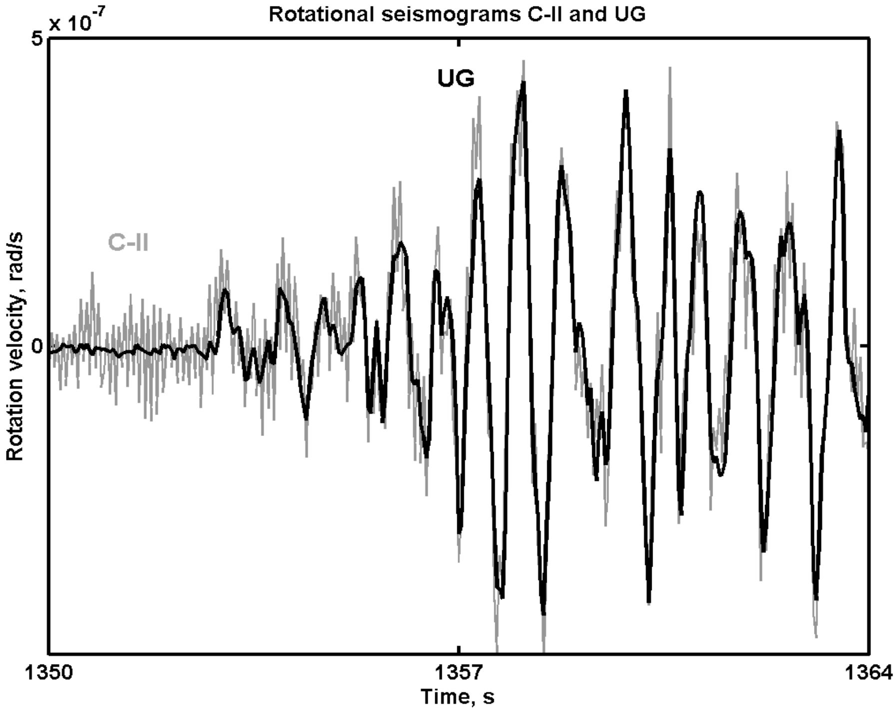

Figure 31: Comparison of two RLG rotation rate during FIJI Earthquake, 19.08.2002, M=7.7

comparison is shown on Figure 31. One can see a very good agreement between the two instruments both in phase and amplitude, which remains the same all through the length of the event record. The fact that two substantially different devices both in resolution and design produce nearly identical results during the earthquake is very encouraging. This gives the opportunity to merge the best qualities of two design approaches – superior mirrors and high, as near to monolithic construction as possible stability on one hand and mobility, installation flexibility and cost-effectiveness on the other.

5.3.2 Tilt contribution to rotation

In order to proof that the observed rotational rate is not caused by orientational changes of the ring plane due to the quake the corresponding tiltmeter data were converted into the rotation rate change according to the following expression

$$\Omega_{TILT} = \left(\Omega \cdot \sin(\varphi)\cos(T_{NS}) - \Omega \cdot \cos(\varphi)\sin(T_{NS})\right) \cdot \cos(T_{EW}) \tag{64}$$

where Ω_{TILT} is the tilt equivalent rotation rate, Ω - Earth rate, φ - ring laser location latitude, T_{NS} and T_{EW} are instrument tilts in North-South and East-West directions respectively. Since the East-West tilt component is under cosine function, which is usually close to 1, for all practical purposes it can be ignored, and the formula (64) becomes

$$\Omega_{TILT} = \Omega \cdot \sin(\varphi - T_{NS}) \tag{65}$$

The result of this calculation is illustrated in Figure 32. As one can see the tilt contribution to the overall response does not exceed 5% and can be corrected from an independent sensor quantity by subtraction of the tilt equivalent rotation rate change from the ring laser signal.

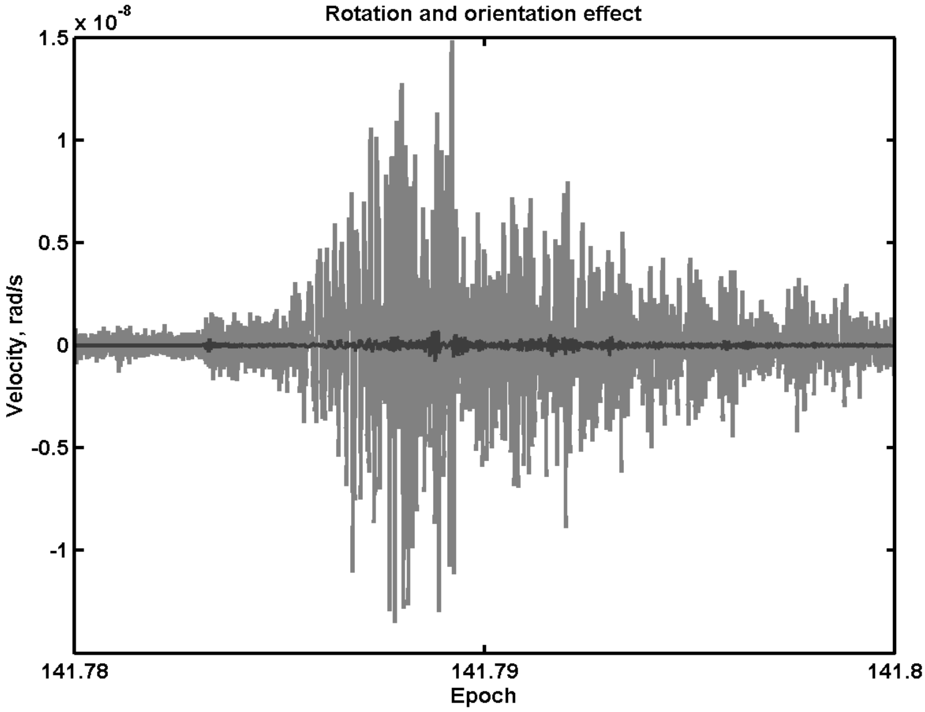

Figure 32: The rotation rate (grey) and converted tilt (black) taken from the Northern Algeria Earthquake, 21.05.2003, M=6.8

5.3.3 Possible signal dependent limitations

Another important issue concerning the seismic rotation detection is a limitation of the ring laser in terms of the amplitude of the incoming signal. The following example gives some idea about these boundaries. This is an earthquake in New Zealand that occurred at 29.09.2003, 40 km North-East of Christchurch, magnitude 4.7. The small distance between the instruments location and the quake focus makes this event a serious test for the ability of the ring lasers to adequately detect short-range seismic shakes. All the rings, C-II, G0 and UG-1 continued to run, however the UG-1 readings are unusable because of combination of large (a few hundred Hz around the 1513 Hz) amplitude variations and undersampling. The C-II and G0 produced good results in comparison. The sampling frequency of the frequency demodulator is 10 Hz thus the signal was heavily aliased and only the major signature of the incoming rotation can be recognized. The careful frequency estimation (see method description in section 5.3.1) of the C-II and G0 raw readings shows that the minimum bandwidth required for appropriate rotational signal extraction is 10 Hz which corresponds to the sampling interval of 0.05 seconds as standard in seismology. Here we made two estimations with bandwidths of 10 Hz (20 Hz acquisition rate, 0.05 s time window) and 20 Hz (40 Hz acquisition rate, 0.025 s time window). Figure 33 illustrates the accuracy difference of the frequency estimation with two sampling rates on the first phase of the quake.

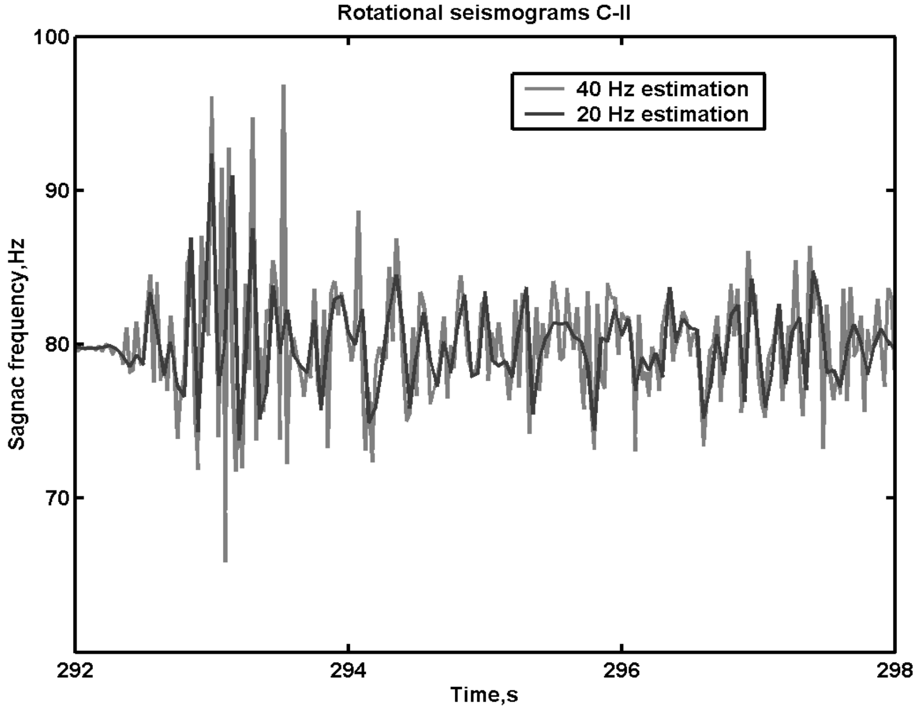

Figure 33: New Zealand Earthquake local rotational seismograms reconstructed from different frequency estimation rates

One can see signal components with a frequency higher than 10 Hz, however this resolution makes no sense on the larger part of a signal, where the 20 and 40 Hz estimated frequencies are nearly identical (Figure 34). The variations of rotation rate here are large and fast, hence the 0.025 seconds time window estimation is not able to resolve the changes while a 0.05 seconds time window estimation produces more reliable results. Thus by applying standard for seismology 20 Hz acquisition rate one has to keep in mind that this is still a compromise between time and amplitude resolution.

The Earth rotation rate, which is a natural rate-bias for the Sagnac frequency signal, has not been smaller for the detection of seismic frequency changes than the measurements of both C-II and G0. So far the Earth rate is large enough to avoid the zero-crossing in the Sagnac frequency determination for these particular instruments. However the bias problem must be regarded with some attention with respect to the instrument location. The New Zealand earthquake produced the rotation amplitude of about 4.4×10^{-5} rad/s

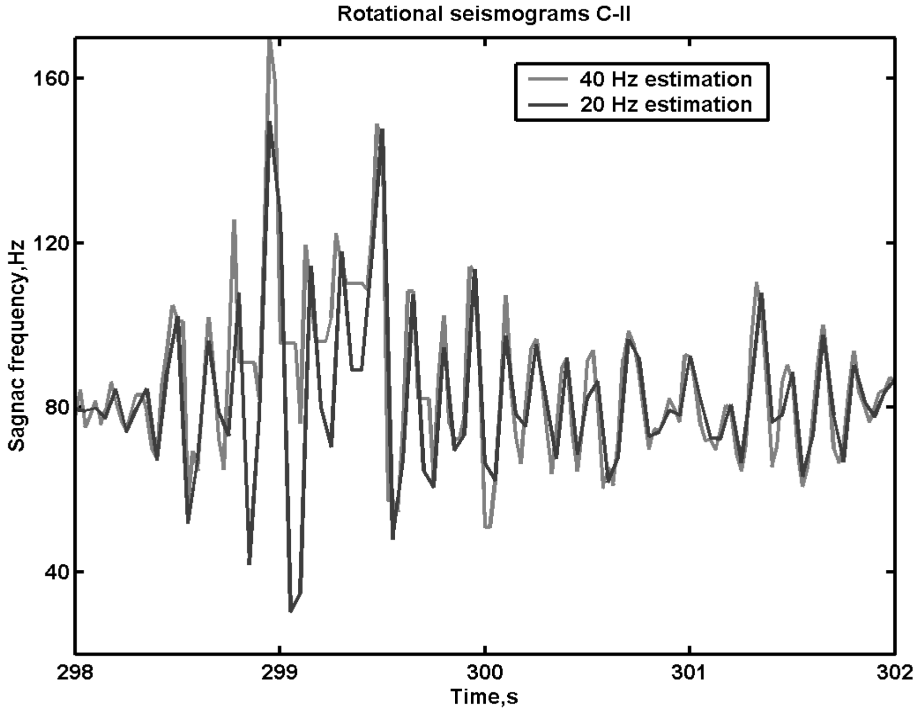

Figure 34: New Zealand Earthquake rotational seismograms obtained via different frequency estimation rates

while the Earth rate bias at the Christchurch latitude of 43.57694° is 5×10^{-5} rad/s. Therefore for the latitudes below 38° the frequency variations due to the seismical impact may eventually not be resolved unambiguously by the ring lasers for the earthquakes with the similar or stronger rotational amplitudes and with the same range of distance between the focus and instrument location as for the New Zealand earthquake. In such a case the Earth rate is not enough to cover all the range of the frequency variations. Since the ring laser in its present form does not sense the direction of rotation the Sagnac frequency will cross the zero and until the next zero crossing the trend will be inverted. Because these zero crossings are very short the Sagnac frequency will be still available but to establish the proper rotation rate magnitudes additional postprocessing will be required. It is better if this kind of difficulties are avoided for most of the time.

6. GEOsensor design

The GEOsensor is a stand-alone measurement complex for seismic and geophysical studies. It consists of several major components; a large perimeter one-axis ring laser gyroscope, a conventional three axis broadband seismometer, a tiltmeter to monitor changes in the orientation of the ring laser component and a GPS-station to provide time and reference frequencies for the data acquisition system. Figure 35 shows the principal structure of the GEOsensor. Auxiliary instrumentation such as thermometers a barometer and laser power meters are used for diagnostic purposes in the evaluation phase of the GEOsensor. Since the most interesting datasets for seismic studies are expected in the areas of high earthquake

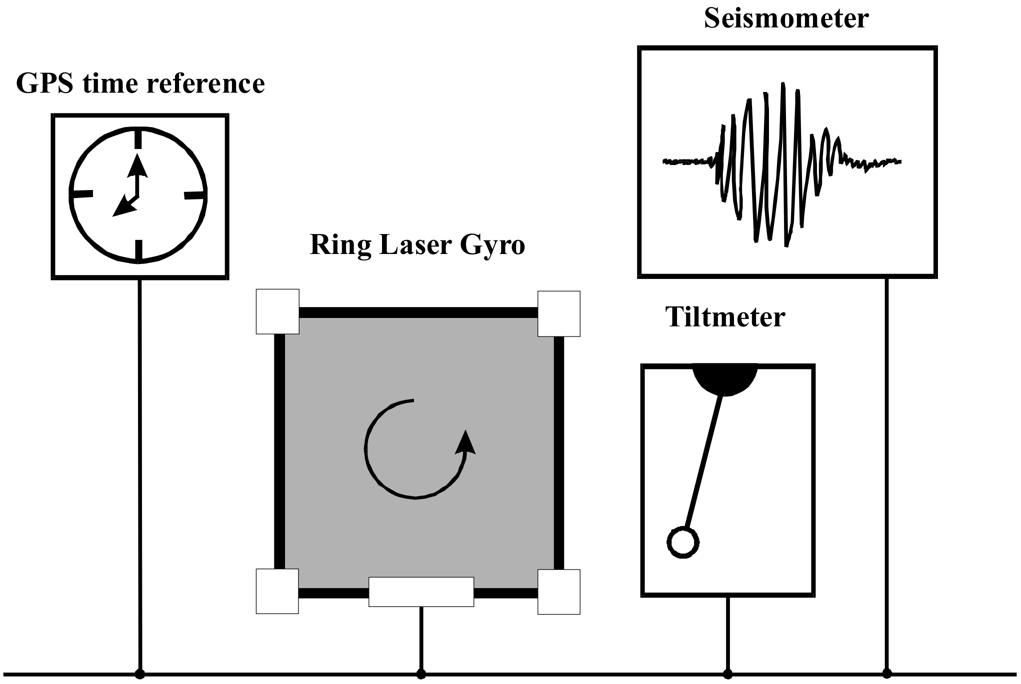

Figure 35: The GEOsensor principal scheme

activity the instrument must be relocatable. Once this hybrid sensor is completed, it can be set up in any suitable observatory, which provides sufficient infrastructure namely a solid monument with as little temperature variations as possible, power and Internet connectivity.

6.1 Ring Laser Component design

The design concept of the ring laser component of GEOsensor is a compromise between high stability and sensitivity of G and small weight, mobility and montage flexibility of G0. Figure 36 illustrates the ring laser design.

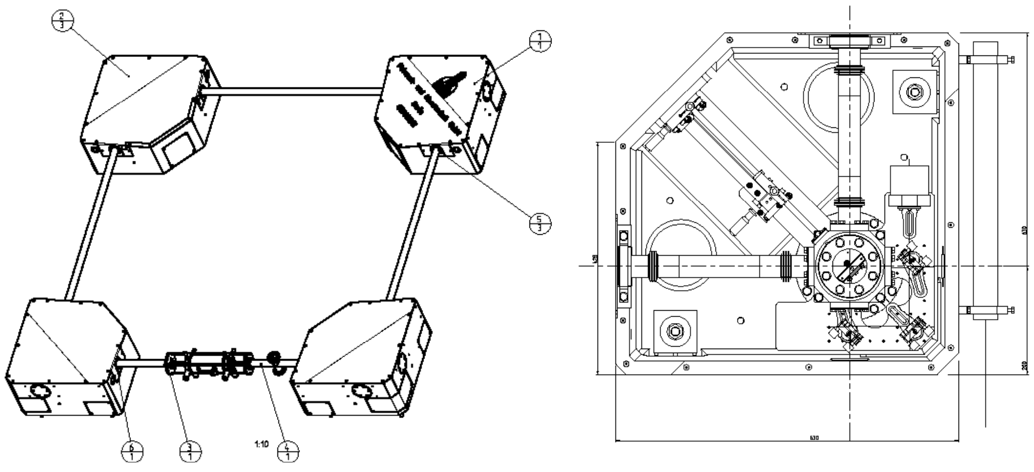

Figure 36: Design of the ring laser component of the GEOsensor. The overall view (left) and corner box(right)

Four 1.6-meter long stainless steel tubes, rigidly attached to the corner boxes, which contain the mirror holders, form the square ring laser contour. The four high-reflectivity supermirrors are creating a closed square beam path. The ring laser has a modular design, i.e. it can be upscaled by using longer tubes while other components remain unchanged. This concept allows the user to adjust the size and accuracy characteristics of the ring laser component according to the conditions and requirements at the site of the instrument deployment.

The gain tube required for the lasing process is located in the middle of one of the tubes, symmetrically with respect to other ring laser parts. The excitation is provided by RF discharge to avoid the biases caused by Langmuir flow like in the DC driven plasma tubes. The corner boxes are made of granit-epoxy compound for better mechanical stability. They must be rigidly mounted onto the concrete basement in a place of the system location. The concrete base acts as the stable geometrical reference for this ring laser. After the box installation the mirror holders can be aligned by a folded lever systems to an accuracy of better than ±15 arcsec per mirror, thus forming the planar beam contour. The pick up system for the interferogram of the ring laser is built inside of one of the corner boxes. Each of the corner boxes has a total weight of 120 kg and is mounted to the monument by 3 steel stubs in the bottom of the encasing.

In the presence of temperature fluctuations the ring laser experiences rapid mode changes due to the cavity deformation. However it is not crucial for GEOsensor application since the quake induced frequency modulations are not critically affected by the mode change. The short-time (about 1 hour) monomode operation is enough to capture the seismic rotation and even if a mode hop occurs in the middle of an earthquake it can be removed from the data at the postprocessing.

The way of the beat frequency extraction is the following. A very small part (approx 0.2 ppm of the beam power) of the two counterpropagating beams is passing through each corner mirror. At one of the corners they are superimposed in a 50%:50% beamsplitter using the reflecting mirror assembly as shown in Figure 37.

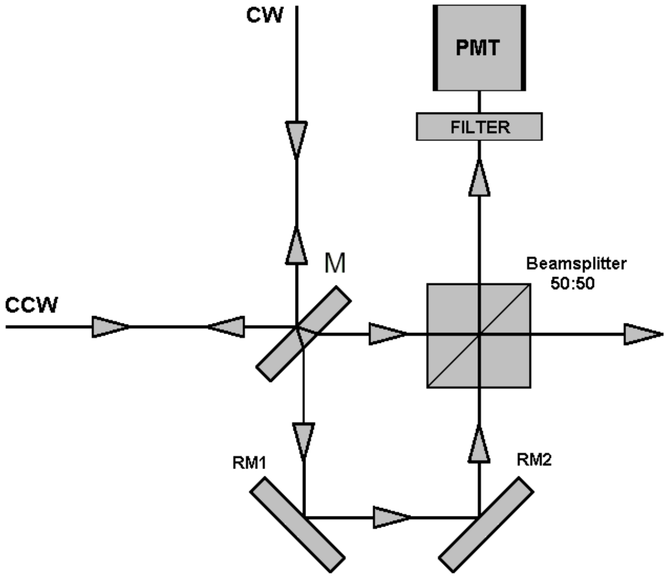

Figure 37: Beam combining scheme: CW –clockwise propagating beam, CCW – counterclockwise propagating beam, M – corner mirror, RM1 & RM2 – reflecting mirrors; PMT - photomultiplier

The resulting combined beam passes through the spectral filter and then the photodetector observes the interference fringes. When the input rotation is nonzero the fringes are moving relative to the photodetector thus changing the brightness of the incoming light. The frequency of this motion is proportional to the input rotation magnitude. Thus in order to obtain the Sagnac frequency one has to count the passing fringes per time unit.

In the GEOsensor this approach is utilized due to the corner box inner space limitations. Here the clockwise beam is passing trough the mirror rightwards, reflecting twice and meet the counterclockwise beam at the beam combiner. The combined beam then goes to the detector. The output signal of the detector is an AC voltage with carrier frequency equal to the beat frequency of the conterrotating beams, i.e. Sagnac frequency according equation (1).

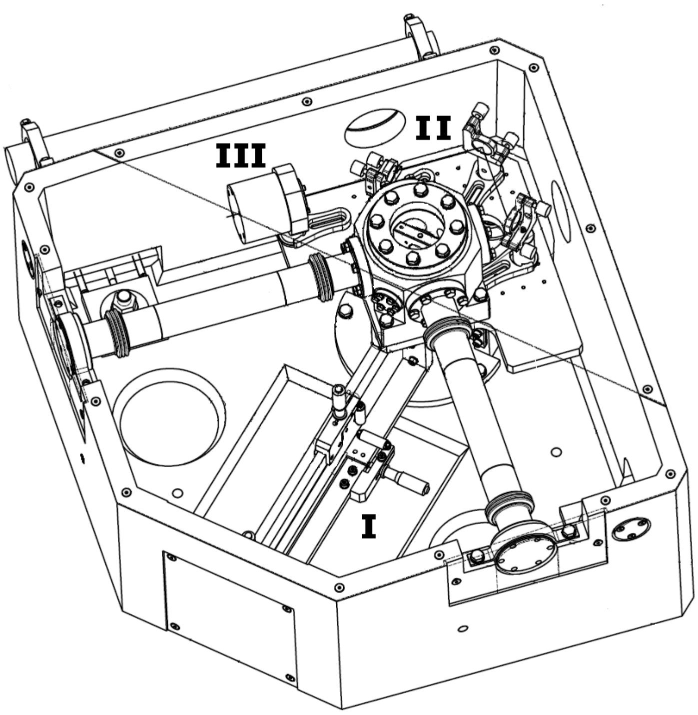

Figure 38: The inside of the corner box: mirror adjustment screws (I), laser beam path (II), photodetector (III)

6.2 Auxiliary sensors

Since ring lasers are inertial rotational sensors they need to be referenced to the location of installation as well as to a standard seismometer collocated with the ring laser. For this purpose we are generating a combined dataset that contains simultaneous observations of the rate of rotation (acceleration) from the ring laser and ground velocities from the seismometer along with tiltmeter measurements. The latter is necessary in order to monitor small changes in tilt of the ring laser plane relative to the local g-vector, because ring laser measurements are sensitive to variations in orientation. While the tilt due to the tidal components (amplitude about 30 nrad) and polar motion (maximal amplitude of about 90 nrad) produce the corresponding changes in the observable rotation rate equal to 2.4×10^{-12} rad/s and 4.3×10^{-12} rad/s respectively, the earthquake induced tilt variations can reach the amplitudes of several tens of microradians with equivalent changes in observable rotation rate of few nanorad/s. All observations must be precisely timestamped since the accurate timing of the signals recorded allows deducing the seismic wave properties. For this purpose a GPS time reference is integrated in the GEOsensor design. It may be important to correlate the observations with measurements of atmospheric pressure and ambient temperature in order to understand and correct the GEOsensor output data. Therefore this information is also recorded along with the rest of the data.

6.3 Data acquisition techniques

The output of the RLG photodiode circuitry is an alternating voltage with the carrier frequency equal to the Sagnac frequency. This frequency has to be determined at short time intervals. It means that the data extraction is indirect unlike in case of seismometer where the output signal is simply scaled ground velocity. There are a few approaches that can be implemented for the Sagnac frequency estimation. Here we discuss them from the point of view of applicability according to the standards accepted in seismology. It is in general 20 Hz sampling rate that covers most of the signal's frequency range of interest and accurate timestamping with the precision down to 1 ms. Figure 39 illustrates the specific of the seismic rotation data acquisition. Here the output signal of the photodetector, i.e. the voltage with Sagnac frequency as a carrier, taken during the Fiji earthquake in 2002 is represented. One can see the strong variations of the signal frequency caused by the quake induced rotation rate changes. The standard for seismic signal acquisition frequency (20 Hz) puts the strict requirement on the duration of the time window within which the rotation rate has to be established. The 20 Hz equivalent time window is 0.05 s, which means that every 50 ms the rotation rate magnitude, or the carrier frequency of the photodoide output signal, must be estimated. The duration of the dataset on Figure 39 is 0.2 seconds, therefore the only four data blocks of above mentioned length fit into this sample. As one can see it became difficult to estimate frequency accurately with such a huge and fast changes of the carrier. For seismic purposes the rotation deriving technique should be capable to obtain those variations without large uncertainties. In the following sections we discuss the available means for frequency estimation.

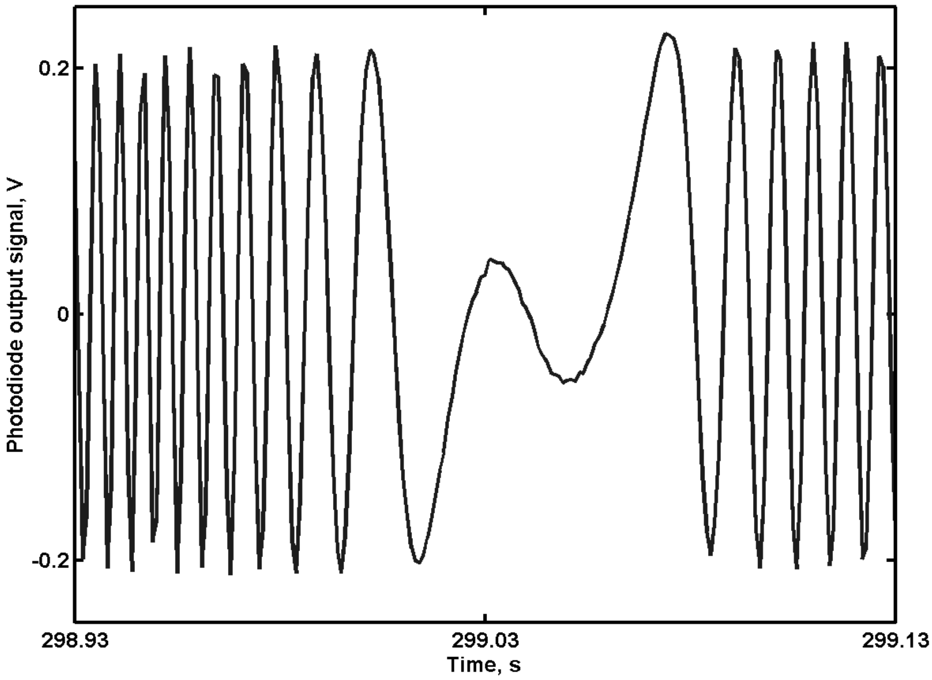

Figure 39: Example of C-II ring laser output during the FIJI quake

6.3.1 Frequency and period counting

The measurement of the frequency in the counter is accomplished by counting the rising edge of the input signal for a precise period of time (gate time). Then in simplest case the frequency of the signal is determined as number of wavelengths divided by gate time. There is always the possibility that up to one wavelength can be missed. For the ring laser like G this implies a frequency estimation error of about 0.3%. However for smaller rings that will be worse. Nevertheless the counter when used in period counting mode can produce better results. In this regime the time interval for a certain number of wavelengths passed trough the counter is determined. Therefore no errors like in the frequency regime occur. The accuracy depends on time resolution and stability. The most precise hardware that has been tested is the Hewlett-Packard HP 5370 Time Interval Counter with time resolution of about 20 ps. Unfortunately no time window settings equivalent to the 20 Hz acquisition rate is available in the counters tested. The temperature induced drift is possible to exclude if the internal quartz oscillator can be bypassed by using an external frequency standard, however the absence of 50 ms (20 Hz acquisition rate) time window and rather slow data transfer protocol makes the counter application difficult.

6.3.2 Autoregressive analysis

King [12] implemented autoregressive second order AR(2) analysis for RLG beat frequency and spectral linewidth estimations. The autoregressive model assumes the signal to be monochromatic in this case, with deviations imposed by white noise. A data set is then modeled as

$$X_t + a_1 X_{t-1} + a_2 X_{t-2} = \vartheta_t \qquad (66)$$

where X_t are the discrete time samples of the data set, the a_i are parameters and ϑ_t is a random process, usually a Gaussian distribution N(0,1) with zero mean and unit variance [16]. The AR(2) model describes a pseudo-sinusoidal signal with Lorenzian lineshape for narrow spectral lines, which is a nature of the beat frequency in ring laser when it is quantum-noise limited. This approach provided an appropriate description of the RLG output while there is only one spectral line present for which bandpass filtering about Sagnac frequency is usually necessary. The AR(2) model has been successfully tested on teleseismic data [16] and the limitations of this method in terms of data sampling intervals were determined. According to that research in order to provide reliable frequency estimates the AR(2) model requires at least 20 cycles, which gives a time interval between data samples of about 0.14 s for the GEOsensor RLG with a beat frequency of 139 Hz. Therefore we cannot employ the AR(2) analysis for a broadband system since the expected useful frequency range is 0.05-10 Hz, which makes the available sampling time interval not larger than 0.05 seconds. The modeling of the AR(2) estimator deviations with different number of cycles per sample has been carried out using the raw G ring laser signal. In addition, the voltage offset influence on the Sagnac frequency determination accuracy was estimated. The results are presented in Figure 40.

This diagram shows that 20 cycles are not enough for AR(2) to provide a stable estimation but at least 200 of those are required for the estimation routine to converge. This requirement becomes even more important in the presence of a photodetector output voltage bias. As one can see such biases produce offsets in the absolute frequency value of about 60 mHz and 210 mHz for 1.5 mV and 3 mV of bias respectively.

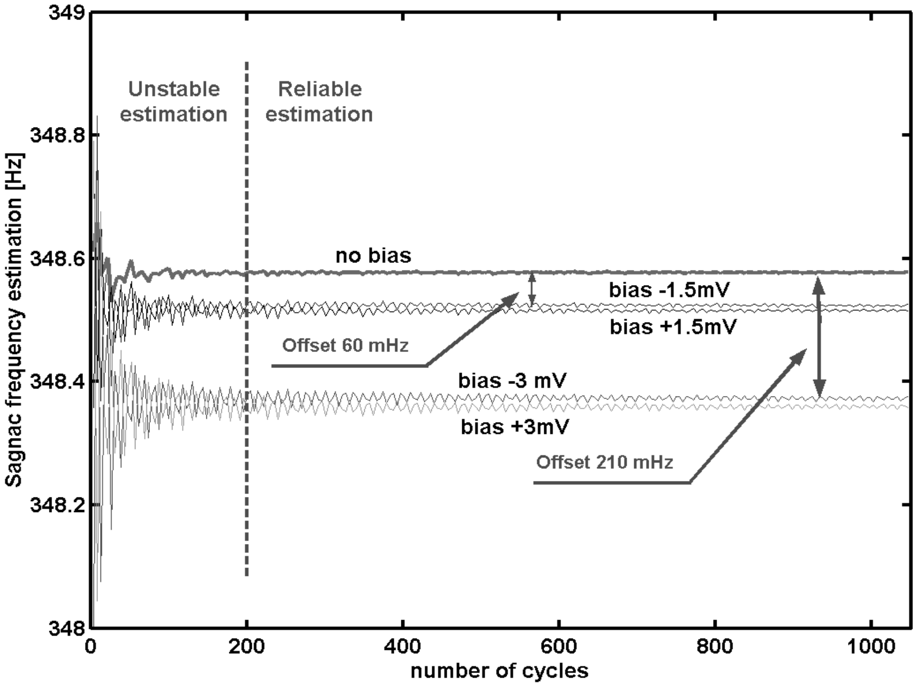

Figure 40: Sagnac frequency estimation by AR(2) for various numbers of cycles and voltage biases

In addition the narrowband filtering of a signal is not allowed for seismic application, and short-time strong input signals cannot be accurately estimated. Nevertheless the AR(2) can still be utilized as an independent secondary frequency estimation approach for teleseismic events.

6.3.3 Frequency demodulation

Both of the above mentioned techniques have one general disadvantage. They have to perform some operations before obtaining the signal of interest. It can lead to a certain time delay, especially in the case of a high acquisition rate. The ideal solution would be an electrical signal proportional to the Sagnac frequency instead of dealing with a frequency modulated carrier. Such a solution has been proposed [26], not ideal though but absolutely suitable for the purpose. Since the signal of interest is composed of the Earth rate bias frequency modulated by the seismic signal, the concept of frequency demodulation can be applied. By phase locking a voltage controlled reference oscillator to the RLG output signal one can obtain the rate of change of the Sagnac frequency as a time varying voltage from the feedback loop of the phase locking circuit. This voltage is then sampled at a rate of 20 Hz. The test unit called FM demodulator (FMD) has been built and compared with other techniques [26]. It is important to note that there is a specific relationship between the detection accuracy and available bandwidth of the signal in the FMD. A wide dynamic range can not have a tight phase locking, therefore for different frequency bands one needs different demodulator settings. A typical FMD amplitude-frequency response is flat from DC up to 5 Hz, then decreases with a slope of about 10 dB per decade. Therefore we need at least two demodulators to cover the whole 10 Hz of the seismic signal frequency band, one with a tight loop for teleseismic events (up to 0.5 Hz) and another with loose coupling for local events (0.5 – 10 Hz).

6.3.4 Comparison of the three methods

For the comparison of the three methods a series of artificial rotation perturbations in the G laboratory were executed. The resting monument of the ring laser was slightly pushed on its corner with varying force and rate. On the low frequency impacts (0.1-1Hz) all three techniques demonstrate a good agreement as illustrated in Figures 41 and 42.

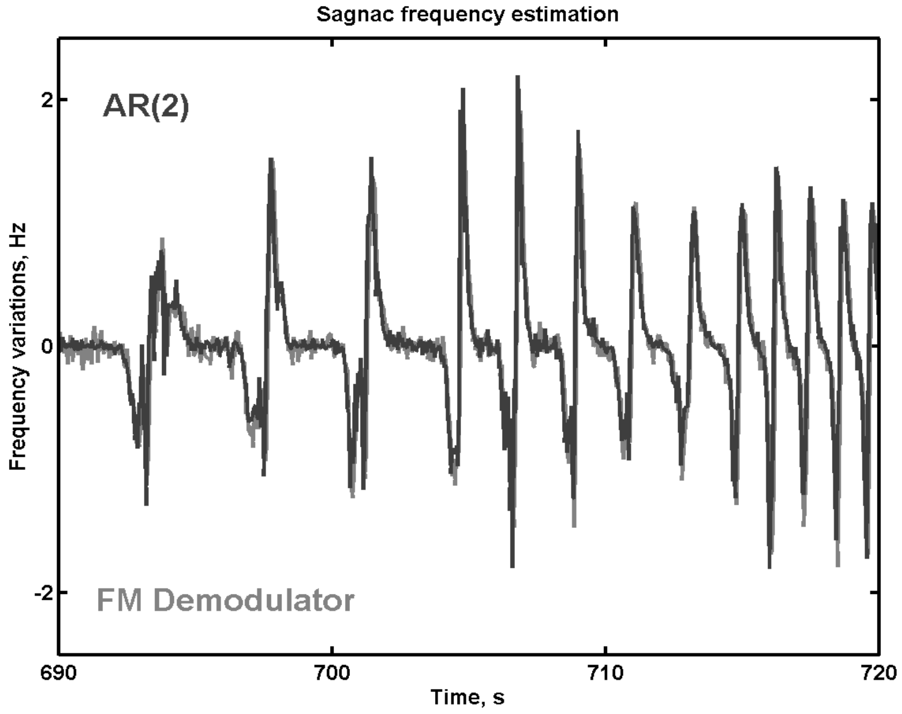

Figure 41: Comparison of AR(2) and FM demodulator beat frequency estimation for low rotational rate changes

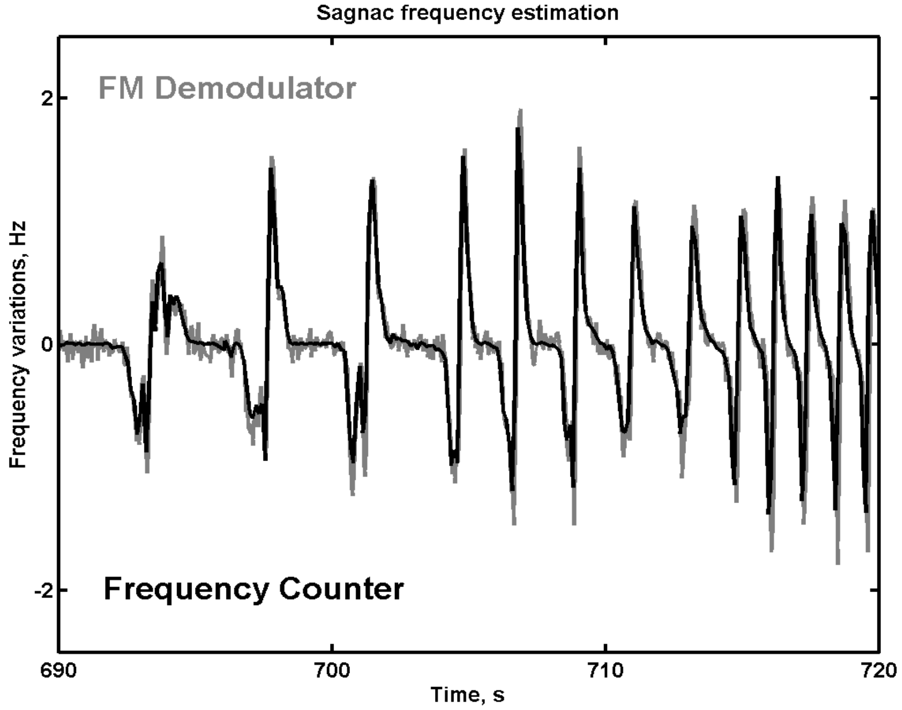

Figure 42: Comparison of frequency counter and FM demodulator beat frequency estimation for low rotational rate changes

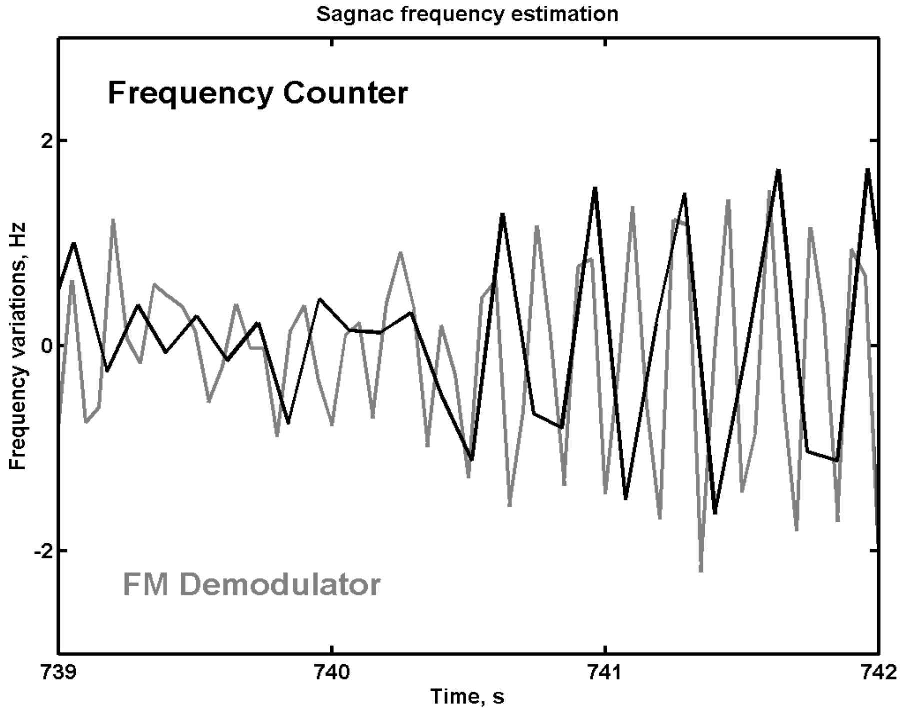

Figure 43: Comparison of frequency counter and FM demodulator beat frequency estimation for high rotational rate changes

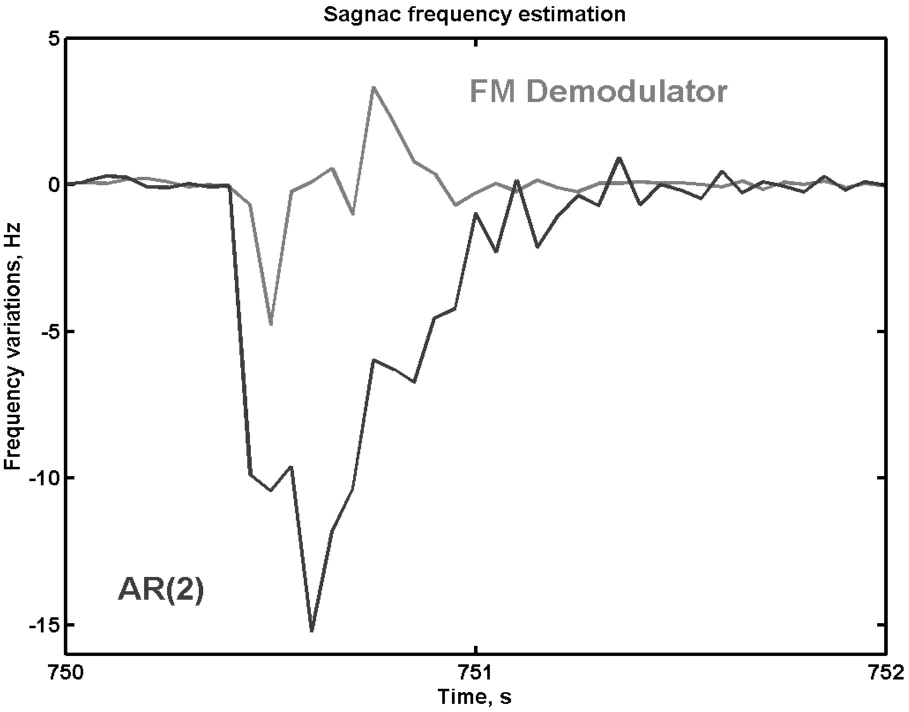

Figure 44: Comparison of AR(2) and FM demodulator beat frequency estimation for high rotational rate changes

A higher noise level in the demodulator data here is due to its wide bandwidth setting. However when the perturbation rate becomes faster the counter failed to estimate the frequency simply because of its time window limitations (Figure 43). AR(2) demonstrates better results but on higher rates than 1 Hz it produces inadequate estimations along with divergence-like responses on strong short-time impacts (Figure 44). The sum of these artifacts along with the simplicity of the phase locked feedback loop usage makes the frequency demodulator a key technology for the GEOsensor. A further comparison of the AR(2) and the FMD results obtained during the real earthquakes confirmed the advantages of the latter technique over the frequency estimation algorithms (see section 7.1.2).

6.4 Data time stamping

The precise time stamping of the data is absolutely crucial in seismology. All the data samples must be equidistant and localized in time with an accuracy of at least 1 ms. Therefore a highly stable time source must be used as an acquisition clock. For this purpose the reference GPS time-frequency station is utilized. The time stamps are provided with a PPS (pulse per second) signal with an accuracy of 30 ns RMS relative to UTC and the data sampling is based on a reference frequency output which has an accuracy of better than 1×10^{-12} (while locked to GPS). The general concept of timing realization totally relies on the use of an external precise time/frequency source. The PPS signal triggers the acquisition, so one knows the dataset start time with PPS precision. In turn, the DAQ internal channel clock is replaced with an accurate external GPS-based frequency. Possible time offsets between the arrival of PPS and the next first reference frequency pulse rising edge can be estimated by using internal hardware counters. However the clock machine in the GPS station is organized in such a way that when it is locked to GPS the frequency signal is synchronized with PPS. The acquisition test at 1 KHz rate shows that there is no detectable time offset between rising edges of the PPS and frequency signal, therefore the required precision of 1 ms is achieved.

6.5 Data file structure

The data acquired is streamed to a disc in a binary format for better logging speed, low hard disc space consumption and high compatibility. In order to make the file format as close to one typically used in seismology as possible, the acquisition start time, date and sampling frequency are written in the file header and the file body contains the rotational seismogram signal, three components of ground motion velocities, two components of tilt, ambient temperature and atmospheric pressure, or other signals needed for further data analysis. Each data file contains also a time column in seconds. A special binary-to-ASCII conversion program provides the flexibility required for the user specified data extraction.

6.6 GEOsensor system architecture

A detailed system block diagram is presented on Figure 45. Here the ring laser servo systems (yellow marked) represent the control loop for keeping the gain level and intensity ratio constant. The obtained Sagnac frequency is posted to a signal divider. The signal divider can be employed for optional channels (blue marked) such like real-time monitoring, direct Sagnac frequency estimation or raw voltage recording. The green marked components are integral parts of the whole system. These are: the GPS time-frequency station providing the time code for the computer clock correction, PPS and frequency signals for precise timestamping of the acquired data; a three-axis seismometer providing three components of the ground velocity; two-axis tiltmeter for monitoring of the ring laser orientation; a FM demodulator for obtaining the rotational seismogram. The frequency divider is required for dividing down the original 10 MHz GPS station output to 1 KHz, which is the acquisition rate. An optional pathlength control system can be employed if necessary and by request the raw photodiode voltage can be recorded for further detailed analysis. The data acquisition, preprocessing, temporary data storage and transfer are realized by a logging program programmed in LabView, which is running on the acquisition computer.

This setup has a disadvantage that the logging program, which is running on the host computer, occupies most of the processor resources and makes the access to the file impossible during the acquisition. The National Instruments Real-Time Technology provides the required flexibility and independence of the acquisition process from all the others and the data are always available for extraction and further analysis. This is the state-of-the-art approach implemented within the seismological community and our current data acquisition concept is made to be in maximum agreement with those requirements.

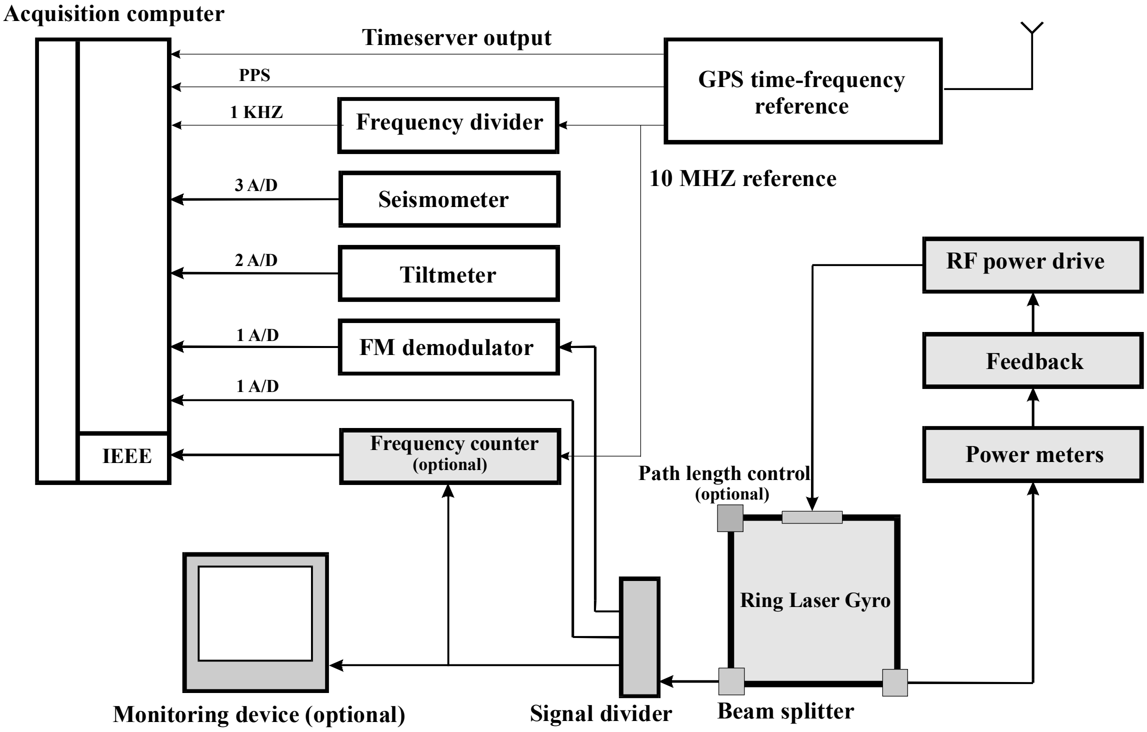

Figure 45: The GEOsensor data flowchart

The acquisition computer is a specifically designed system consisting of the PXI-1002 chassis, NI 8171 controller and PXI-6031 DAQ board. The controller provides the external communication via different interfaces and inner data flow/storage. The DAQ board is sampling continuously the analog channels using the external acquisition frequency source. The acquisition program starts automatically after the controller boot-up. The build-in FTP server provides the access to the data stored on the local hard drive.

6.7 System installation

The place of the GEOsensor deployment should provide a relative stable (concrete or bedrock) basement for the ring laser component. The corner boxes are mounted to the monument by 3 steel stubs in the bottom of the encasing and are then adjusted in such a way that the separation between the mirror holders of two diagonal opposite boxes is equal to within 1-2 mm of the square form of the whole contour. Furthermore each side must have the same length to within 1 mm and the tops of the four mirror holders need to be at the same level. After tightening the screws, the stainless tubes are fixed to the boxes thus forming the laser beam path enclosing. The section containing the plasma tube has a pair of additional supports for better stability.

After that the mirrors must be installed. The mirrors are fixed inside the mirror holder assembly particularly designed for portable systems like the GEOsensor. Once installed into this assembly they do not have to be moved anymore because they are prealigned. These mirror holders can be placed and fixed inside the mirror holder chambers for operation as well as inside the transport boxes for relocation. In order to keep the mirrors ultimately clean for reduced backscatter, the mounting process must be carried out quickly. The next step after the mirror installation is the mirror adjustment. For this purpose an external green CW HeNe laser is fixed on one of the boxes external sidewalls. The optical plate on the same wall is holding two reflecting mirrors and by adjusting the mirrors angles (45° relative to the incoming beam) the beam of the external laser is directed into the cavity through one of the windows in the ring laser mirror holder assembly, following the center axis of the cavity as closely as possible.

Then the orientation of each mirror holder is leveled using the adjustment screws. Each mirror must be oriented in such a way that the incident beam reflected by this mirror hits the next mirror in the center until the laser beam passes through all the four mirrors thus forming a square contour.

Finally the reflecting mirrors, beam combiner and the detector can be installed. Two reflecting mirrors, installed on the inside of one of the corner boxes on an optical plate (see Figure 37), direct the clockwise beam leaking through the corner mirror to the beam combiner (see Figure 38), where it is mixed with the counterclockwise beam, thus producing an interference fringe pattern (see Figure 37). The combined beam is then fed to the photodetector.

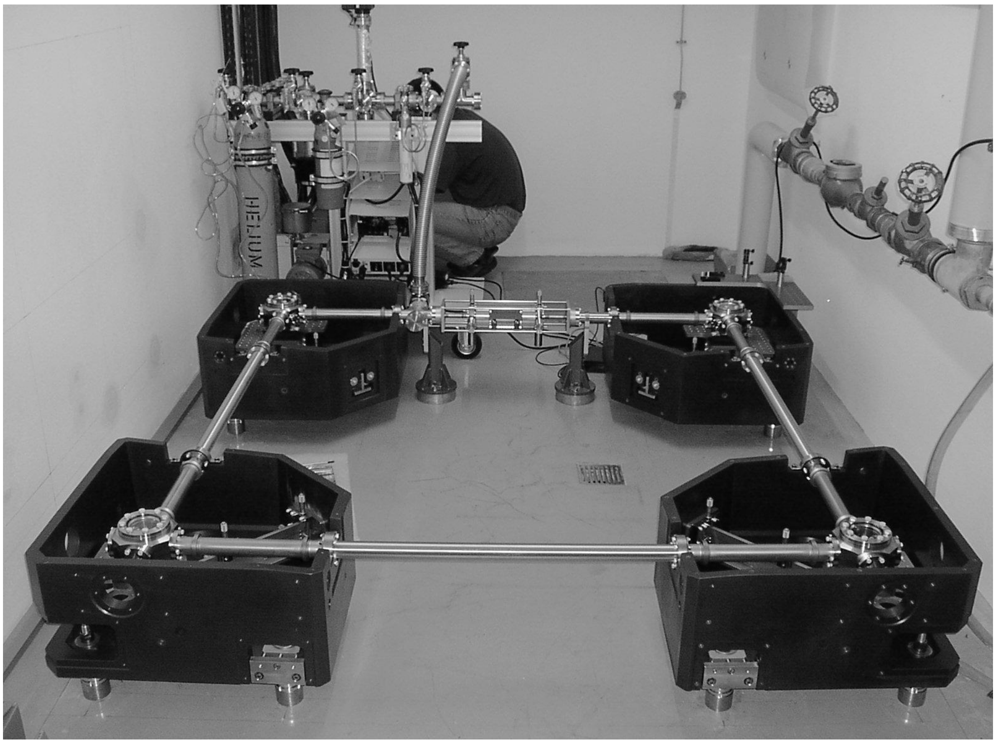

Figure 46: The installation of GEOsensor ring laser component at the Wettzell station

In the next step the pumping system must be connected to the cavity via a vacuum pipe, and after being evacuated (pressure about 10^{-6} bar) the cavity is filled with a mixture of

He and Ne_{20} and Ne_{22} isotopes, the latter two in the ratio 1:1. The RF power supply is connected to the plasma tube electrodes via impedance transformer to match the output impedance of power driver and the plasma capillary.

The seismometer and tiltmeter can be placed next to the ring laser on the same concrete platform according to their installation manuals. The output signals from all the instruments are connected via cables to the data acquisition circuit incorporating the power supplies for the seismometer and the tiltmeter, signal distribution and conditioning boards and the signal termination board.

The latter is connected to the DAQ board of the computer, which provides the data acquisition, storage and communication.

After all the required gas, power and data transmission connection are done, the ring laser component of GEOsensor is ready for operation.

Figure 46 shows the first installation of the GEOsensor ring laser component on the geodetic observatory Wettzell, Germany.

7. Results and Discussion

During the last two years when the GEOsensor was under construction, quite a number of seismic events have been recorded by the large ring laser gyroscopes. The parameters of the most significant earthquakes are summarized in Table 8, where **D** is the distance between the earthquake epicenter and the G ring, **M** is the magnitude of the earthquake and **K** is the heading angle in degrees, time - UTC. For all these events the translational data have been taken from the broadband STS-2 seismometer, permanently located at the Fundamentalstation Wettzell. Rotational seismograms are taken from the G ring laser gyroscope.

Table 8: Parameters of the detected earthquakes

Location	Date & Time	M	Depth, km	D, km	K
Northern Algeria 36.9N 3.71E	21.05.2003 18:44:19	6,8	10	1550	212°
Greece 39.19N 20.24E	14.08.2003 05:14:55	6.3	10	1272	147°
Hokkaido 41.78N 143.86E	25.09.2003 19:50:06	8,3	27	8838	35°
Russia-Xinjiang 50N 87.85E	27.09.2003 11:33:24	7,3	16	5175	59°
Southwestern Siberia 50.22N 87.68E	01.10.2003 01:03:25	6,7	10	5153	58°
Rat Islands 51.13N 178.74E	17.11.2003 06:43:07	7.8	33	8794	9°
Papua, Indonesia 3.94S 134.99E	07.02.2004 02:42:35	7.3	10	12636	67°
Nancray, France 47.35N 6.29E	23.02.2004 17:31:21	5.1	10	527	250°

Morocco 35.14N 3.99W	24.02.2004 02.27.46	6.4	0	2070	228°
Eastern Honshu, Japan 33.66N 137.07E	5.09.2004 14:57:18	7.4	10	9295	43°

The rotational component of seismic events in order to be captured by the ring laser, deployed in Wettzell, must fulfill certain conditions, which are a combination of a distance, magnitude and depth of the quake. Most of the earthquakes recorded have their focus no deeper than 30-40 km, which is responsible for the strength of the propagating surface waves, and in other words, the seismic rotation. If the focus of the earthquake is deeper than that the seismic energy can dissipate on its way to the surface and no significant amount of S-waves will be produced. The closer the earthquake is to the RLG location, the more high-frequency components are present in the rotational seismogram.

7.1 Results from the G-ring

Here we discuss a few different earthquakes, among them the 2003 Hokkaido event, the strongest earthquake of that year. Those examples demonstrate the differences between the seismic rotation properties for different earthquakes and the capabilities of various techniques under real operational conditions. The difference between these events, leading to quite distinguishable effects produced, illustrates the abilities of ring lasers and the implemented acquisition technologies.

The first test of the FMD, installed on the G ring laser, on the real earthquake was the detection of the Vogesen (Vosges) earthquake at 22.02.2003 with magnitude of 5.4. Figure 47 shows corresponding rotational seismogram.

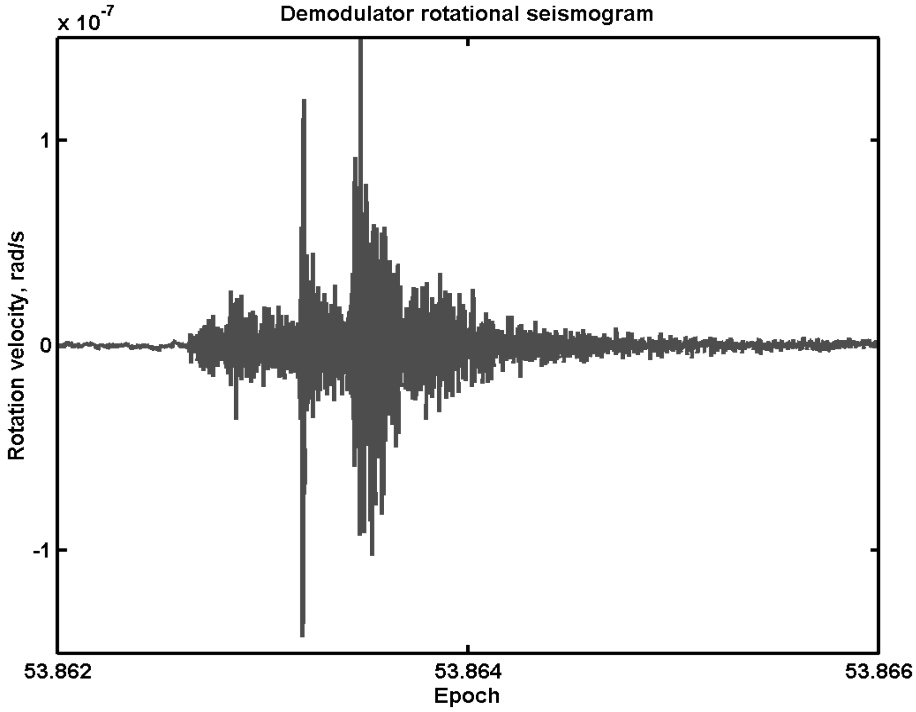

Figure 47: Vosges Earthquake rotational seismogram obtained with the FM demodulator

This is not an teleseismic event since the distance between the earthquake epicenter and the location of the ring laser is about 400 km. One can see a rather strong rotation, with amplitude of up to 1.5×10^{-7} rad/s. A local event like this produces body waves causing signal responses with a wide spectrum of up to 5 Hz, as one can see in Figure 48.

Another example of an earthquake detection by the FM demodulator is the 25.09.2003 Hokkaido event with a magnitude of 8. The rotational seismograms have been obtained by the G ring laser with the FM demodulator and a frequency counter. Figure 48 shows the first stage of the teleseismic rotational signal propagation. One can see a very good agreement between both instruments in amplitude as well as in phase. This time the teleseismic event was detected, with much smaller amplitudes and a much narrower frequency band than the local event.

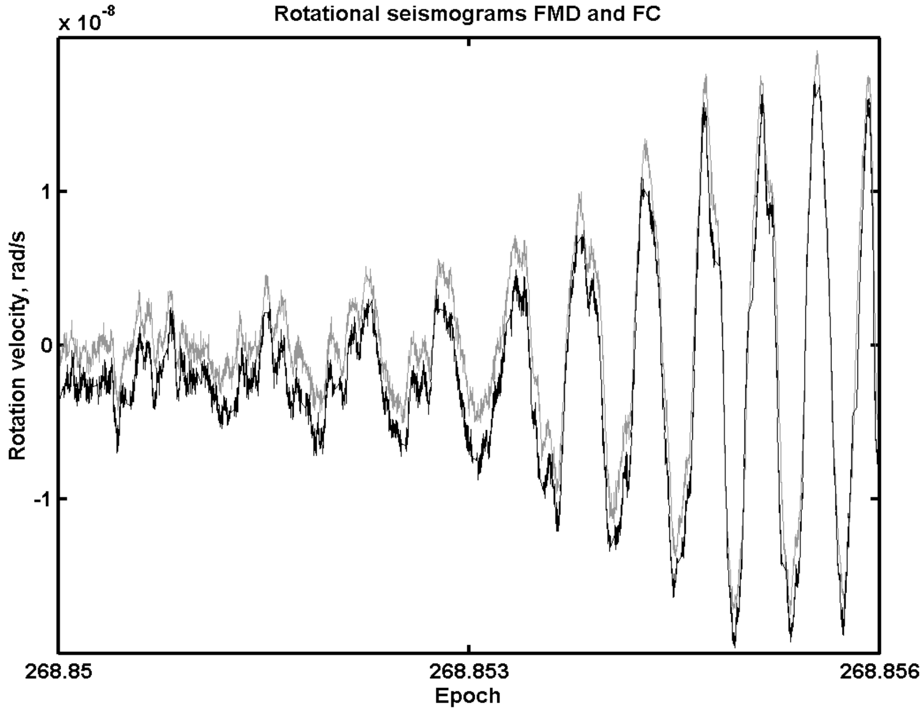

Figure 48: Hokkaido Earthquake rotational seismogram obtained with the FM demodulator (black curve) and frequency counter (grey curve)

In this case even the frequency counter is reasonably precise. This is because a teleseismic event produces a narrow frequency response, mostly due to the surface waves. The surface waves have a much more narrow range of frequencies than the body waves, and most of the signal power is concentrated around the 0.05 Hz, which is illustrated by the Figure 49.

The spectral components of the moderately distant quake spread up to 4 Hz being strongest between 0.5 and 2.5 Hz (Figure 50). In case of far away earthquake the spectral response area is between 0 and 0.15 Hz. The knowledge of the possible quake locations distribution is important for proper demodulator bandwidth adjustment.

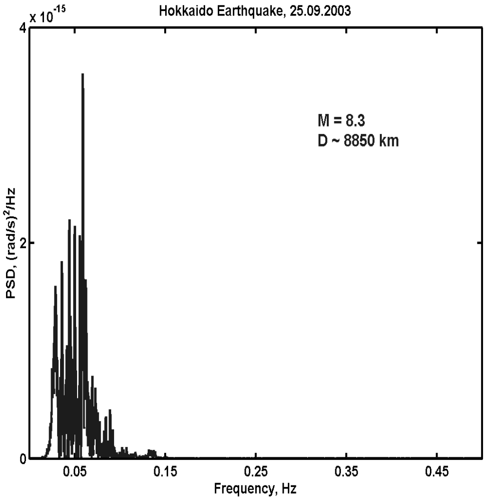

Figure 49: Hokkaido Earthquake spectrum

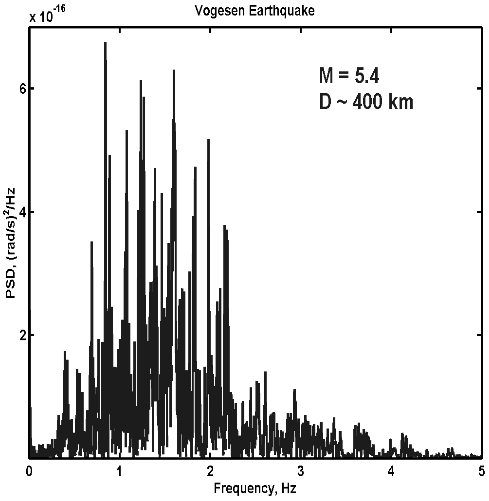

Figure 50: Vosges Earthquake spectrum

7.1.1 The Hokkaido region earthquake

The 26.09.2003 Hokkaido earthquake has an origin time of 19h 50m 06s UTC. This propagating seismic wave field has been recorded by both the STS-2 broadband seismometer and the G ring laser in Wettzell. The translational motion was recorded with 20 Hz sampling rate, rotation rate with 5 Hz. In order to compare the two signals one has to perform the translation motion reformation (see section 5.2). The obtained transverse acceleration, scaled with twice the wave phase velocity (5 km/s) is then compared with the direct observation of the vertical component of the rotation rate. The results are presented on Figures 51-54.

The P-S wave arrival at 20h 12m 20s (Figure 51) and surface wave at 20h 24m 20s (Figure 52) are clearly seen on both seismograms. The rotation rate is in phase with transverse acceleration as expected. However there are differences in the waveforms, especially near the end of the event. These discrepancies are rather sporadically and cannot be compensated by simple adjustment of the back azimuth angle or the wave amplitude (see Figures 53 and 54). The tilt effects are negligible in that part of the seismogram. Therefore this difference has to be attributed to the properties of the seismic waves. The surface waves are dispersive and do not have a fixed velocity, hence some amplitude ratio variations can be explained by this fact. The propagation direction of the wave may vary as well, but it seems not taking any visible effect on the rotation/acceleration correlation.

Most of the discrepancies between the rotation rate and the transverse acceleration can be seen at the last part of the earthquake response (Figures 53-54), where the most significant amplitudes are decaying and perhaps the interference of the smaller waves produces such a disagreement. This is a very interesting area of the signal interpretation and these discrepancies are the subject for further investigations.

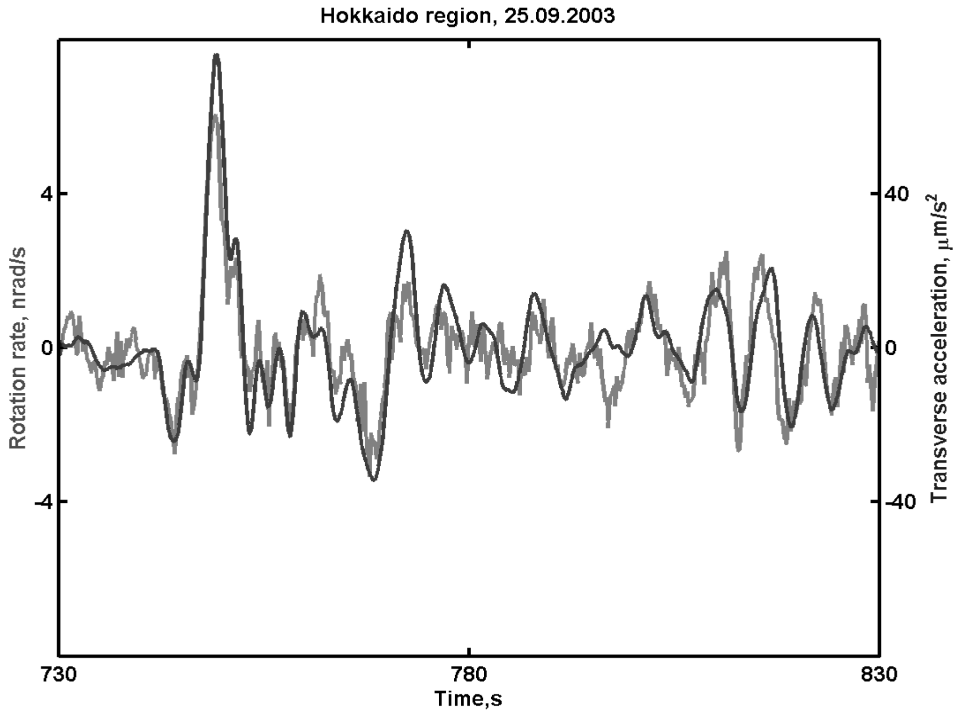

Figure 51: The rotation rate (grey) and transverse acceleration (black) during the Hokkaido earthquake. The arrival of the P-S wave

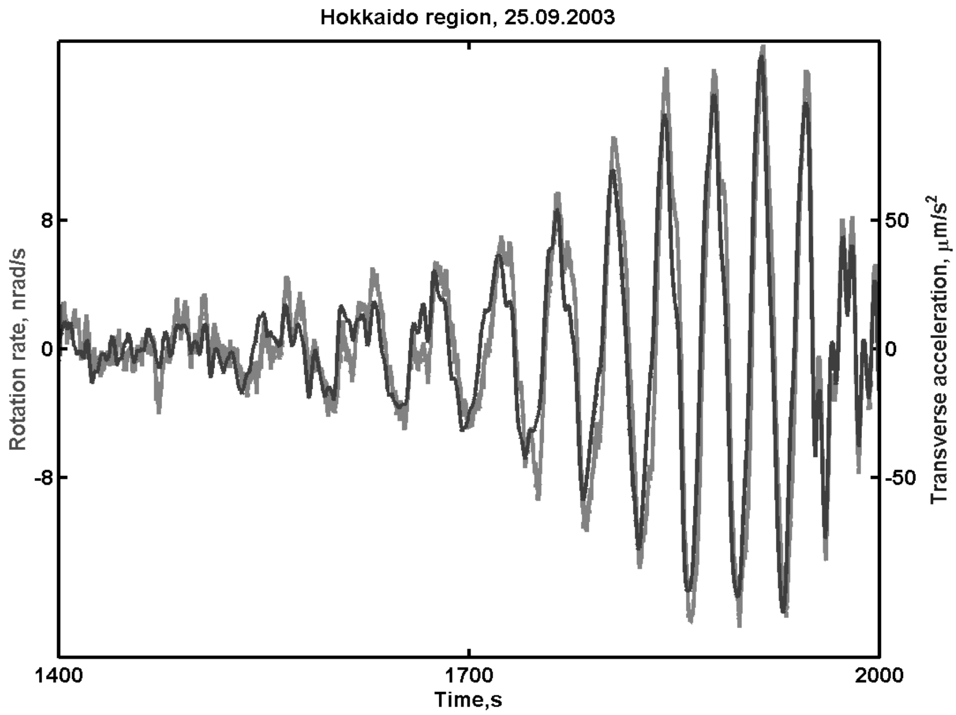

Figure 52: The rotation rate (grey) and transverse acceleration (black) during the Hokkaido earthquake. The arrival of the surface wave

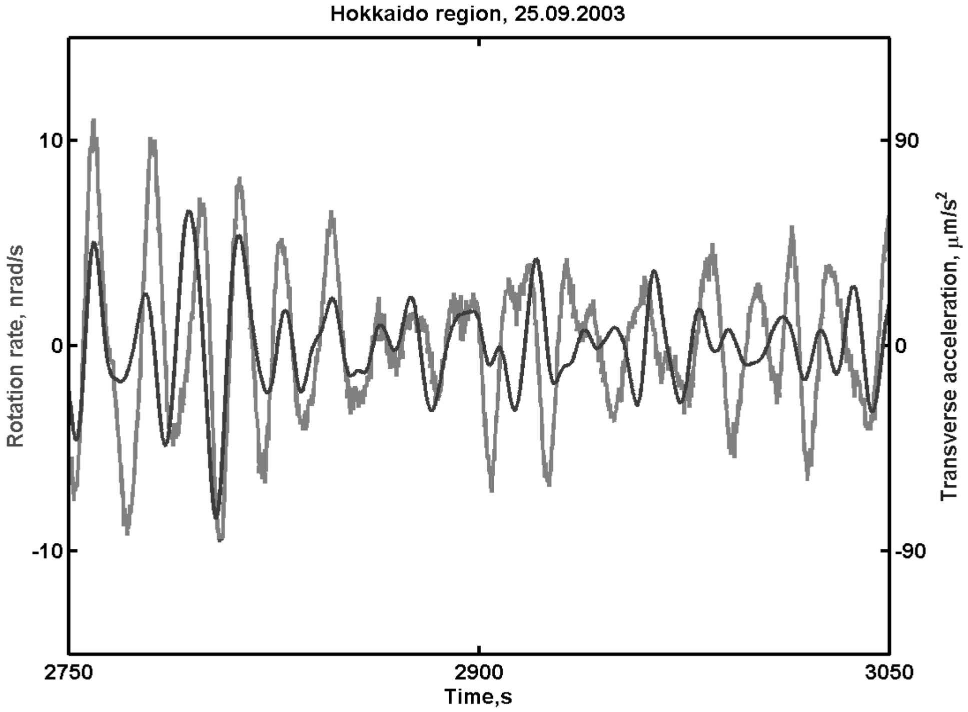

Figure 53: The rotation rate (grey) and transverse acceleration (black) during the Hokkaido earthquake. The maximum amplitudes can be seen here as well as some discrepancies

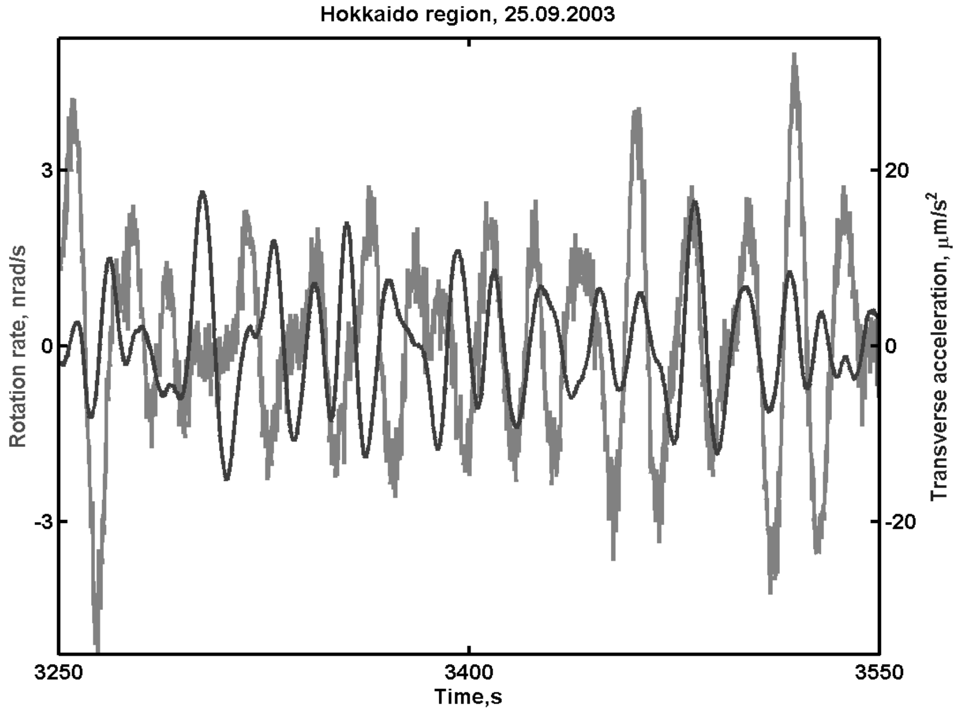

Figure 54: The rotation rate (grey) and transverse acceleration (black) during the Hokkaido earthquake. The last part of the dataset shows some disagreement in both phase and amplitude

Figure 55 shows both waveforms during the earthquake, the cross-correlation and the distribution of the wave velocity. One can see the very large (about 11 km/h) S-wave speed and later on typical 5 km/h Love wave velocity magnitudes, all in a good agreement with expectations. To estimate the wave velocity a 30 seconds long window slides over the

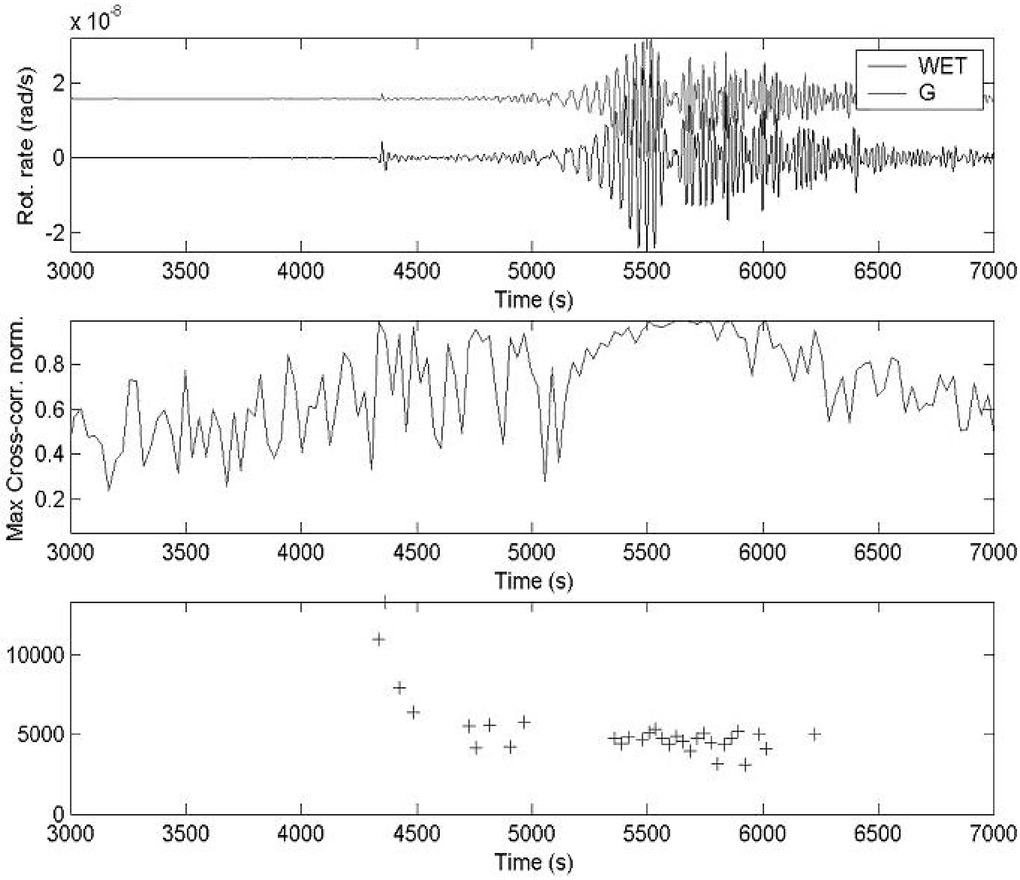

Figure 55: Comparison of rotation rate and transverse acceleration for Hokkaido event

timeseries and searches for the best amplitude fit for the windows with a phase correlation of better than 0.95. The observed velocities are in excellent agreement with expected theoretical values.

In order to check the consistency of the observed amplitudes of rotation a theoretical, or synthetic seismogram has been calculated for this event. Synthetic seismograms are computed by evaluating a mathematical model with a particular geometry of the source and velocity layering that approximates an elastic or inelastic Earth. Solutions of varying approximations to the wave equation in the geometry of the model result in a theoretical amplitude versus time of arrival times or wavefield seismograms. These may be used for studying wave propagation through various media, calculating amplitude and waveform responses to various sources in different models. Furthermore they can be used for the comparison of observed seismograms to various source models. The details of the model used for the calculation of the Hokkaido synthetic seismogram can be found in [7]. The comparison of the calculated and observed rotation and the wave velocity estimations are shown on Figure 56.

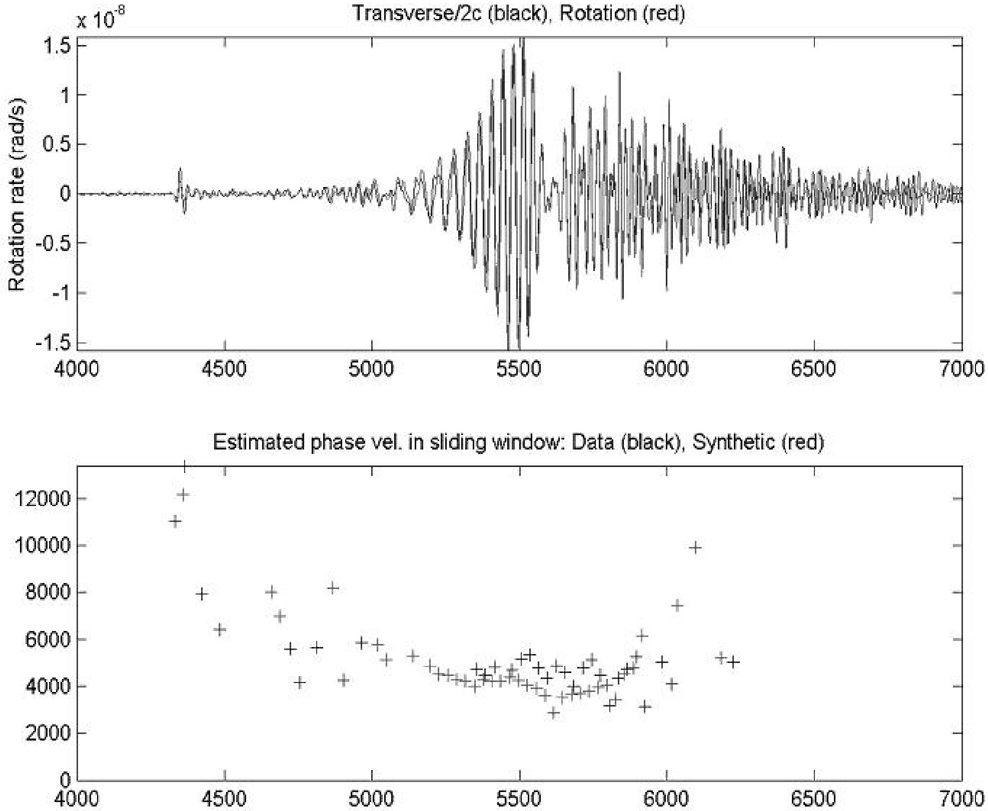
Transverse/2c (black), Rotation (red)

Estimated phase vel. in sliding window: Data (black), Synthetic (red)

Figure 56: Comparison of a synthetic and the observed rotational seismograms for the Hokkaido event

The synthetic seismograms computed for this earthquake show very good agreement with the observations, with similar discrepancies relative to the transverse acceleration data. Therefore the measurements of the rotational motion for teleseismic events are at least consistent with observations of translational motion at the point of the instrument deployment [8].

7.1.2 Bischofshofen earthquake

The 29.06.2004 earthquake in Bischofshofen, Tennengebirge, with magnitude 3.9 and distance of about 185 km, is the nearest quake detected by the G ring laser so far. This is a typical example of an local event, with sufficient magnitude to produce a rotational seismical signal component. The local events are characterized by a wide signal spectrum with frequencies of up to 10 Hz and possibly higher. Therefore any frequency estimation approaches involving filtering are not practical. Figure 57 shows the FMD and AR(2) rotational seismograms for the earthquake. The time delay of the AR(2) estimation relative to the FMD is about 120 ms and is compensated here for comparison purposes. Due to the bandpass filtering of the raw photodiode signal, which is a requirement for the AR(2) procedure, most of the high frequency components in the AR(2) analysis are gone and the restoration of the actual waveform is impossible. While for teleseismic events the AR(2) is still producing reliable estimations the local events cannot be treated accurately with this approach. This outlines the importance of a suitable detection scheme.

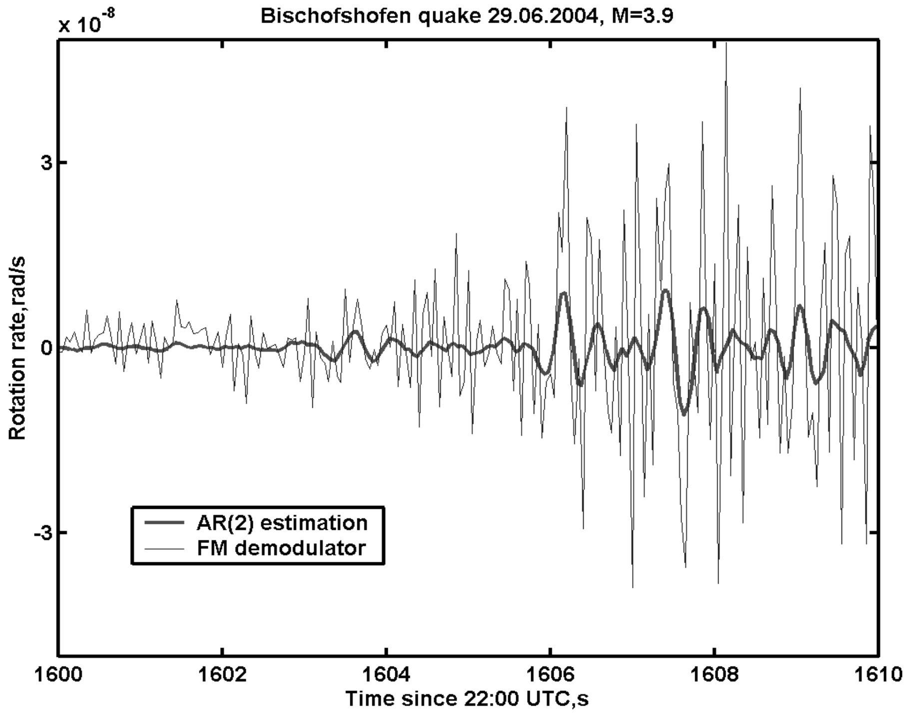

Figure 57: Comparison of rotational seismograms obtained by the FMD and the AR(2) for the Bischofshofen earthquake

The signal of the demodulator also requires a tuning and has a flat amplitude-frequency response within a bandwidth of 5 Hz (see section 6.3.3). However it may be important to complement the data logging with a second more loosely coupled unit of a flat frequency response between 5 and 10 Hz, thus covering the whole 10 Hz frequency window. The application of two independently tuned demodulators can help to keep the logging within range even for strong earthquakes.

7.2 GEOsensor results discussion

During the test phase the GEOsensor system was located in a small room of the office building at the Fundamentalstation Wettzell. The basement of that building is of course far from the required in terms of stability. Apart from the mechanically unstable building structure, the measurements are also affected by various “human” and machinery noises. Large variations of temperature (subdegree level) lead to frequent mode hops in the ring laser, typically in half an hour intervals. Nevertheless that short time period of single mode operation is not critical for the purpose, and the earthquakes can be accurately registered even under these unfriendly environmental conditions. Here we demonstrate the first real earthquake detected by the GEOsensor. The earthquake happened on 16.05.2004 at 9:53 UTC in Poland, magnitude 4.9 25 km deep. Due to the short distance between the source and receiver this earthquake has a lot of higher frequency components in comparison with typical teleseismic responses. Figure 58 shows the rotation rate taken from GEOsensor AR(2) estimation routine, the FMD and the frequency counter data from G ring laser and provided for comparison purposes.
The AR(2) frequency estimation algorithm is still capable to establish the seismic frequencies, however with a severe degradation of amplitude and the introduction of a time delay due to the filtering. The frequency counter data shown here are not worth to analyse (since the sample rate is 5 Hz, therefore the bandwidth is much less than required for such an event) but demonstrate the reliability of the GEOsensor

measurements, despite of the very seismically noisy environment the latter is installed in. The timeshift between the G and GEOsensor datasets is due to the free running timing in the counter.

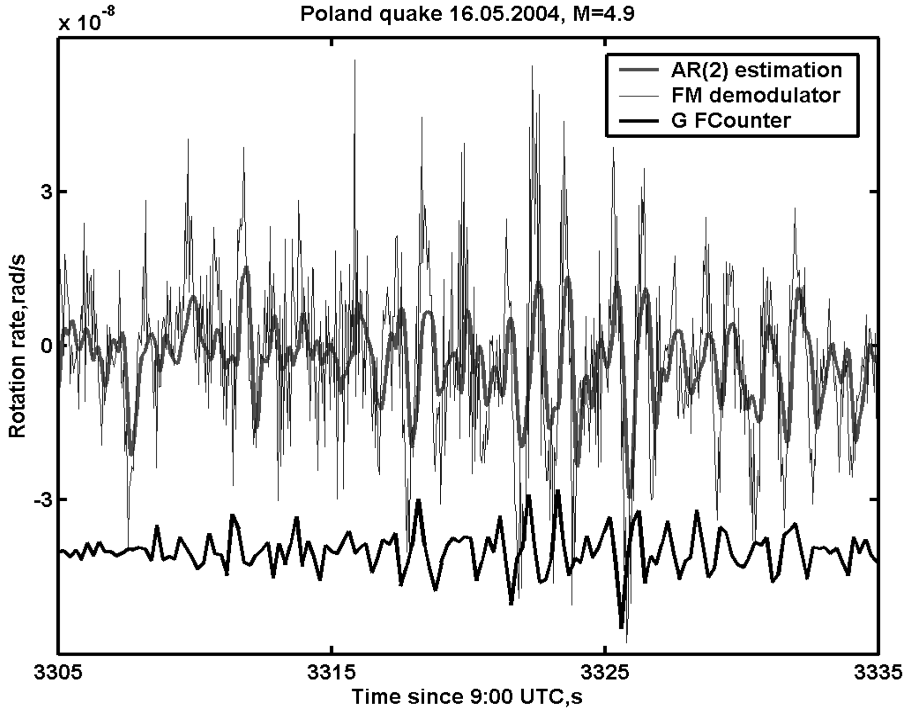

Figure 58: Comparison of rotational seismograms for GEOsensor and G

As in the case of the G ring laser, the AR(2) estimation is not applicable for the detection of local events as can be seen from the picture above. The major part of the signal is damped out by the filter procedure. Figure 59 compares the spectrum of the rotation rate obtained by the FMD and the AR(2) respectively.

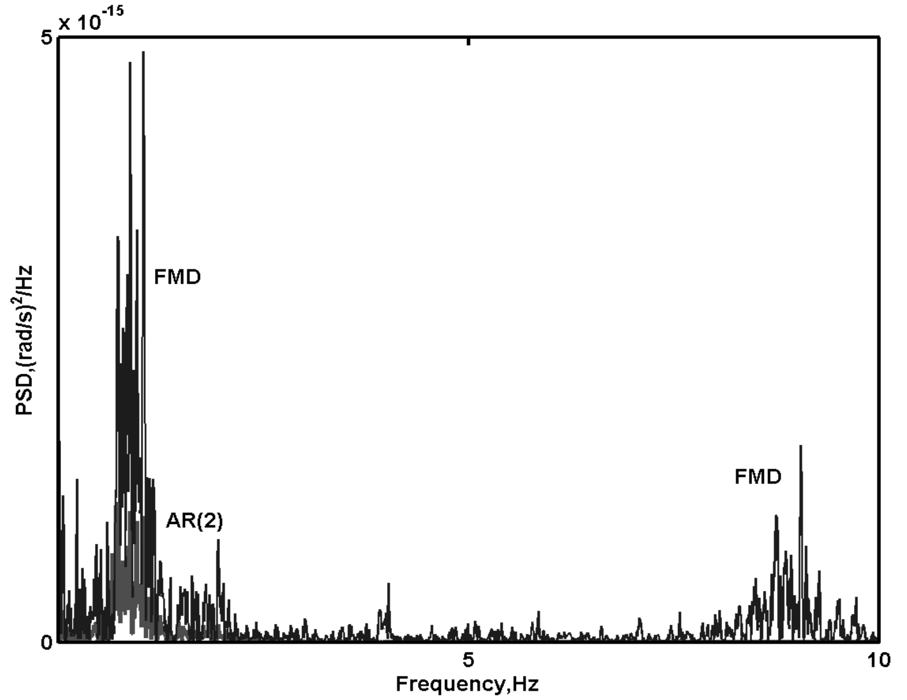

Figure 59: Spectrum comparison of AR(2) and FMD for local class of seismic event

One can see that with the bandpass filtering (bandwidth of 4 Hz) applied to the raw photomultiplier signal a substantial part of the seismically induced signal is suppressed and the amplitude response is distorted. In other words the bandwidth of the AR(2) output is vastly reduced in comparison with the FMD and the signal amplitudes appear also much attenuated. A comparision is shown in Figure 59. The situation is similar to that of the G ring detected earthquake in the previous chapter. Since the GEOsensor will be deployed within an area of high seismic activity the AR(2) estimations can only be taken as secondary for the local seismic events. The demodulators can be adjusted for the operation with a linear amplitude-frequency characteristic within 0-5 Hz and 5-10 Hz frequency domains in order to capture both local and teleseismic events without distortions.

Another interesting example of the earthquake detection by both G and the GEOsensor ring lasers is the Eastern Honshu, Japan event at 5.09.2004. The G records presented by both FMD and counter readings while for the GEOsensor only AR(2) was available at that time. The interesting part about that record is that during the earthquake the GEOsensor ring laser experienced one of the mode hops, which occur quite frequently due to the temperature instability in the room. The timeseries is shown in Figure 60.

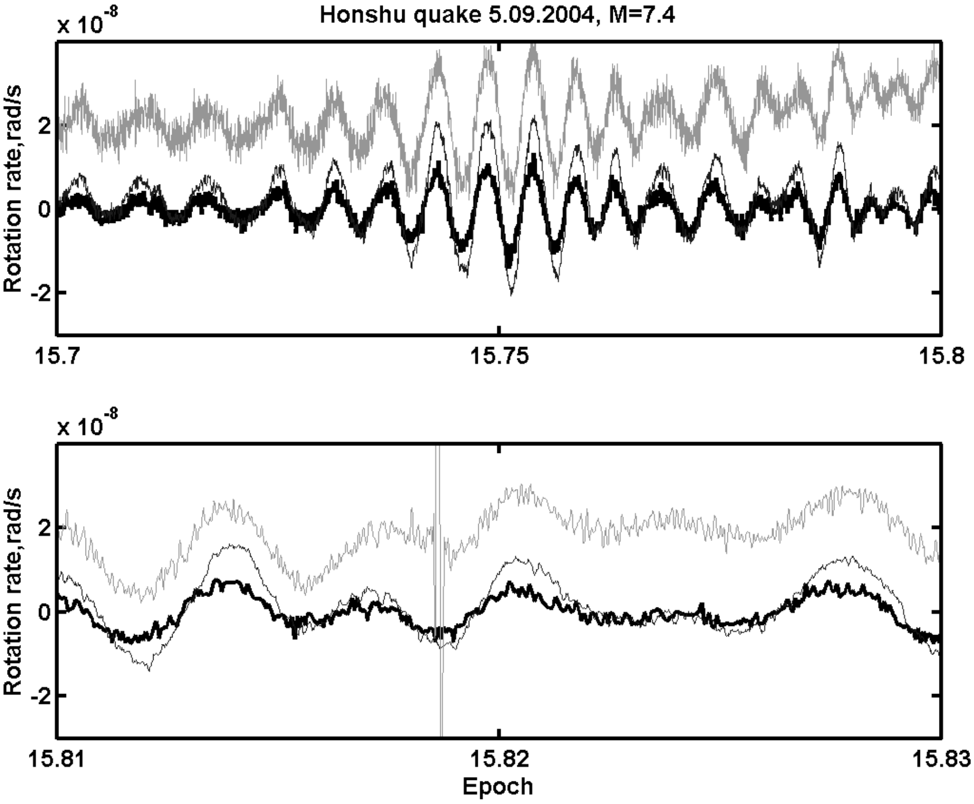

Figure 60: Comparison of rotational seismograms for GEOsensor (AR(2) - grey) and G (FMD –thin black curve, Frequency Counter – thick black curve); offset added for better viewing

On the top graph one can see the typical surface wave arrival (rotation rate in rad/s) and all three recording techniques (of both ring lasers) demonstrate a very good agreement both in phase and amplitude. The larger noise level of the GEOsensor signal is due to the noisier environmental conditions. The small differences between the amplitudes of the rotation rate obtained by the FMD (G ring laser) and the AR(2) (GEOsensor) can be attributed to the smoothing of the signal response due to the bandpass filtering in the AR(2) while the FMD possesses a flat amplitude response up to 5 Hz, which is plenty for the recording of an undisturbed rotation.

The bottom graph shows the laser mode change in the GEOsensor that occurred during the earthquake. One can see that the perturbation of the signal due to the mode change is very short (1 second) and does not ruin the whole record, as it has been feared. Moreover, the timeseries short-term drift due to the large temperature fluctuations can be corrected in order to obtain the unbiased rotation signal as it was done on the data set on Figure 60. This is because the earthquake and the temperature induced drift happen each in a frequency band, which is totally unrelated with respect to each other. The important conclusion is that we can correct the mode jump induced signal disturbances without degrading the quality of the timeseries. If the deployment site provides stable environmental conditions (like those in the G laboratory or similar) we can expect no rapid mode changes or substantial drift, which will improve the sensor performance even further.

The especially build facility at the Pinion Flat observatory, South California, provides the required rigidness and stability of basement as well as smooth environmental conditions. It is a “bunker” like underground laboratory designed similarly to that one in Wettzell. The sketch of the Pinion Flat facility is shown on Figure 61.

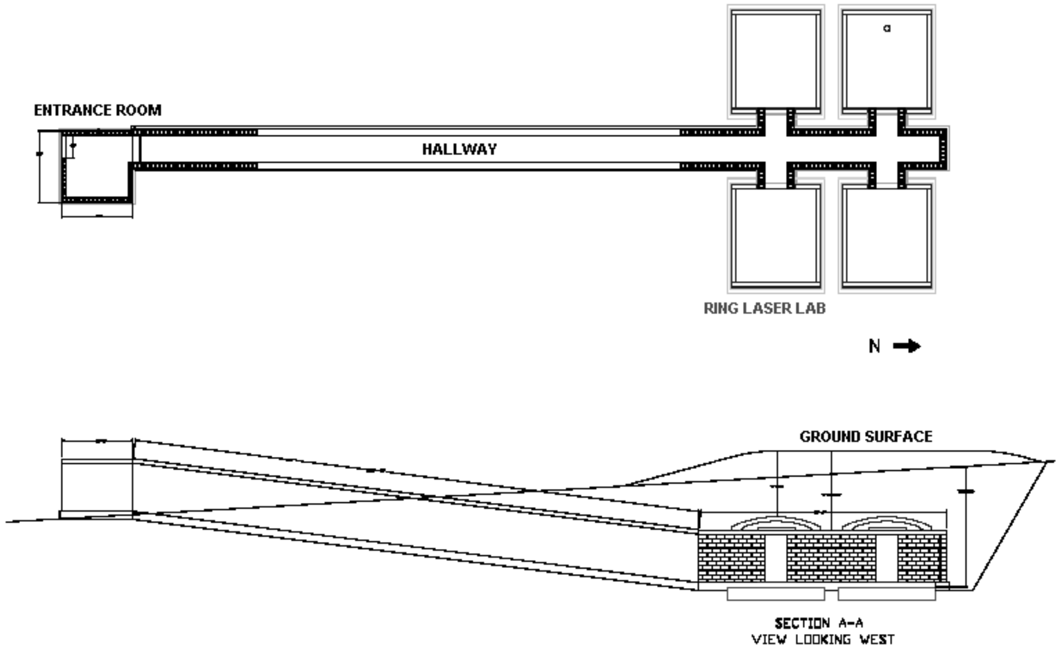

Figure 61: The Seismic Vault project diagram

The Seismic Vault facility consists of four square rooms located underground about 6 meters deep and connected with the entrance room at the ground surface via a hallway of 28 meters length. A 35 cm square concrete drain box is located in the corner of the upper right room (as shown in Figure 61) along with two 8 cm drain lines connecting to the main sump (lowest point in a drainage system) in the hallway. Each room has a size of approximately 6×6 meters with concrete arches and end walls. All the required power and data communication connections are provided as well.

We expect the GEOsensor performance under those conditions with respect to the seismic signals detection to be as good as that of G ring laser.

8 Comparison of the RLG with other techniques

So far the ring laser technology proved to be the most accurate for the seismic rotation waves detection. However there are few instruments around which also possess the capability to measure small rotations. We haven't had a chance to compare all these different techniques with the ring laser data (excluding the seismometer array) but some publications may give indications about their abilities.

8.1 Two Antiparallel Pendulum Seismometers (TAPS)

Teisseyre et al [35] use a rotation seismometer consisting of two oppositely oriented seismographs with pendulums suspended on the common axis. The paper reported the record of the Silesian earthquake 11.07.2001 M=1.5 with the distance from the epicenter to instrument location about 60 km. The obtained rotation rate variation amplitude is about 3×10^{-8} rad/s at maximum, which is in agreement with our observations of rotation perturbances caused by local seismic events. However this system has some disadvantages that may come from the construction of the sensor block, where the difference in the seismometer responses causes disturbances of the extracted rotational signal [31]. In addition it is extremely sensitive to translational motion, which might disturb the extracted rotational signal substantially, especially at the low levels.

The mechanical system is inertial thus the proper transfer function has to be estimated via careful calibration. Such a calibration has been performed by means of fiber optic gyroscope [10] demonstrating the necessity for signal smoothing and post-processing in the TAPS. Nevertheless the region of magnitudes where these tests have been carried out (sensitivity of fiber optic gyro was about 6×10^{-6} rad/s) is still too coarse to provide consistent results. The benefits of the TAPS application are unclear yet since we do not have any TAPS data for direct comparison with our ring laser recordings.

8.2 Fiber Optic Gyroscope

Fiber optic gyros (FOG) are widely used in the inertial navigation due to production advantages, constantly improving performance and a comparatively low price. The immediate superiority of FOG over the TAPS is the same as that of the ring laser – no masses involved, absolute rotation detection. The principle of FOG operation is also based on the Sagnac effect. The output signal of the FOG is the phase difference between two oppositely propagating light waves, which is proportional to the rotation speed of the instrument. When the closed beam path is formed by the optic fiber, the formula for the phase difference become

$$\Delta\varphi = \frac{8\pi \cdot N \cdot S_C}{\lambda \cdot c}\Omega = \frac{2\pi \cdot L \cdot D}{\lambda \cdot c}\Omega \tag{67}$$

where N is the number of coils of the optic fiber, S_C is the average area of the coil, L - the total length of the optic fiber, D – mean diameter of the coil.

This basic ratio demonstrates the major advantage of FOG in comparison with the ring lasers - the value of the FOG's scale factor can be made much larger than that in ring laser because of the length of the optic fiber (usually several kilometers). There are however problems of thermal susceptibility and nonreciprocity that affect the performance, but the biggest difference is that one has to do a phase difference measurement as opposed to a frequency difference measurement in ring laser.

The random walk coefficient (resolution) of FOG is considered as follows

$$\delta\Omega = \frac{\sigma\Delta\varphi}{K} = \frac{\lambda \cdot c}{2\pi \cdot L \cdot D}\sqrt{\frac{h\nu}{P_0}} \cdot \frac{1}{\sqrt{T}} \tag{68}$$

where P_0 – power of luminous flux, $\nu = \frac{c}{\lambda}$ - frequency of light, T – observation time.

For example, by using a light source with wavelength of 1.55 μm, power amplitude $P_0 =$ 100 μW, optic fiber length L of 4000 m and diameter D of 4 m the value of rotation rate sensitivity of such FOG would be $\delta\Omega = 1.65 \cdot 10^{-10} \cdot \frac{1}{\sqrt{T}}$ rad/sec.

By means of adjusting the length of the optic fiber L, the optimal tuning of the FOG can be achieved, when an obtained phase difference satisfies the ratio

$$\Delta\varphi = \frac{\pi}{2}(2n+1), \text{ where n=0,1,2...} \qquad (69)$$

Thus an operating point can be placed on a linear part of the performance curve and therefore there is no need of a phase modulator anymore. For example, the optimal diameter D for fixed optic fiber length L=4000 m can be found as:

$$\Delta\varphi = \frac{\pi}{2} = \frac{2\pi \cdot L \cdot D}{\lambda \cdot c}\Omega_V \Rightarrow D \cong 526m \qquad (70)$$

where $\Omega_V = \Omega_E \cdot \sin(\varphi_W)$, φ_W = 49.1441(6) deg – Wettzell latitude. The research group from the Polish Institute of Applied Physics designed a FOG for the detection of seismically induced rotation [11]. The gyroscope with the operation wavelength of 1.3 μm, power amplitude P_0 = 500 μW, optic fiber length L=400 m and diameter D=0.2 m has a claimed value of rotation rate sensitivity of $\delta\Omega = 9.8 \cdot 10^{-6}$ rad/sec. While it is enough for the TAPS calibration this magnitude is too small for the detection of rotational waves, at least for teleseismic events or small magnitude earthquakes. Therefore the assumption that rotational signals exist in the seismic events only for the strong earthquakes [10] can not be drawn, since the noise level of the instrument is so high that it covers such signals. However such advantages of the FOG technology like low cost and small size might be implemented for seismic rotation detection near earthquake fault in the seismically active areas or aftershock regions, where portable FOG-based stations could be quickly installed after an major earthquake. The sensors cluster consisting of one 3-axis conventional seismometer and the three FOG assembly in one box could be a cost-saving analogue of a strapdown system for seismology.

8.3 Seismic array

The seismic array is a set of seismometers distributed over an area of the Earth's surface at distance small enough so that the signal waveform may be correlated between adjacent seismometers [1]. Common seismic arrays can detect the "general area" of the earthquake focus, epicenter and hypocenter by measuring the times of arrival of the seismic waves as they are received at a minimum of three seismometers for a triangulation of the general area. These seismographs are synchronized time wise with atomic clocks or GPS. Arrays of seismographs are used to study details of sources and radiation patterns of earthquake and volcano activities. By analogue with detection of translations, the rotational motion might also be detected by using a seismic array. Figure 62 illustrates the principle of such measurement.

Since the rotation rate is a curl of the wavefield the rotation at the central point (geometrical center of the seismic array) can be derived by taking the space derivative of the velocities recorded by the seismometers. One of the methods to calculate the space derivatives by using the minimal amount of seismometers is a typical triangular grid. For a triangular grid *ijk*, by making the linear interpolation function pass through the nodes of the triangle and then taking the first order spatial derivatives of the function one obtains the following expression for the calculation of the rotation rate

$$\begin{aligned} \partial_x V_y &= \frac{1}{A}\left[b_i V_y^i + b_j V_y^j + b_k V_y^k\right] \\ \partial_y V_x &= \frac{1}{A}\left[c_i V_x^i + c_j V_x^j + c_k V_x^k\right] \end{aligned} \tag{71}$$

where A is the area of the grid *ijk*, $b_i=(y_k-y_j)/2$, $c_i=(x_k-x_j)/2$.

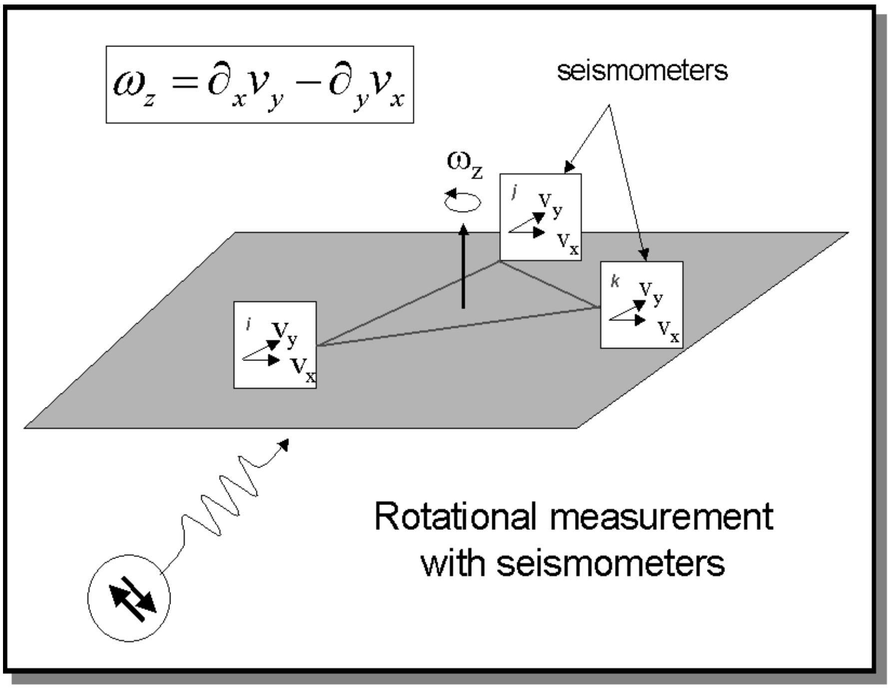

Figure 62: Rotational measurement with seismic array

Such experiment was carried out by the group of Prof. Igel in early winter 2004 [9]. The seismometer network, consisting of 9 instruments, has been deployed around Wettzell station (see Figure 63) for the time period of about four months, recording several large earthquakes.

In particular the comparison of the data has been done for the Morocco quake at 24.02.2004, M=6.4 [34]. The ring laser and seismic array data were complemented by the STS-2 broadband seismometer installed at the Wettzell station. The transverse acceleration component has been calculated using bandpass filtered (0.03-0.08 Hz) velocity seismograms and compared with the ring laser data. The two rotation seismograms were found to be generally in good agreement, apart from some amplitude differences, which are the subject of further studies.

The difficulty about deriving the rotation from array data has been the different noise level on the seismometers due to the differences in ground coupling (some of the instruments were installed on the hard rock, some on the muddy forest soil). A small difference in the noise level of the seismometers of say 5% can substantially degrade the quality of the calculations. In addition, the finite difference analysis, used for obtaining rotations from seismometers, introduces a frequency dependence of the accuracy with which those rotations can be estimated.

Despite of seemingly simplicity and low cost of this approach, the method is still vulnerable to many complications. The seismometer data has to be restituted before use in order to restore proper signal parameters in the frequency range of interest. Secondly the variations in location site properties can affect the instrument response severely. On top of that the finite difference method itself possesses limitations like accuracy frequency dependence mentioned above.

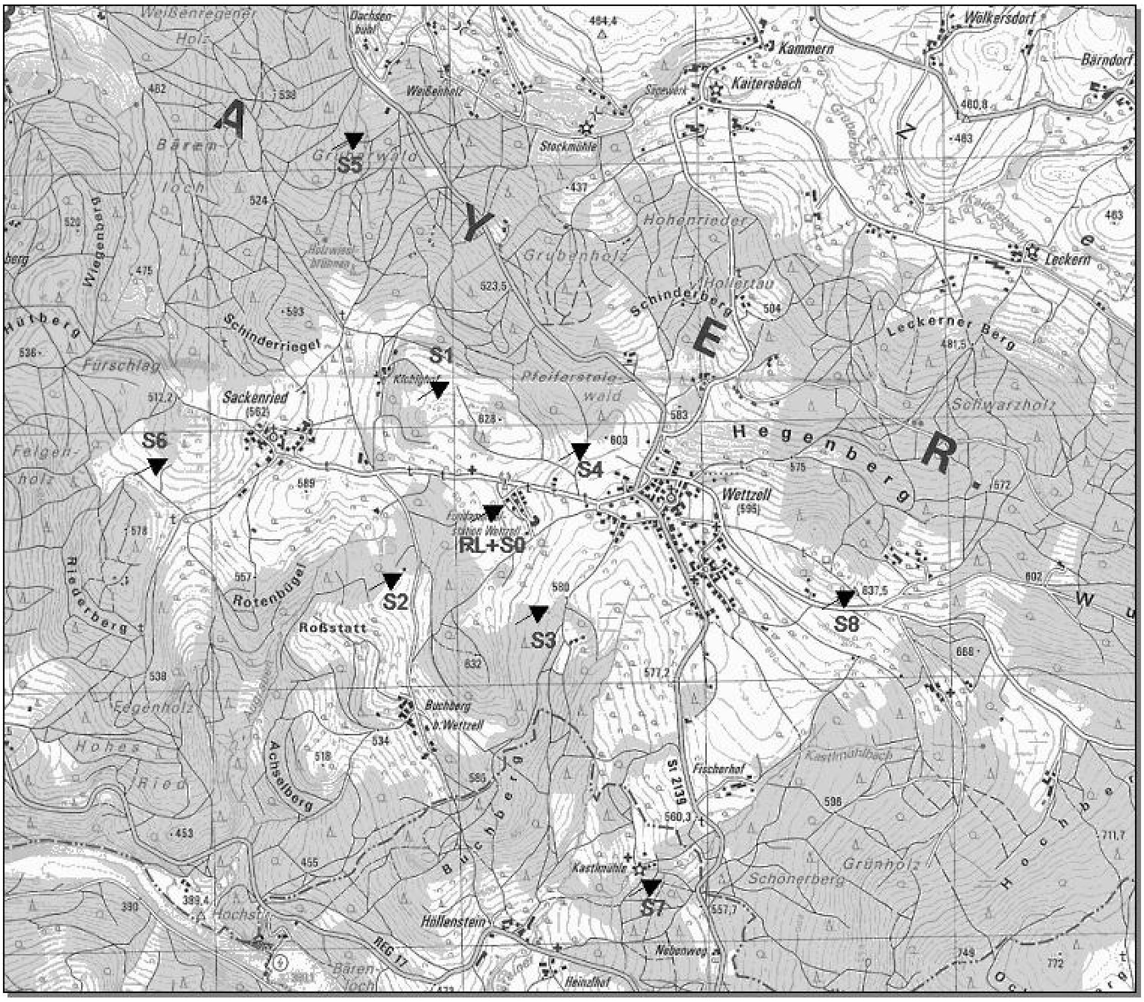

Figure 63: Location map of seismic network, seismometers marked by SN (where N – station number), RL – ring laser.

As is seen from the comparison of existing methods for measurements of seismically induced rotations, the optical gyroscope technology is still the most sensitive and provides very precise and definitive results. No additional data processing is required after the rotation rate variations are recorded. The absence of susceptibility to accelerations and a sensitivity to absolute rotation only makes these instruments far more adequate to the purpose. The large ring lasers are still the best for detection of small rotations, however the progress that was made by fiber optic sensors technology over the last decade may put those instruments on the second position after the RLG. At the current stage of the FOG sensitivity and stability it can be applied to the detection of local earthquakes with relatively large magnitude. Further development is required to make FOG a competitor to RLG in the field of the seismic rotation measurements.

9. Conclusion

As a result of the cooperation between the Technical University of München, the University of Canterbury (New Zealand) and the “Bundesamt für Kartographie und Geodäsie” a number of large ring lasers of an enclosed area between 1 and 366 square meters have been built and investigated. The high precision application of large ring lasers in geodesy can be categorized in three main areas:

- Sensor model
- Orientation model
- Rotation model

In this work we were looking at the sensor model in particular for the C-II and the G ring laser. The general ring laser model of Aronowitz [4] for an equal isotopic mixture of $Neon^{20}$ and $Neon^{22}$ was applied. The resulting model required an extended set of auxiliary parameters taken along with the Sagnac frequency at a high level of quality. It was found that the larger of the two instruments G in general works on a much reduced level of instrumental errors such as the lack of sensitivity to departures of the Sagnac frequency from the instrumental design value due to the effect of backscatter. We attribute this to the much larger separation of the mirrors in the cavity. In general about one order of magnitude improvement for the instrumental stability was achieved for datasets as long as 30 or 70 days. The relative instrumental errors of C-II are typically reduced to 10^{-4} while we achieved 3×10^{-7} for G. The limiting factor in the quality of the model corrections are usually coming from an insufficient quality of the auxiliary measurement quantities in particular the temperature values which are used to infer the changes in the length of the cavity of the ring laser and therefore the exact optical frequency for one sense of rotation. A direct precise measurement of the optical frequency is desirable but not yet available.

Nevertheless to our knowledge both rings are the most sensitive and precise rotation measurement devices for long term measurements currently existing on Earth. The successful identification of earth tides, ocean loading and diurnal polar motion demonstrates the sensitivity of this measurement technique impressively. Similar results are not yet available from any other inertial rotation measurement techniques such as atom interferometry or superconducting Helium gyroscope.

We are currently endeavoring to improve the auxiliary sensor arrangement and to obtain a high-resolution measurement of the exact optical operation frequency of our ring lasers. Also the development of the highly stable driving power control system is necessary for which an improved feedback loop scheme has been realized.

In contrary to the long-time operation instrumental trend for whose removal the model mentioned above has been developed the application of the large ring lasers in seismology needs rather short-term stability, however, the precision criterion is still very important. Furthermore such instruments need a high bandwidth. The data logging procedure according to the seismological standards has been adapted to allow the measurement of rotational velocities at the rate of 20 Hz. A number of recent earthquakes in the years 2003-2004 were successfully recorded with this new logging scheme, which is considered a key technology for the GEOSENSOR, a hybrid system for the introduction of rotation measurement to seismic applications. The frequency demodulation approach leads to a high rate data acquisition with the Sagnac frequency variations resolution that is not achievable by means of both traditional period counting hardware and frequency estimation algorithms. The accurate timestamping of the measured data is achieved by means of a GPS standard time/frequency source.

For better compatibility with the requirements in seismology a fully autonomous data acquisition system for the GEOsensor, based on National Instruments real-time technology, has been developed. This system was tested in the geodetic observatory Wettzell and is currently on its way to the Pinion Flat seismic observatory, California USA.

The comparison of the rotational seismograms taken from the different ring lasers with the same vertical orientation proved the credibility and adequateness of the results produced. The analysis of the ring laser orientation such as the tilting of the basement during an earthquake shows that for teleseismic events the tilt influence is almost an order of magnitude smaller that the actual signal amplitude and hence can be ignored or corrected if required. However for close events the orientation must be taken into account and a suitable tiltmeter is considered a vital part of the GEOsensor system. The theoretical correlation between the rotation rate and the transverse acceleration has been confirmed which opens a new field to the 3D ground motion model development and study. Moreover the synthetic seismograms calculated for a few major earthquakes in the years 2003-2004 show marvelous agreement with the corresponding rotation rate measurements. The understanding of the origin of the discrepancies between the rotation rate and the acceleration may provide valuable information about the crust structure, which cannot be obtained from the translation seismogram alone.

The comparison with the other techniques that might be applied for detection of small rotations during an earthquake shows that currently none of those instruments are capable of providing the required sensitivity. However for a particular situation such as a close fault location, volcano seismic activity detection the FOG technology seems suitable to combine the advantages of optical rotation sensors with small size and low-cost characteristics.

References

1. Aki K. and P.G. Richards, Quantitative Seismology. Theory and Methods, Freeman, San Francisco, 1980.

2. T. D. Anh, W. Dietel; Homogeneous broadening in a 0.63 μm single mode He-Ne laser, Opto-electronics 5, 243-248, 1973.

3. F. Aronowitz; Fundamentals of the Ring Laser Gyro, Optical Gyros and their Application, RTO AGARDograph 339, 1999.

4. F. Aronowitz; The Laser Gyro, Laser Applications, M. Ross, Academic Press, New York, 1971, 1, 133-200.

5. H. R. Bilger, G. E. Stedman, P. V. Wells; Geometrical dependence of polarisation in near-planar ring lasers, Optics Communications, Vol. 80, No. 2, 133-137, 1990.

6. A. Brzezinski; Contribution to the theory of polar motion for an elastic earth with liquid core, manuscripta geodaetica, 11 226-241, 1986.

7. R. B. Hurst, R. W. Dunn, K. U. Schreiber, R. J Thirkettle, G. K. MacDonald; Mode behavior in ultralarge ring lasers, Applied Optics, Vol. 43, No. 11, 2004.

8. Igel H., Schreiber, U., Flaws, A., Velikoseltsev, A., Schuberth, AB., Cochard, A. (2004). Rotational motions induced by the M8.1 Tokachi-oki earthquake, September 25, 2003, submitted to JGR MS 2004GL022336.

9. Igel H., Suryanto W., Wassermann, J., Scherbaum, F., Vollmer, D., Schreiber, U., Velikoseltsev, A. (2004). Comparison of direct measurements of rotational ground motions with seismic array measurements, manuscript in preparation.

10. L. R. Jaroszewicz, Z. Krajewski, L. Solarz; "Usefulness of the fiber-optic interferometer for detection of the seismic rotation waves", ABTOMETRIA Optoelectronics, Instrum. and Data Processing, 39, 5, (2003), 91-101.

11. L.R. Jaroszewicz, Z. Krajewski, L. Solarz, R. Teisseyre, "Fiber-optic Sagnac interferometer as a system for the electromechanical rotational seismometer calibration and a new senor of the rotational seismic events", EGS-AGu-EUG Joint Assembly, 7-11.04.2003, Nice, France

12. B Tom King; Ring Laser Dynamics, Ph.D. Thesis, University of Canterbury, New Zealand, 1999.

13. A. Levine, A. DeMaria,; Lasers vol. 4, Narcel Dekker, INC., New York, 1976.

14. P. McClure; Diurnal polar motion, GSFC Rep. X-529-73-259, Goddard Space Flight Center, Greenbelt, Md., 1973.

15. D.P. McLeod, G.E. Stedman, T.H. Webb, U. Schreiber, Comparison of standard and ring laser rotational seismograms, Bull. Am. Seis. Soc.. 88, 1495-1503, 1998.

16. D.P. McLeod, B.T. King, G.E. Stedman, T.H. Webb, K.U. Schreiber, T.H. Webb, Autoregressive analysis for the detection of earthquakes with a ring laser gyroscope, Fluctuation and Noise Letters, Vol. 1, No. 1, R41-R50, 2001.

17. P. W. Milloni, J. H. Eberly; Lasers, Wiley-Interscience Publ., 1998.

18. Nelder J. A. and Mead R., Computer Journal, vol. 7, pp. 308-313, 1965.

19. T. Klügel; Analyse der Zeitreihen lokaler Rotationssensoren - Entwicklung eines Orientierungsmodells, Schlußbericht zum DFG-Forschungsprojekt, 2001.

20. Pancha A., Webb T.H., Stedman G.E., McLeod D.P., Schreiber K.U.; Ring laser detection of rotations from teleseismic waves, Geophys. Res. Lett. 27, 3553-3556, 2000.

21. S. Riepl; Analyse der Zeitreihen lokaler Rotationssensoren - Entwicklung eines Rotationsmodells, Schlußbericht zum DFG-Forschungsprojekt, 1999.

22. R. Rodloff; A Laser Gyro with Optimized Resonator Geometry; IEEE Journal of Quantum Electronics, Vol. QE-23, No. 4, 438-445, 1987.

23. U. Schreiber; Ringlasertechnologie für geowissenschaftliche Anwendungen, Habilitationsschrift, Forschungseinrichtung Sattellitengeodäsie der TU München, März 1998.

24. U. K. Schreiber, C. H. Rowe, D. N. Wright, S. J. Cooper, G. E. Stedman; Precision stabilization of the optical frequency in a large ring laser gyroscopes, Applied Optics, Vol. 37, No. 36, 8371-8381, 1998.

25. U. Schreiber, A. Velikoseltsev, T. Klügel, G. E. Stedman; Advances in the Stabilization of Large Ring Laser Gyroscopes, Proceedings of the Symposium Gyro Technology, Stuttgart, 2001.

26. U. Schreiber, A. Velikoseltsev, H. Igel, A. Cochard, A. Flaws, W. Drewitz, F. Müller; The GEOSENSOR: a new instrument for seismology, Geotechnologien science report No 3, 148-151, 2003.

27. U. Schreiber, A. Velikoseltsev, G. E. Stedman, R. B. Hurst, T. Klügel; Large Ring Laser Gyros as High Resolution Sensors for Application in Geoscience, Proceedings of the 11th International Conference on Integrated Navigation Systems, Saint Petersburg, 2004

28. A. E. Siegman; Lasers, University Science Books, 1986.

29. P. W. Smith; The effect of cross relaxation on the behavior of gas laser oscillators, IEEE Journal of quantum electronics, Vol. QE-8, No. 8, 704-709, 1972.

30. P. W. Smith; Mode Selection in Lasers; Laser Devices and Applications, IEEE Press, 1973.

31. L. Solarz, Z. Krajewski, L.R. Jaroszewicz, "Analysis of seismic rotations detected by two antiparallel seismometers: Spline function approximation of rotation and displacement velocities", Acta Geophys. Pol., 53, 2 (2004), in print

32. G. E. Stedman, Z. Li, C. H. Rowe, A. D. McGregor, H. R. Bilger; Harmonic analysis in a large ring lasers with backscatter induced pulling, Phys. Review A, Vol. 51, No. 6, 4944-4958, 1995.

33. G. E. Stedman; Ring laser tests of fundamental physics and geophysics, Rep. Progr. Phys. 60 615-688, 1997.

34. W. Suryanto, D. Vollmer, J. Wassermann, H. Igel, F. Scherbaum; Array experiment to estimate rotational motions induced by earthquakes (comparison with ring laser measurements), EGS 2004 poster presentation.

35. R. Teisseyre, J. Suchcicki, K. P. Teisseyre, J. Wiszniowski, P. Palangio; Seismic rotation waves: basic elements of theory and recording, Annals of Geophysics, Vol. 46, No. 4, August 2003.

36. P. V. Wells; Polarisation Dependence on Aplanarity in the Near-Planar Ring Lasers, Ph.D. Thesis, University of Canterbury, New Zealand, 1997.

37. D. N. Wright; Optimisation of Ring laser gyroscopes, Ph.D. Thesis, University of Canterbury, New Zealand, 2001.

38. А.С. Батраков, М.М. Бутусов, Г.П. Гречка и др., под ред. Д.П. Лукьянова, Лазерные измерительные системы, Радио и связь, 1981.

39. М.Н. Бурнашев, Ю.В. Филатов; Основы лазерной техники, Изд. СПбГЭТУ «ЛЭТИ», Санкт-Петербург, 2000.

40. Н.В. Кравцов, Н.Н. Кравцов; Невзаимные эффекты в кольцевых лазерах, Квантовая электроника, 27, № 2б 1999.

41. В. В. Тучин; Динамические процессы в газоразрядных лазерах. М.: Энергоатомоиздат, 1990.